TRW Space, Defense & Information Systems

One Space Park
Redondo Beach, CA 90278

CAGE No. 11982

TITLE

EO-1/ Hyperion Early Orbit Checkout Report Part II: On-Orbit Performance Verification and Calibration

DATE: September 27, 2002

NO. HYP.TO.01.066PR
REV Public Release

Superseding: Original

PREPARED BY: Carol Segal for 9-20-02
Pamela Clancy — Date
Performance Verification Lead

APPROVAL SIGNATURES:

Carol Segal 9-20-02
Carol Segal — DATE
TRW Deputy Project Manager
Science and Operations

Steve Carman 9-20-02
Steve Carman — DATE
TRW Hyperion Project Manager

_____ DATE

_____ DATE

_____ DATE

_____ DATE

ORIGINAL PDMO RELEASE _____ DATE

TABLE OF CONTENTS

This document was prepared by the Hyperion On-Orbit Performance Verification Team. The primary area of responsibility for each team member is provided below.

Pamela Clancy, Team Lead
Dave Adachi, Focal Plane Electronics
Suzanne Casement, VNIR and SWIR Noise Characteristics
Peter Jarecke, Radiometric Calibration Lead
Neil Nelson, Image Quality Lead
John Shepanski, Spectral Calibration, SWIR Echo
Karen Yokoyama, Solar Calibration Lead
Lihong Wang, HypPerform Data Processing Tool

1 INTRODUCTION

Hyperion is the hyperspectral imager on the Earth-Observing 1 (EO-1) spacecraft that was launched from Vandenberg Air Force Base on November 21, 2000. EO-1 is part of NASA's New Millennium Program which is an initiative to demonstrate advanced technologies for dramatically reducing the cost and improving the quality of instruments and spacecraft for future space missions. Under this program, missions are intended primarily to validate new technologies in flight and to provide useful scientific data to the user community. The other instrument payloads on the spacecraft are ALI (Advanced Land Imager) and AC (atmospheric corrector).

The first three months of the mission life were focused on instrument activation and checkout as well as performance verification. This document is Part II: On-Orbit Performance Verification and Calibration of the EO-1/ Hyperion Early Orbit Checkout Report. Part I: Hyperion Activation and Operation discusses the activation period, results and lessons learned.

1.1 Scope

This document describes the results of the Hyperion on-orbit performance verification task. The on-orbit performance was compared with the pre-flight characterization and requirement specification. This document describes the analysis technique, estimated accuracy of the technique and the scenes used in the analysis.

1.2 Instrument Overview

The Hyperion instrument provides high quality calibrated data that can support evaluation of hyperspectral technology for Earth observing missions. Hyperion is a pushbroom, imaging spectrometer. Each image taken in this configuration captures the spectrum of a line 30m along-track by 7.75Km wide (perpendicular to the satellite motion). Hyperion has a single telescope and two spectrometers, one visible/near infrared (VNIR) spectrometer and one short-wave infrared (SWIR)) spectrometer. The Hyperion instrument consists of 3 physical units: 1) the Hyperion Sensor Assembly (HSA), 2) the Hyperion Electronics Assembly (HEA), and 3) the Cryocooler Electronics Assembly (CEA). The HSA includes subsystems for the telescope (fore optics), internal calibration source, the two grating spectrometers and the supporting focal plane electronics and cooling system as seen in Figure 1.2-1. The telescope images the Earth onto a slit that defines the instantaneous field-of-view which is 0.624° wide (i.e., 7.5 Km swath width from a 705 Km altitude) by 42.55 μ radians (30 meters) in the satellite velocity direction. This slit image of the Earth is relayed to two focal planes in the two grating spectrometers. A dichroic filter in the system reflects the spectral region from 400 to 1,000 nm to a VNIR spectrometer and transmits the region from 900 to 2500 nm to a SWIR spectrometer. The HEA contains the interface and control electronics for the instrument and the CEA controls cryocooler operation. These units are all placed on the nadir-facing deck of the spacecraft with the viewing direction as shown in Figure 1.2-2

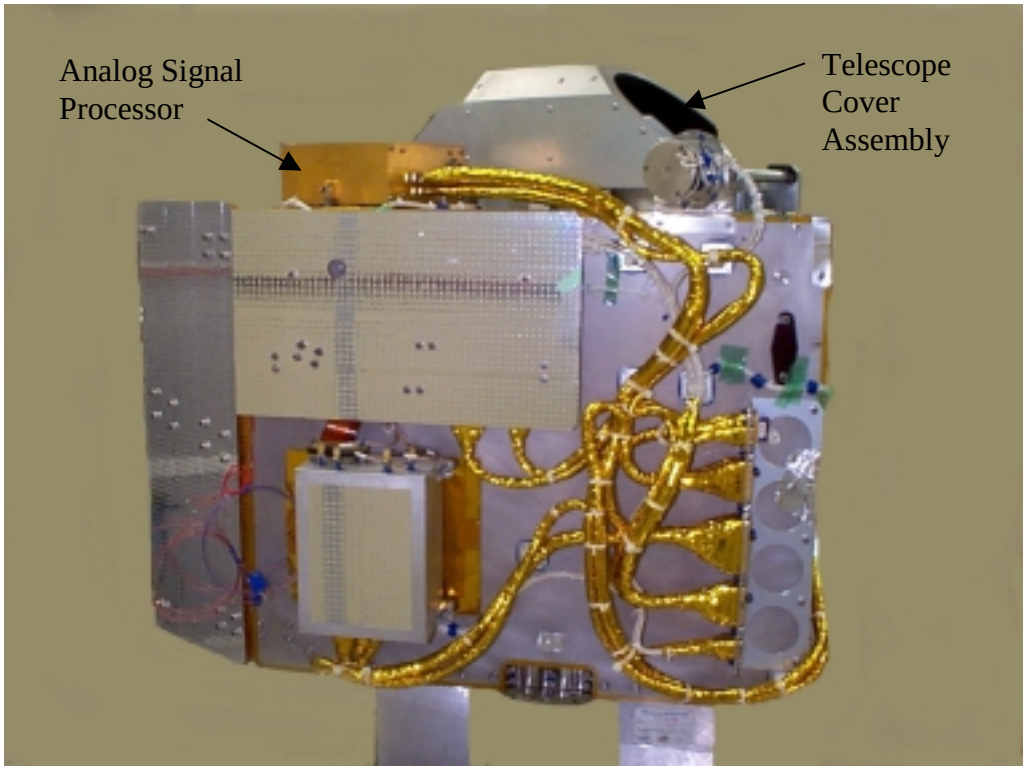

Figure 1.2-1. Hyperion Sensor Assembly (HSA) includes the telescope fore-optics, internal calibration source, the two grating spectrometer, mechanical cryocooler and analog signal processing electronics.

The visible/near-infrared (VNIR) spectrometer has an array of 60 μm pixels in a Charge-Coupled Device (CCD) detector array. The VNIR spectrometer uses a 70 (spectral) by 256 (spatial) pixel array, which provides a 10 nm spectral bandwidth over a range of 400-1000 nm. The shortwave infrared (SWIR) spectrometer has 60 μm HgCdTe detectors in an array of 172 (spectral) x 256 (spatial) channels. Similar to the VNIR, the SWIR spectral bandwidth is 10 nm. Thus, the spectral range of the instrument extends from 400 to 2,500nm with a spectral resolution of 10nm. The HgCdTe detectors, cooled by an advanced TRW cryocooler, are maintained at 110 K.

A common calibration system is provided for both the VNIR and SWIR spectrometers. The solar calibration utilizes a diffuse reflector on the backside of the optical cover to provide uniform illumination across the focal plane arrays. The cover is partially opened during solar calibration and the spacecraft is oriented such that the sun enters the solar baffle in a direction normal to the usual nadir viewing angle. Solar data are used as the primary source for monitoring radiometric stability, with ground site (vicarious) and lunar imaging treated as secondary calibration data. The internal calibration subsystem provides additional information for tracking instrument performance.

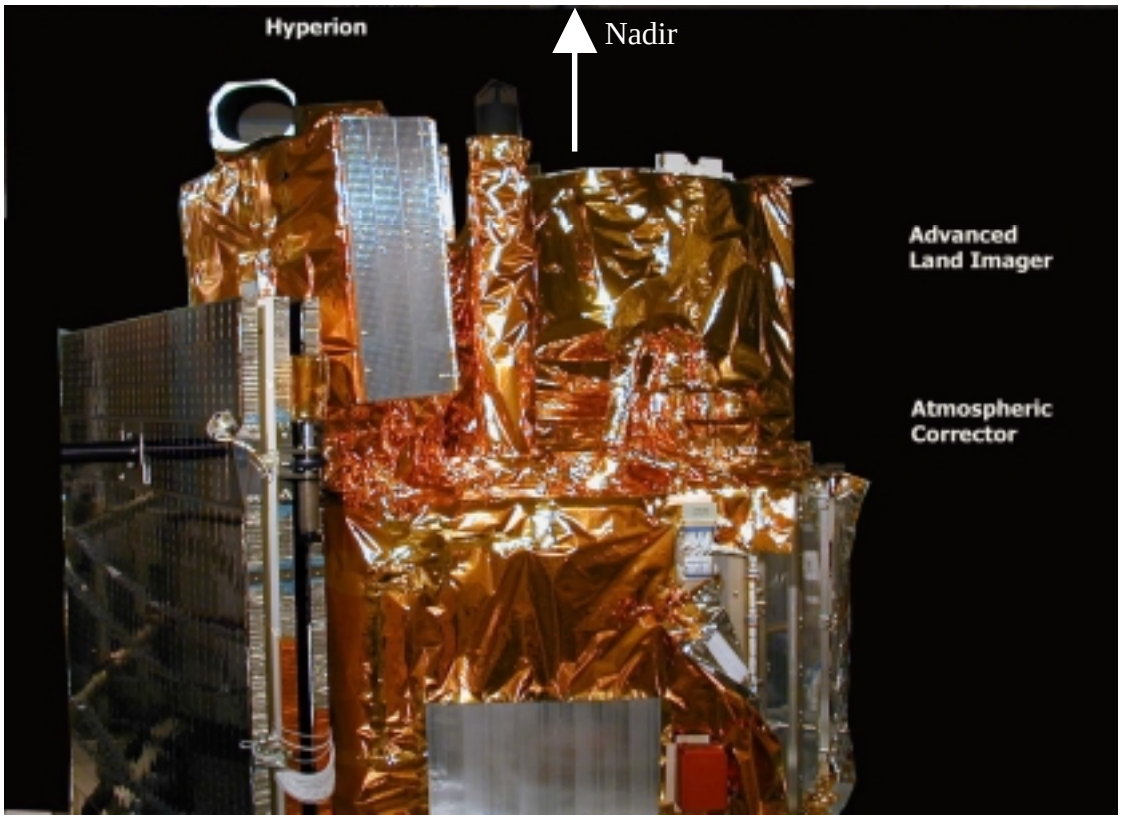

Figure 1.2-2. Hyperion shown installed on the EO-1 spacecraft (upper left in photo)

1.3 Document Organization

The document is organized in eight chapters. Chapter 1: Introduction provides a general overview of the instrument and the EO-1 mission. Chapter 2: Requirements reviews the instrument requirements, pre-flight characterization and comparison of the on-orbit characterization. The on-orbit verification confirms that the pre-launch characterization is still applicable. The following chapters contain the details of the analysis for the on-orbit assessment of each of the requirements. Chapter 2 also points to various sections in the document that can be referred to for the analysis pertaining to each requirement. Chapter 3: VNIR Focal Plane Characteristics and Chapter 4: SWIR Focal Plane Characteristics have the same organization. However, since there are two different types of focal planes, which have different artifacts and subtleties, the discussion of each was separated. Both chapters address the fundamental performance of each focal plane and assess the impact of residual errors on the final precision estimate. Chapter 5: Absolute Calibration and Accuracy presents the basis for the pre-flight absolute calibration and how the pre-flight calibration was updated for use in level 1 processing of scientific data. This chapter explains how the solar calibration event was used in support of the on-orbit calibration determination. The performance of the in-flight calibration lamp is also reviewed. The chapter concludes with an estimate of the on-orbit end-to-end measurement error. Chapter 6: Spectral Verification describes the technique developed and implemented to verify the on-orbit spectral calibration. Chapter 7: Image Quality details the techniques used to measure the on-orbit Modulation Transfer Function (MTF), Ground Sample Distance (GSD) and

VNIR/SWIR co-registration values. Chapter 8: Summary and Chapter 9: Recommendations for Remaining Mission summarizes the on-orbit performance of Hyperion and provides recommendations for monitoring the Hyperion performance for the remainder of the mission.

Figure 1.3-1 presents an overview of the performance verification approach with associated chapter and section. This flow diagram indicates the major areas in the overall performance verification task and indicates the chapter in which they are addressed in detail.

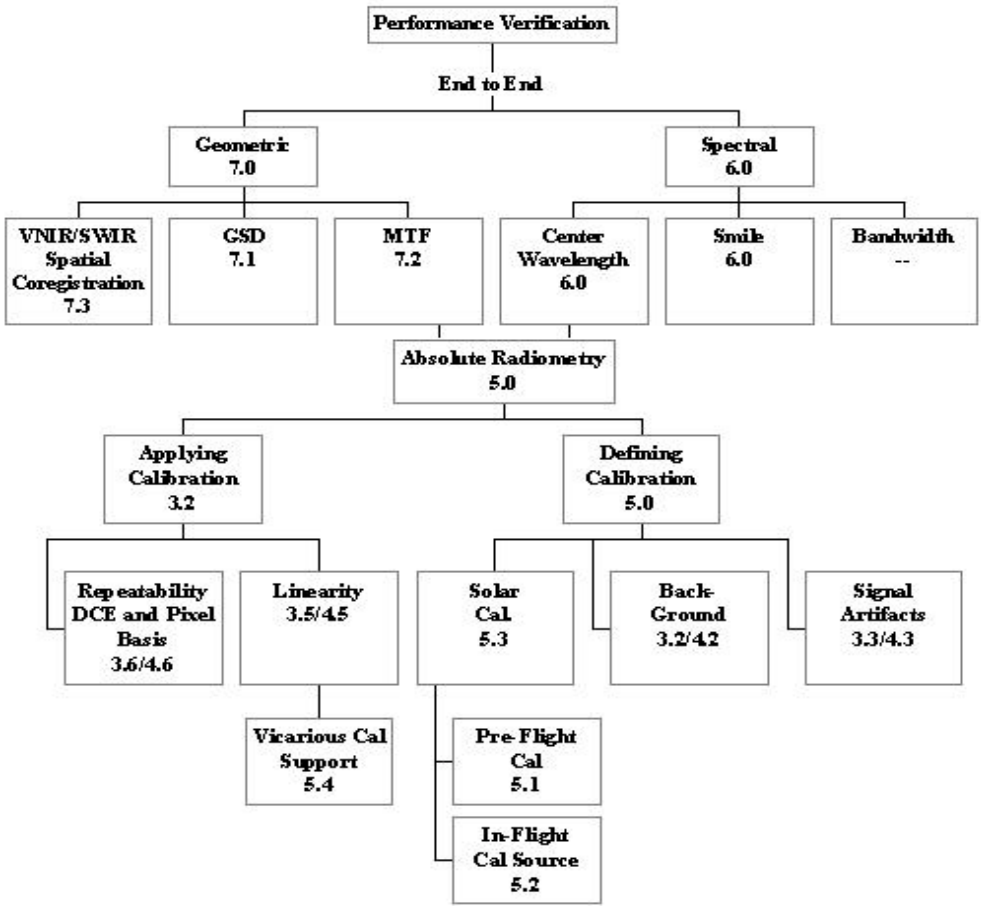

Figure 1.3-1 Overview of Performance Verification Flow

1.4 Reference Documents

The following documents are referred to herein:

P. Jarecke, K. Yokoyama, "Radiometric Calibration of the Hyperion Imaging Spectrometer Instrument From Primary Standards to End-to-End Calibration" ", *Proc. of SPIE*, Vol. 4135, pp 254-263, July 2000
J. H. Walker, R. D. Saunders, J. K. Jackson, D.A. McSparron, "Standard Irradiance Calibrations", NBS Special Publication No.250-20 (1987)
J. Geist, "Quantum Efficiency of the p-n Junction in Silicon as an Absolute Radiometric Standard.", Appl. Opt. 18, 760 (1979)
J. Geist, E.F. Zalewski and A.R. Schaefer, "Spectral Response Self-Calibration and Interpolation and Silicon Photodiodes", Appl. Opt., 19, 3795 (1980)
N. P. Fox, "Trap Detectors and Their Properties", Metrologia, 28, 197 (1991)
W. M. Doyle, B. C. McIntosh and J. Geist, "Implementation of a System of Optical Calibration Based on Pyroelectric Radiometry", Optical Eng., 15, 541, (1976)
E. F. Zalewski and C. C. Hoyt, "Comparison Between Cryogenic Radiometry and the Predicted Quantum Efficiency of pn Silicon Photodiode Light Traps", Metrologia, 28, 203, (1991)
C. Wehrli, World Radiation Center Davos-Dorf, Switzerland, (WCRP) Publication Series No. 7, WMO ITD-No. 149, pp 119-126, October 1986.
G. Thuillier, M. Herse, P. C. Simon, D. Labs, H. Mandel, D. Gillotay, and T. Foujols, "The visible solar spectral irradiance from 350 to 850 nm as measured by the SOLSPEC spectrometer during the ATLAS-1 mission", *Solar Physics*, **177**, 41-61, 1998
Kurucz, R. L., I. Furenlid, J. Brault, and L. Testerman, Solar Flux Atlas from 296 nm to 1300 nm, National Solar Observatory Atlas No. 1, 1984.

2 REQUIREMENTS

The goal of the performance assessment was to determine whether the pre-flight Hyperion characterization was still applicable to on-orbit operations. The results of this assessment are summarized and compared with the pre-flight values in Tables 2.1-1 - 2.1-3. The tables are segmented into Radiometric Results, Spectral Verification Results and Image Quality Results. Each table contains the requirement, the pre-flight value, the on-orbit value as well as the section that can be referred to for technical justification. As can been seen in these tables, the on-orbit assessment is consistent with pre-flight characterization.

Table 2.1-1 Radiometric Performance

	Spectral Range	Requirement	Pre-Flight	On-Orbit	Reference Section
Absolute Radiometery (end-to-end)	VNIR	< 6%	< 6%	consistent with preflight	5.5
	SWIR	< 6	<6%	consistent with preflight	5.5
SNR	550 nm	> 60	150	192	3.4
	650 nm	>60	140	140	3.4
	700 nm	> 60	140	140	3.4
	1025 nm	> 60	90	65	4.4
	1225 nm	> 60	110	96	4.4
	1575 nm	> 60	89	64	4.4
	2125 nm	> 30	40	38	4.4
Quantization	All	12 bit	12 bit	12 bit	

Table 2.1-2 presents the spectral calibration results that are discussed in detail in Chapter 6. Although there are 220 unique spectral channels, the baseline on-orbit calibration file allows Level 1 processing to calibrate 196 unique spectral channels, and has an additional 4 channels of overlap. The spectral bandwidth was measured precisely during TRW ground testing. Direct on-orbit measurements of this value were not attempted. A technique using an atmospheric limb data collect was developed to verify the center wavelengths for the VNIR and SWIR spectral channels. The number of spectral features in the SWIR portion of the data, due to the combination of atmospheric lines and lines on the diffuse reflectance panel, enabled verification of the center wavelength for the entire SWIR to ±3 nm. The number of available lines in the VNIR was limited but was able to confirm that the pre-flight VNIR spectral calibration was still valid. The results of the center-wavelength verification were used to determine the cross-track spectral error and the dispersion, which impacts the spectral range. The VNIR crosstrack spectral error exceeds the requirement. This was reported during pre-flight characterization and a waiver was issued. The on-orbit measurements verify the ground measurement to within the measurement accuracy.

Table 2.1-2 Spectral Performance

	Instrument Parameter	Requirement	Pre-Flight	On-Orbit	Reference Section
Number of Spectral Channels	VNIR & SWIR	220	comply	comply, 200 selected for Level 1 processing	6.1
Spectral Range		400-2500 nm	357-2576 nm center wavelengths determined to ± 1 nm	357-2576 nm, 436-2406 nm selected for Level 1 processing	6.1
Spectral Bandwidth	VNIR	10 +/- 0.1 nm	10.08–10.09	Not measured	
	SWIR	10 +/- 0.1 nm	10.11-10.13	Not measured	
Cross Track Spectral Error	VNIR	1.5*	2.57-3.59	1.71-2.55	6.5
Cross Track Spectral Error	SWIR	2.5	.17-.98	.40-.97	6.4

*Non-compliance waived pre-flight.

Table 2.1-3 presents results for the Image Quality parameters. Chapter 7 discusses the analyses performed and the accuracy to which each parameter was verified. The VNIR and SWIR spatial co-registration of spectral channels were consistent with the requirements and pre-flight characterization to within the accuracy of the on-orbit measurement. In this case, the on-orbit status is considered to support the pre-flight characterization.

Table 2.1-3 Image Quality Performance

	Instrument Parameter	Requirement	Pre-Flight	On-Orbit	Reference Section
GSD	Entire Range	30 m +/- 1 m	29.88	30.38	7.1
Swath Width	Entire Range	> 7.5 km	7.75 km	7.75 km	7.1
MTF (In-Track)	450 nm	> 0.2	.22-.29 meas. @ 500nm	.23-.27 meas. @ 500nm	7.2
	630 nm	> 0.2	.22-.27	.23-.27	7.2
	900 nm	> 0.15	.22-.24	.24-.28	7.2
	1250 nm	> 0.14	.27-.30	.20-.25	7.2
	1650 nm	> 0.15	.25-.27	.28	7.2
	2200 nm	> 0.15	.23-.28	Not avail	7.2
VNIR spatial Co-Registration	All	20% of Pixel*	Met .1-.25	Consistent with pre-flight, .1-.3	7.3
SWIR spatial Co-Registration	All	20% of Pixel*	Met .18-.28	Consistent with pre-flight, .25 ±. .15	7.3

*Non-compliance waivered pre-flight

3 VNIR FOCAL PLANE CHARACTERISTICS

This chapter discusses the performance characterization of the VNIR focal plane. Focal plane repeatability, and noise are evaluated.

The data in Table 3-1 was used to characterize various aspects of the VNIR focal plane and are referred to in following sections.

Table 3-1

Day	Image	Used for
00-345	Active Illumination	Dark noise
00-347	Solar Calibration	Dark noise
00-348	Panorama	Dark noise
00-362	Arabia #1 (elevated ASP temperature)	Dark noise
01-008	Moomba	Dark noise
01-010	Lunar Calibration (missed moon)	Pattern residual, drift
01-018	Belize (lowered ASP temperature)	Dark noise
01-020	Libya #1 (lowered ASP temperature)	Dark noise
01-022	Laupahoehoe (lowered ASP temperature)	Dark noise
01-038	Lunar Calibration	Crosstalk
01-047	Solar Calibration	Outlier Pixels

3.1 VNIR Introduction

This section introduces the VNIR focal plane, presents a detailed discussion of the VNIR performance and proposed explanation for the subtleties of the focal plane.

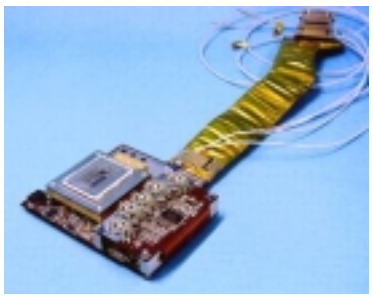

3.1.1 VNIR Focal Plane Description

The visible/near-infrared (VNIR) Focal Plane Array (FPA) was a custom development for the SSTI instrument. This VNIR FPA is a MPP 2-D frame transfer CCD with 384 x 768 pixels of 20μm pitch. The FPA pixels are divided equally into 4 quadrants each. The Hyperion VNIR spectrometer uses a 70 (spectral) x 256 (spatial) pixel section of the VNIR FPA to provide a 10 nm spectral bandwidth over a range of 400-1000 nm. The output of the CCD is controlled by the VNIR Focal Plane Electronics (FPE) and converted from analog to digital format in the VNIR Analog Signal Processor (ASP). The FPE and ASP electronics are thermally isolated from the spacecraft.

The ASP has an operating temperature range of –10C to 50C. During operation, the ASP temperature increases and this ultimately limits the operating "on" time. Currently the VNIR ASP is heated to a 32-34 C starting operating temperature, which is the typical temperature range for a single data collection event (DCE).

3.2 VNIR Background Level Removal

One of the first procedures for processing the raw data is to subtract off a dark frame. This is required because each image includes not only the scene signal but also a signal caused by thermally generated electrons in the bulk material. To enable removal of this signal, three dark frames are taken as part of each DCE. Each dark file is 1 second of data, corresponding to approximately 220 frames. These are then subtracted from the image files to leave just the signal generated by the incoming photons.

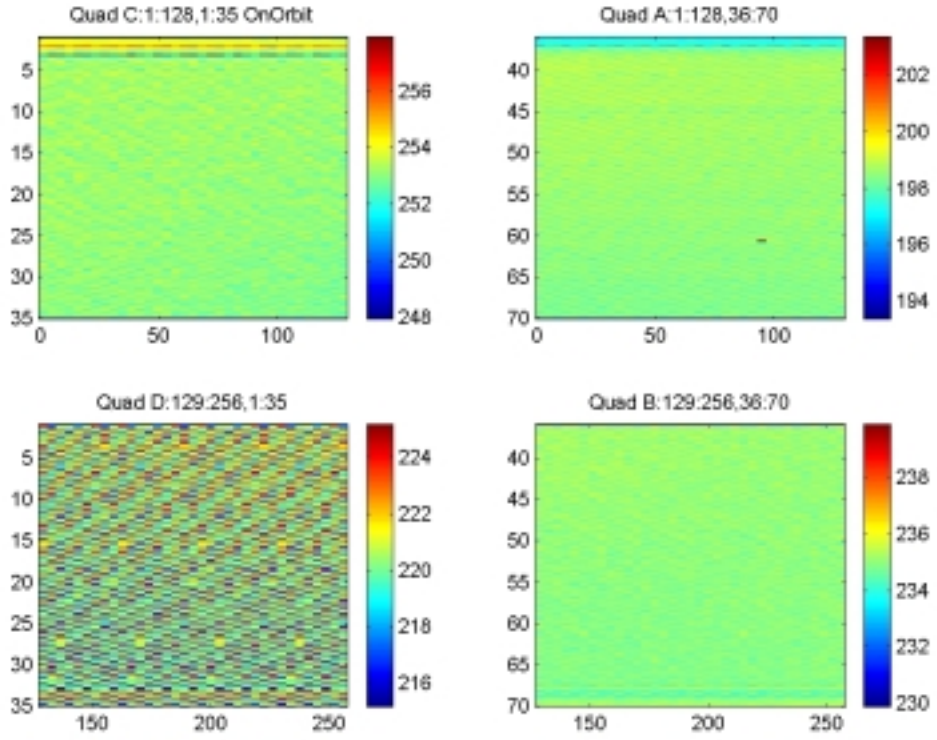

Figure 3.2-1: VNIR Dark Example: Mean of a dark frame from early on-orbit data showing a large pattern noise in the lower left quadrant. All quadrants are shown at the same stretch in counts or DN, centered on the quadrant mean.

Figure 3.2-1 is an example of the average dark for each quadrant. The quadrants are labeled by Quadrant Identifier: range of FOV, range of spectral channels. Each quadrant has a different dark level, and accordingly, the data in the figure is scaled to the mean of the quadrant.

3.2.1 VNIR Dark Pattern and Residual

The pattern noise, evinced as “quilting” in the output data of the FPA, was noted during thermal vacuum testing. The pattern is clearly seen in Quadrant D and to a much lesser degree in Quadrant C. The pattern is consistent throughout a DCE, though the pattern is seen to shift between DCEs. The pattern is also identifiable when looked at a distribution of the dark level for each quadrant in time as well as in space (Figure 3.2-2). Quadrants A and B appear gaussian whereas Quadrants C and D do not. This distribution is temperature sensitive.

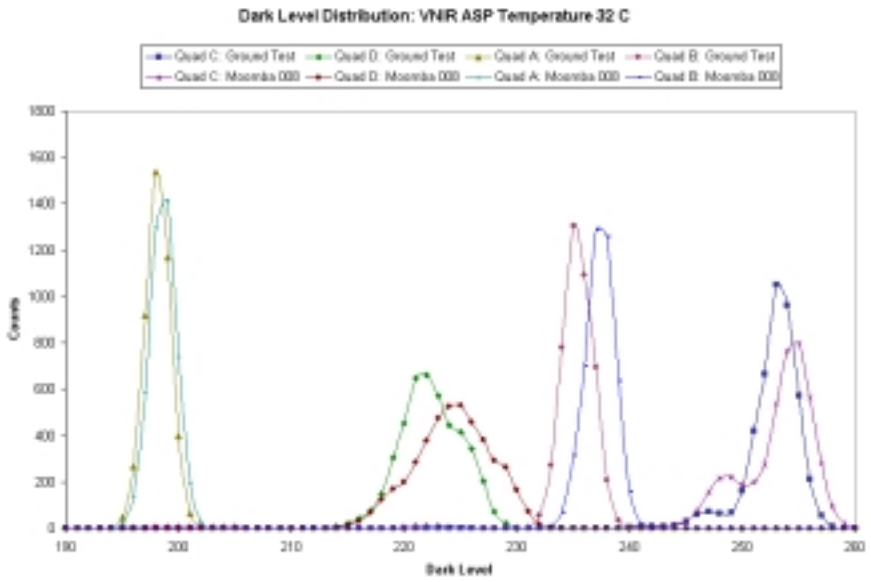

Figure 3.2-2: Dark level distribution by quadrant both ground and on orbit.

In a single spatial pixel this pattern noise shows up as a jig saw pattern that repeats over 3 spectral channels. Figure 3.2-3 shows data from spatial pixel 199 in Quadrant D and shows all of the dark image data examined for this study, listed in Table 3-1. Note that the day 347 data are offset in the starting point of the pattern from the rest of the data, though the pattern is consistent throughout each DCE. Day 347 band 1 is in the "low" position while the rest of the data start in the "high" position of the pattern. The pattern noise appears to subtract out exactly within a DCE as the lamp data, after dark subtraction, are equally matched between Quadrants D and B for one spatial pixel 199 as shown in Figure 3.2-4. This shows that the fixed pattern noise is not a function of illumination level.

To measure any residual dark pattern noise in the data, the lunar calibration DCE from 01-010 was used as a test case. The pre and post image dark frames were averaged and subtracted from an average of the image data. Figure 3.2-5 shows a cut through the subtracted data for that same pixel as in Figures 3.2-3 and -4. No evidence of the previously strong jigsaw pattern is seen, so the noise due to the residual pattern is well below the other noise sources present.

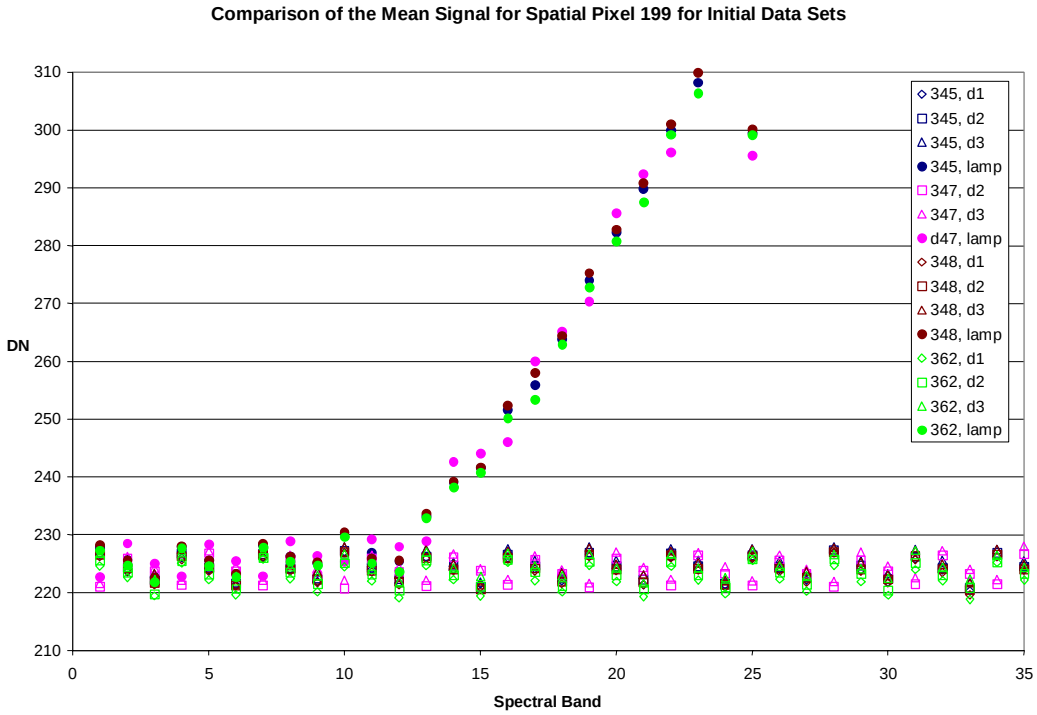

Figure 3.2-3: Dark and raw lamp data for spatial pixel 199 in quadrant D. Note that the day 347 data are offset in pattern from the rest of the data, though it is consistent throughout each DCE. Day 347 band 1 is in the "low" position while the rest of the data start in the "high" position of the jig saw pattern.

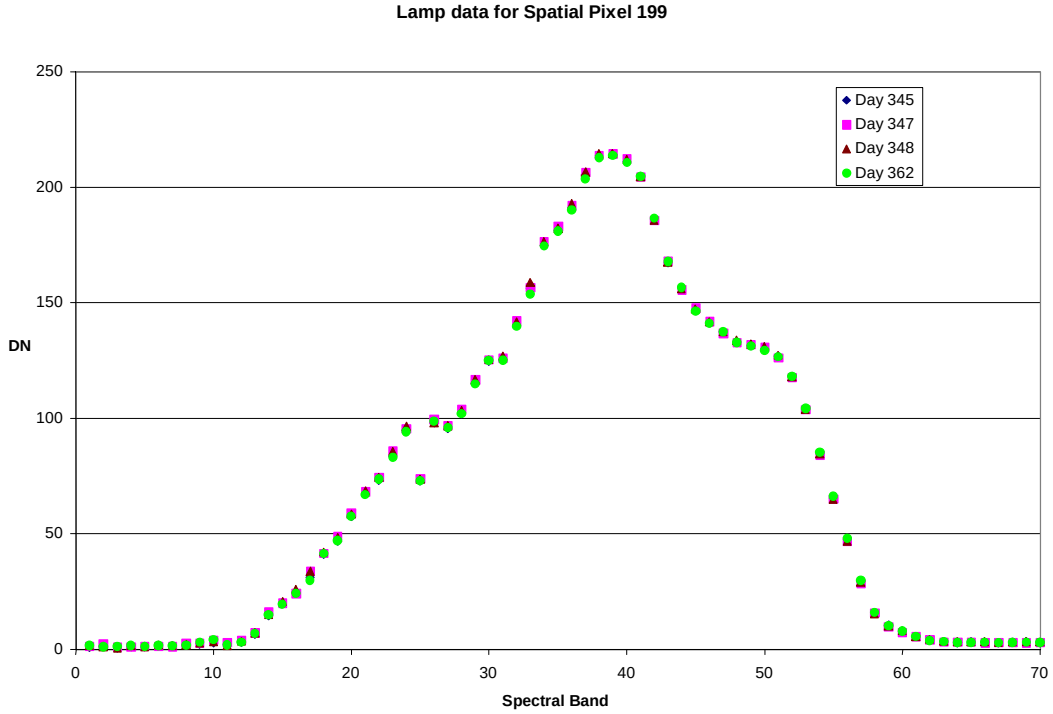

Figure 3.2-4: Dark subtracted lamp data for all DCEs examined. Note the comparable spread in the lamp data between the two quadrants. The dark subtraction removes the fixed pattern noise.

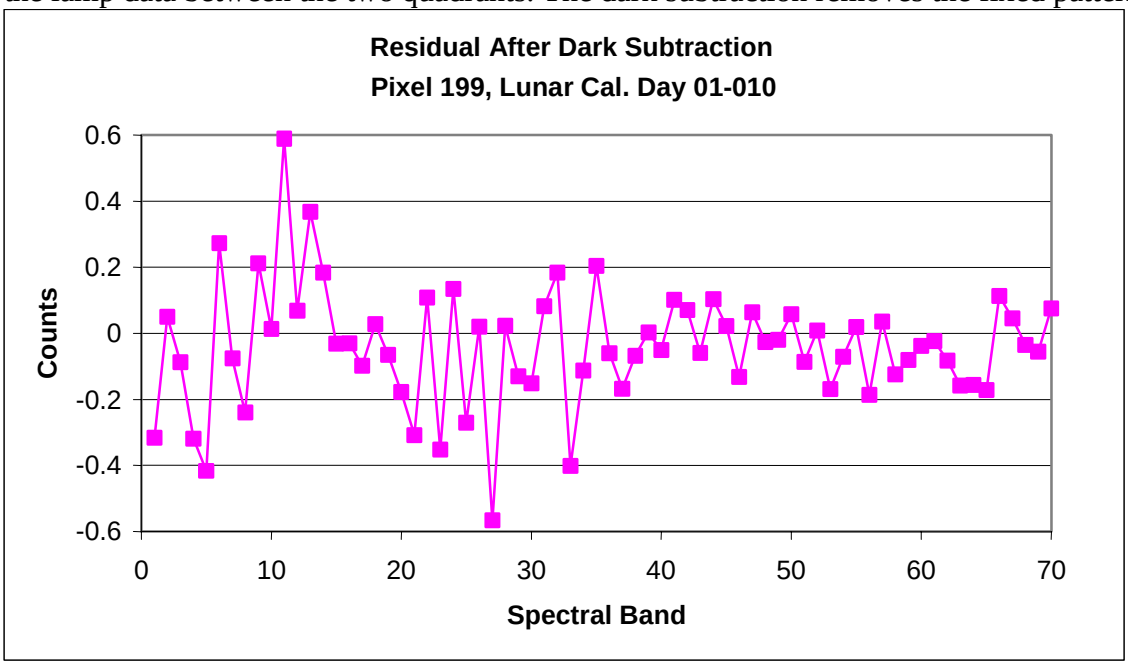

Figure 3.2-5: The residual "noise" after an average dark frame has been subtracted from an image frame that was not illuminated. Note that there is no evidence of the jigsaw pattern in the subtracted data, though the random noise is elevated in the affected quadrant.

3.2.2 VNIR Dark Drift and Residual

To insure the highest quality of data, it is important to determine if there is drift in the dark current over the course of a DCE.

To measure the drift, the dark level corresponding to each DCE that was processed for the Hyperion performance verification task was trended. Each of the three dark files was averaged in time. The difference between the pre-image dark and the post-image dark for a single point in each VNIR quadrant was trended. Table 3.2-1 provides a measure of the drift. Note that the value is negative since the dark increases as heat is generated with the VNIR ASP being powered during the DCE. It is interesting to note that although Quadrant D has the most significant pattern, Quadrant C has the largest amount of drift. Evidence of drift is also seen in Figures 3.2-3 and in the data presented in section 3.4 below. It was determined that the Level 1 processing would be modified to remove the drift in the dark. Any residual noise due to the drift would be due to the non-linearity in the drift. Figure 3.2-6 indicates how the dark signal varies as a function of time. It is based on the 2001 Day 10 Lunar Calibration event in which the moon was missed. From the 01-010 lunar calibration data, the drift can be considered linear with 0.2 DN being the estimated largest deviation from a linear trend.

For the dark image itself, the noise will be beaten down by the $\sqrt{N}$ statistics where N is the number of individual dark frames averaged together that is subtracted from the data. In the 1 second exposure, N~220 frames. Thus the sample noise in the worst quadrant with a standard deviation of ~3.25 DN (section 3.4.1) is reduced to 0.22 DN for the averaged frame. Thus the data image has little to no additional noise introduced by subtracting the dark frame.

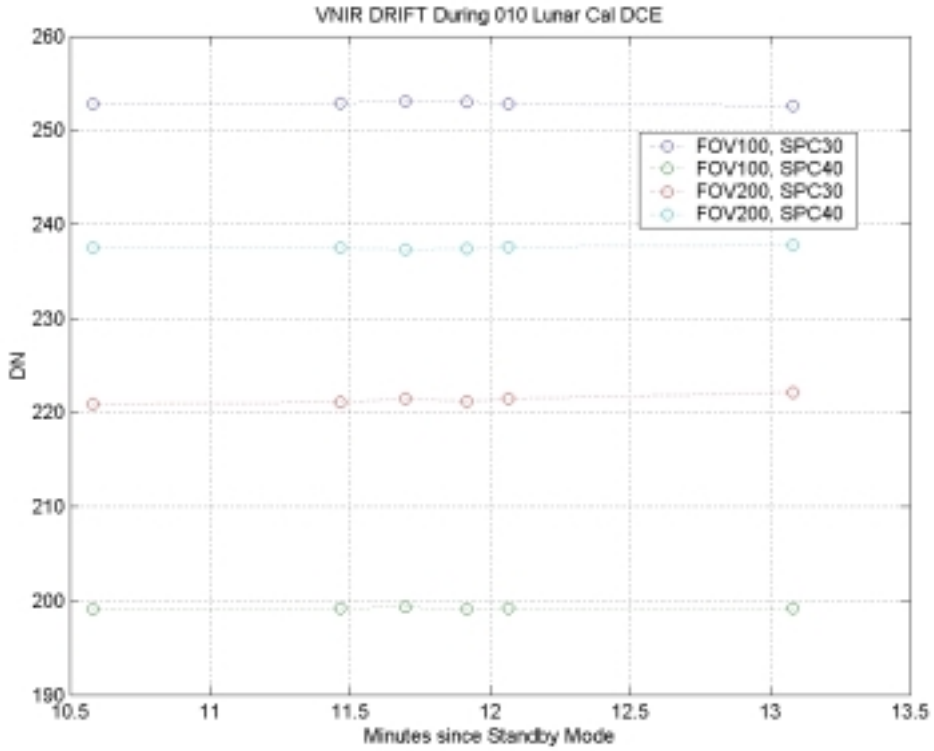

Figure 3.2-6 Mean Dark DN for specific pixels in the VNIR. Each pixel falls in a different Quadrant.

Table 3.2-1 VNIR Dark Drift

Quadrant:	A	B	C	D
Drift	-0.67	-0.45	-1.32	-0.69

3.2.3 VNIR Scatter

There is scatter that is evident in the VNIR. It is identified by the dark subtracted Lunar calibration file not going to zero at the wavelengths in which there should not be any signal detected. The pixels most significantly affected by scatter were removed from the Level 1 processing data product. The residual effect is estimated to be 0.75%. This is based on looking at the Day 038 Lunar Calibration data set and comparing the signal at the spectral edges with a near maximum signal.

3.3 VNIR Artifacts

Two artifacts have been seen in the VNIR data.

3.3.1 Pattern in the VNIR data

The cause of this pattern noise is not certain, but is believed to originate at the CCD.

3.3.2 Crosstalk in the VNIR Image

Over the course of the characterization effort, some images were obtained which have very bright objects in part of the frame and very dark areas in the rest of the image. Examples of this are the lunar calibration images, the Ross Ice Shelf, and sites with islands in a dark ocean. When looking at the details of these images, a low level "ghost" image was seen in the shorter wavelength spectral channels, corresponding to quadrants C and D.

The effect in the lunar image is shown at a greatly stretched intensity scale in Figure 3.3-1. Here, the ghost is measured against a zero background at 8 counts with the image being ~900 counts, or ~0.9% effect. Of all cases examined, this appears to be the worst case.

Figure 3.3-2 shows an image of the Ross Ice Shelf where the ghost is seen against a background of ~100 DN. The ghost behavior is very different in this image, showing up as a negative image against the background. The effect is approximately 0.4% of the positive image.

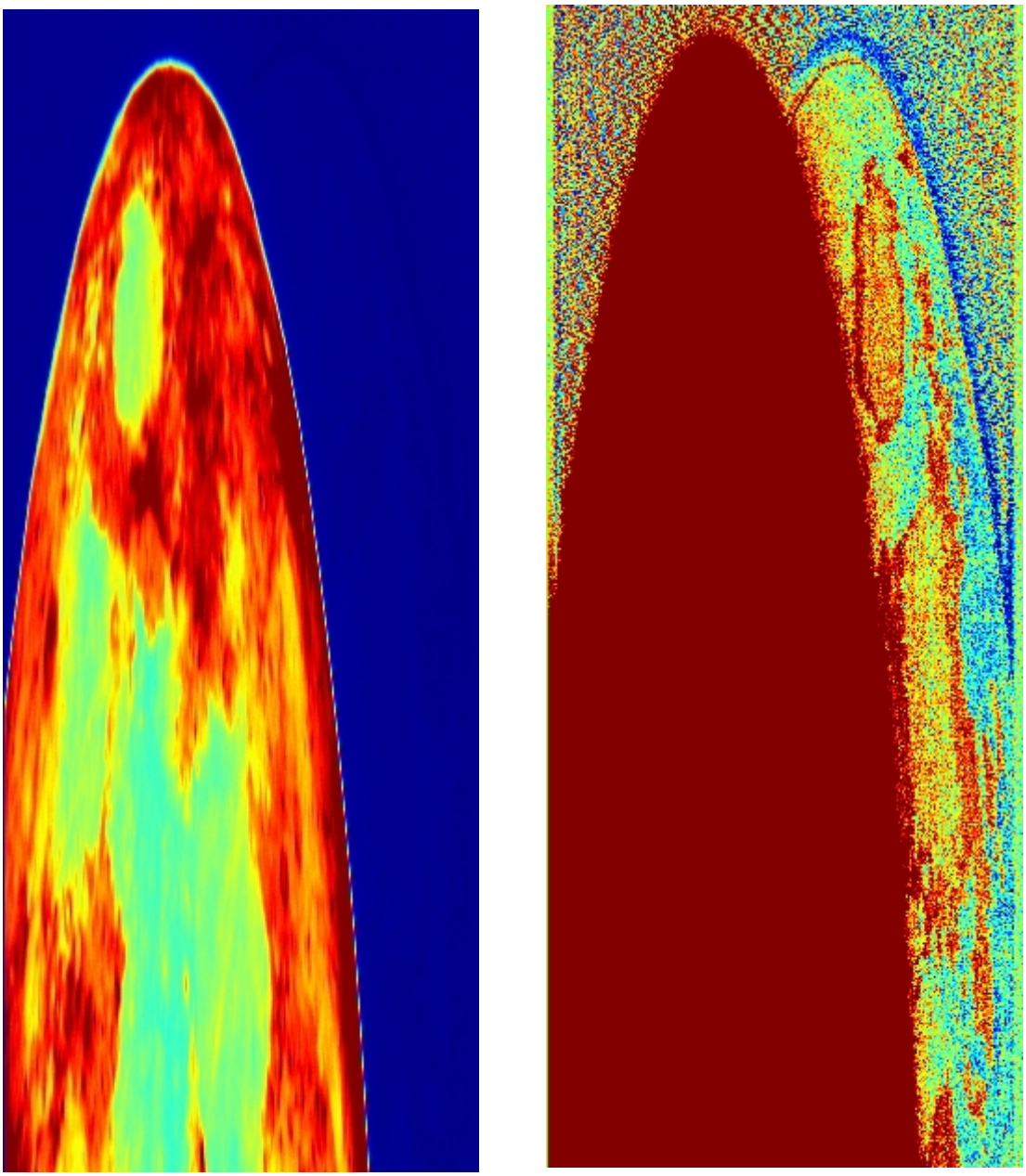

Figure 3.3-1: Lunar calibration image in spectral band 28 (quadrants C and D). “Ghost” image can be seen in the right picture at a very low level. The picture is a mirror image of the actual image seen to the left.

This effect is in all cases a mirror image and only seen in the short wavelength quadrants C and D.

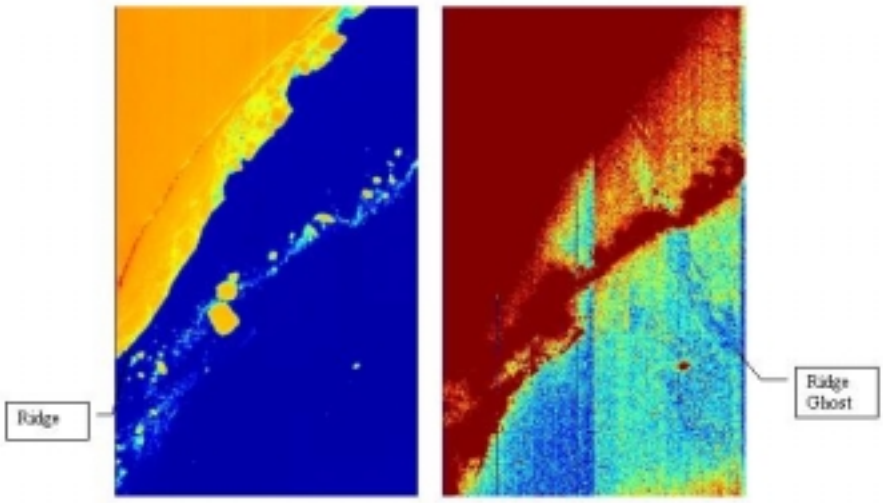

Figure 3.3-2: Ross Ice Shelf image showing a negative ghost.

3.4 VNIR Sources of Noise and Their Characteristics

3.4.1 Readout Noise

The noise in the dark frames is calculated by taking the standard deviation of a single pixel through the 220 samples of a single dark frame. This is done for every pixel in the detector and is referred to as the temporal noise. This measured noise will be a contributor to the error in the data frames, which cannot be measured in a scene where the scene is varying significantly from frame to frame. This should reflect the readout noise of the detector and associated electronics plus a component due to shot noise from the VNIR dark current (which is very low and should not be a significant contribution).

Two unexpected phenomena were seen in the behavior of the VNIR noise. The first is sensitivity to VNIR ASP temperature, which was discovered during ground testing. The second is sensitivity to signal level that is not simply due to increased shot noise (section 3.4.3). In an effort to characterize these effects, the data in Table 3-1 were examined in detail and the results are presented below.

Sensitivity to VNIR ASP Temperature:

The sensitivity to ASP temperature was characterized in ground testing. It was determined that operating the VNIR ASP at a temperature between 32-34°C would minimize the noise. The on-orbit data showed an increase in the noise compared to the final values on the ground. Tests were performed to recharacterize the temperature variation on-orbit. The VNIR ASP temperature was changed by setting the control temperature of the VNIR ASP heaters to values from 20°C up to

38°C for different DCEs. The measured noise of the 4 quadrants of the CCD is plotted in Figure 3.4-1 as a function of ASP temperature for both the ground tests and when on-orbit.

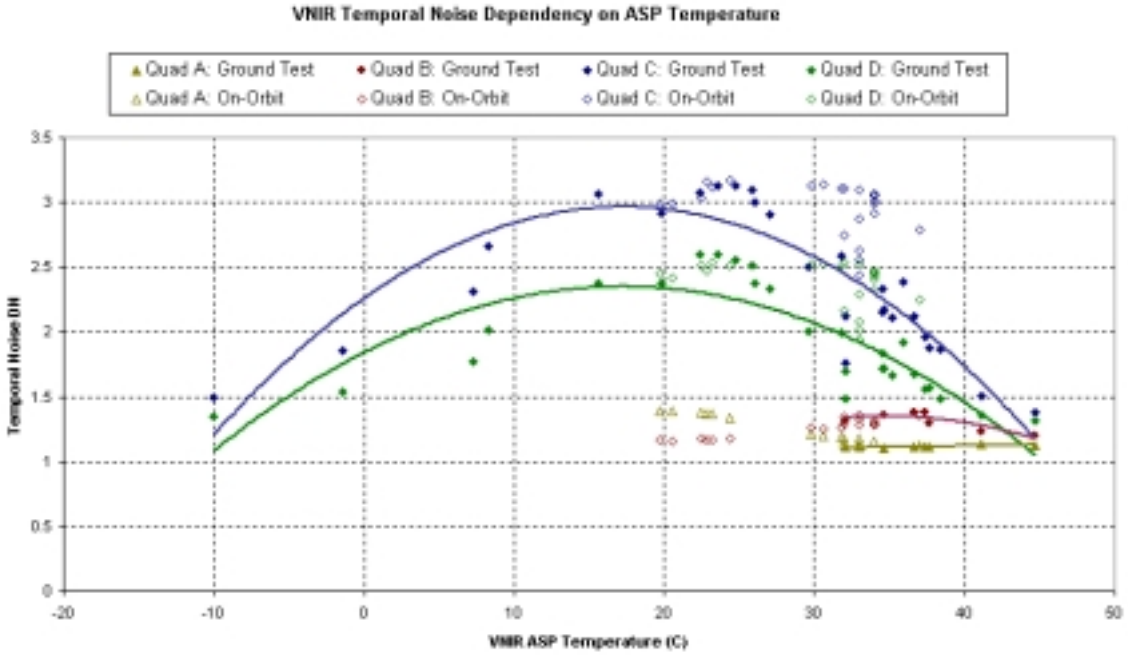

Figure 3.4-1: VNIR noise v. ASP temperature by quadrant.

It was found that at the lowest set temperatures the heaters were able to maintain the desired temperature when in idle mode, but that the ASP would heat up above the setpoint during the DCE when in standby and imaging mode. The temperature plotted is the setpoint temperature. For operational temperature >30°C, the VNIR ASP remained within the limits throughout the DCE. No significant improvement was seen at higher or lower ASP temperatures on orbit. Marginal improvement was seen at the highest temperatures but these cannot be maintained safely given power availability and potential additional stress on the electronics, which could reduce the overall lifetime of the instrument.

Sensitivity to Signal Level:
In addition to being reflective of the readout noise, the VNIR temporal noise should be a function of the illumination level and can be measured in the lamp images since the shot noise from the photo-generated electrons will also contribute. However, both ground tests and on-orbit data show the peculiar behavior that the first 10 to 15 spectral channels in the VNIR have elevated temporal noise in the lamp images compared to the other spectral bands even though the signal level is lower. This is shown in Figure 3.4-2.

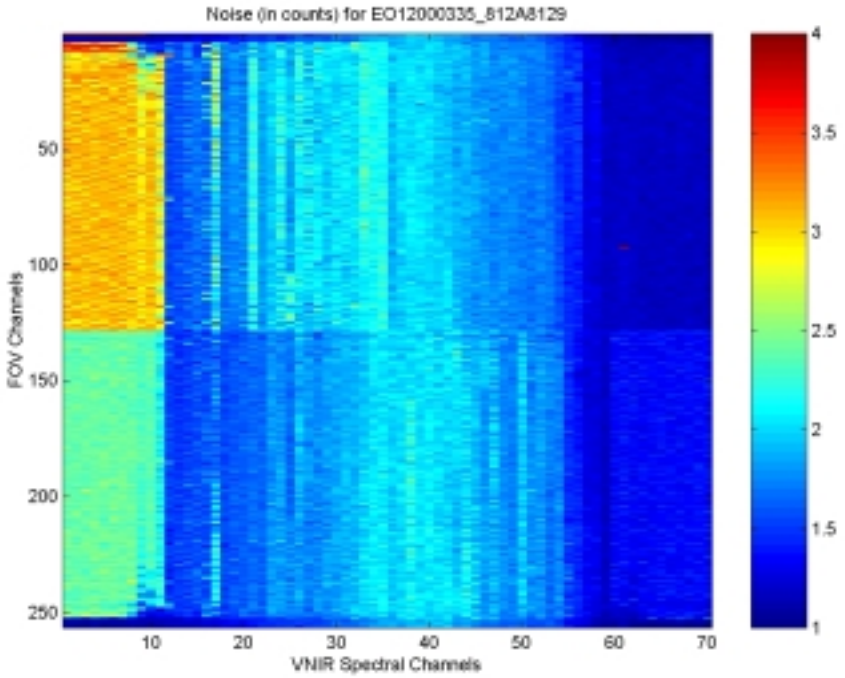

Figure 3.4-2: Noise in the VNIR lamp image observed in early on-orbit data. Wavelength increases from left to right.

Note that the first dark image from the solar calibration data set (day 00-347) was not used as it contained only 20 lines of data. For comparison purposes, statistics were also obtained for the solar image in the solar calibration DCE.

Data Analysis:
The data both within and between DCEs are very consistent so only representative data are presented. Figure 3.4-3 is illustrative of the consistency as it shows all of the dark frames examined for spatial pixel 52 in this study.

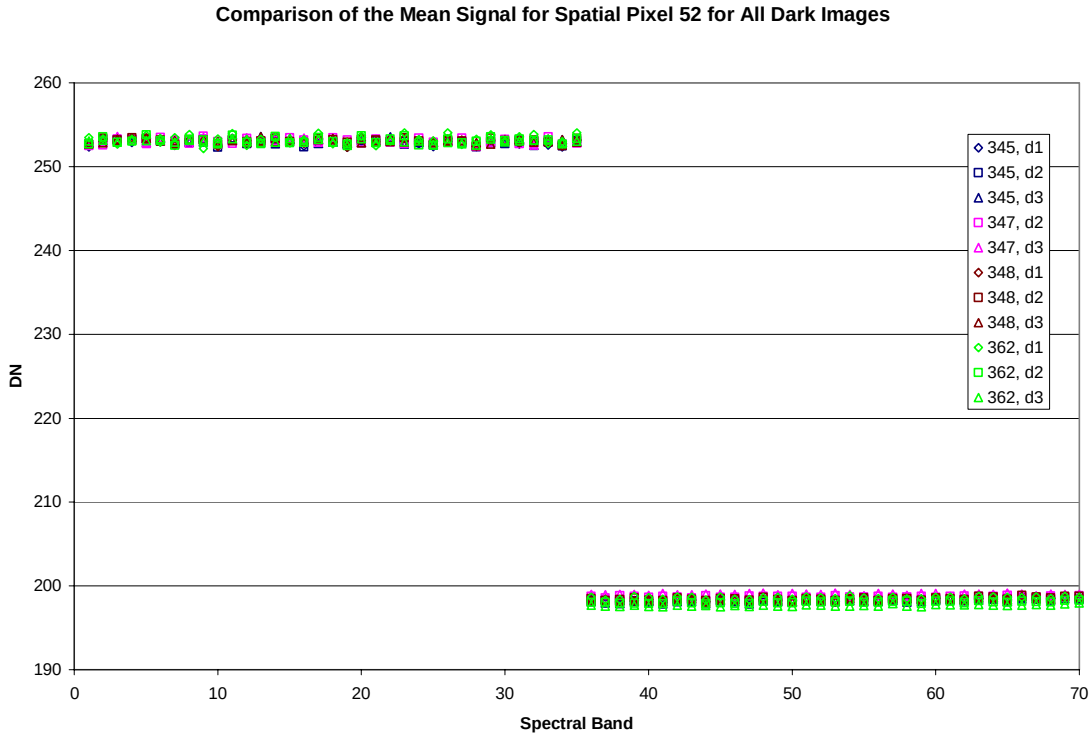

Figure 3.4-3: Mean signal for all the dark image data. "d1" = first dark image (before science data collect), "d2" = second dark image (after science data and before lamp data), "d3" = third dark image (after lamp data collect). Spectral channels 1-35 are in quadrant C and 36-70 are in quadrant A for this spatial pixel.

Using these methods we compared the noise in the dark and lamp frames. We found that the standard deviation in the lamp image is not elevated in the first few short wavelength spectral channels but that the noise in the remainder of those two quadrants is lower in the lamp image than in the dark frame itself. After the 12th spectral channel, the noise in the lamp image appears to be shot noise dominated and is comparable to the longer wavelength quadrants. In the dark images, the noise level in quadrants C and D is significantly greater than in quadrants A and B by a factor of 2 to 3. This is demonstrated in the day 347 data shown in Figures 3.4-4 and -5. The signal levels appear to be normal as shown in Figure 3.4-6, which is just the lamp signal after dark subtraction.

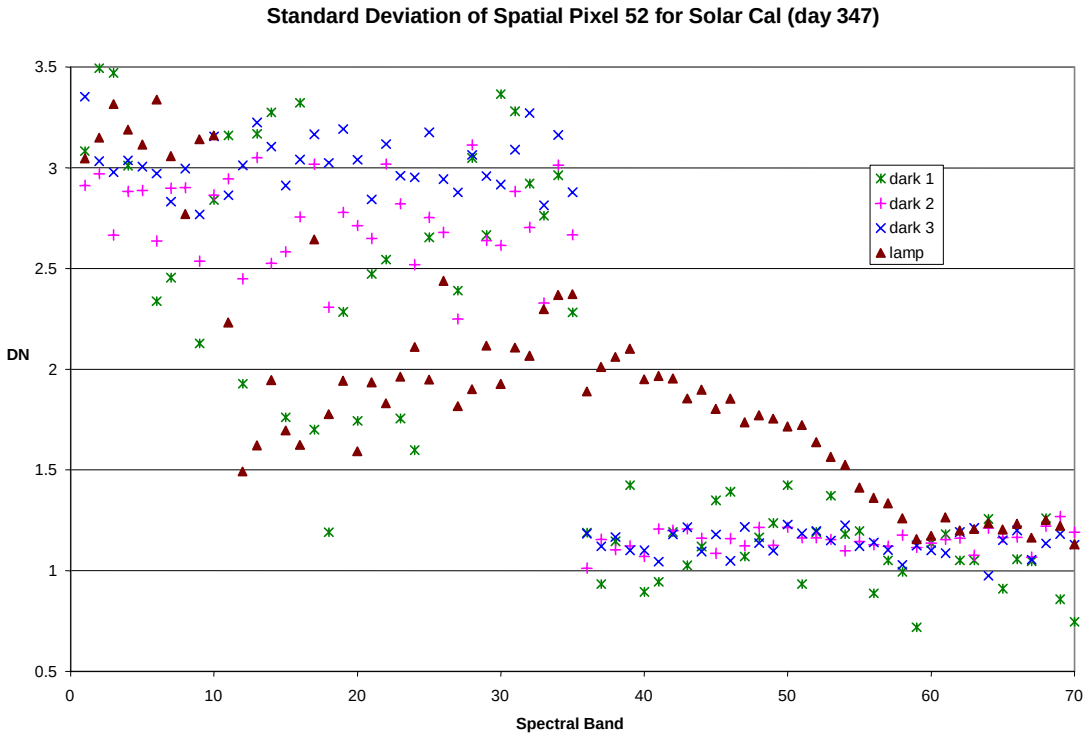

Figure 3.4-4: Noise in the dark and lamp data from the Solar Calibration DCE from day 347 for spatial pixel 52 (quadrants C and A). Notation is as in Figure 2.4.3-3 with "lamp" = lamp data.

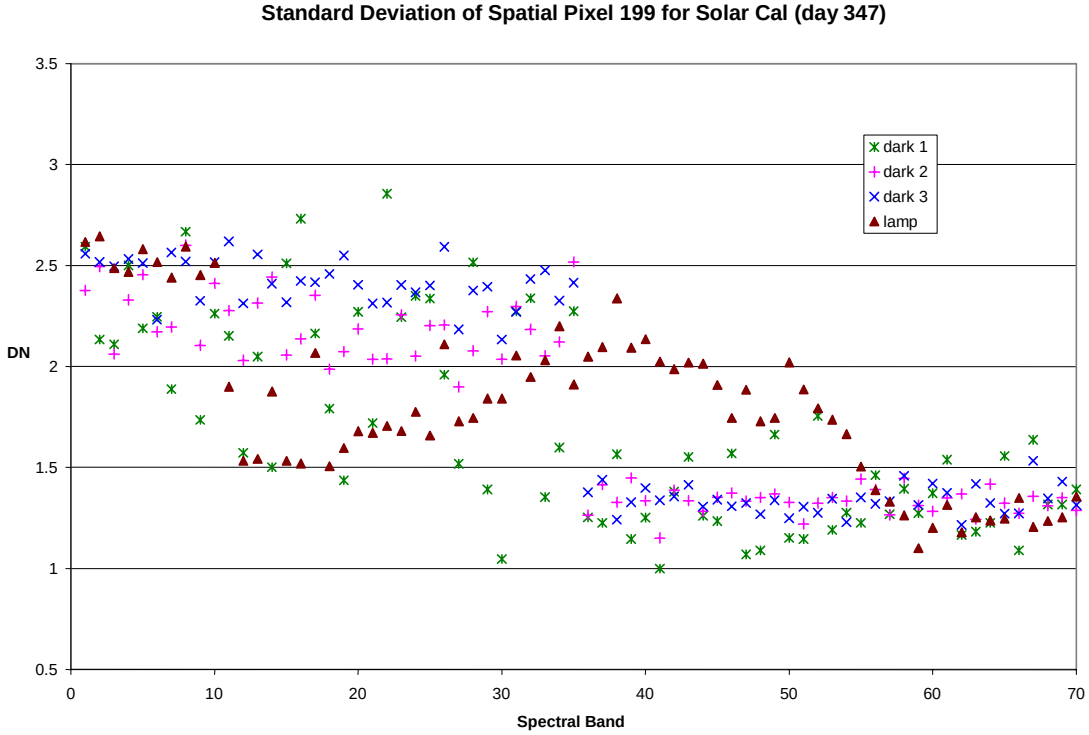

Figure 3.4-5: Same as Figure 3.4-4 for spatial pixel 199, which has spectral channels 1-35 in quadrant D and spectral channels 36-70 in quadrant B.

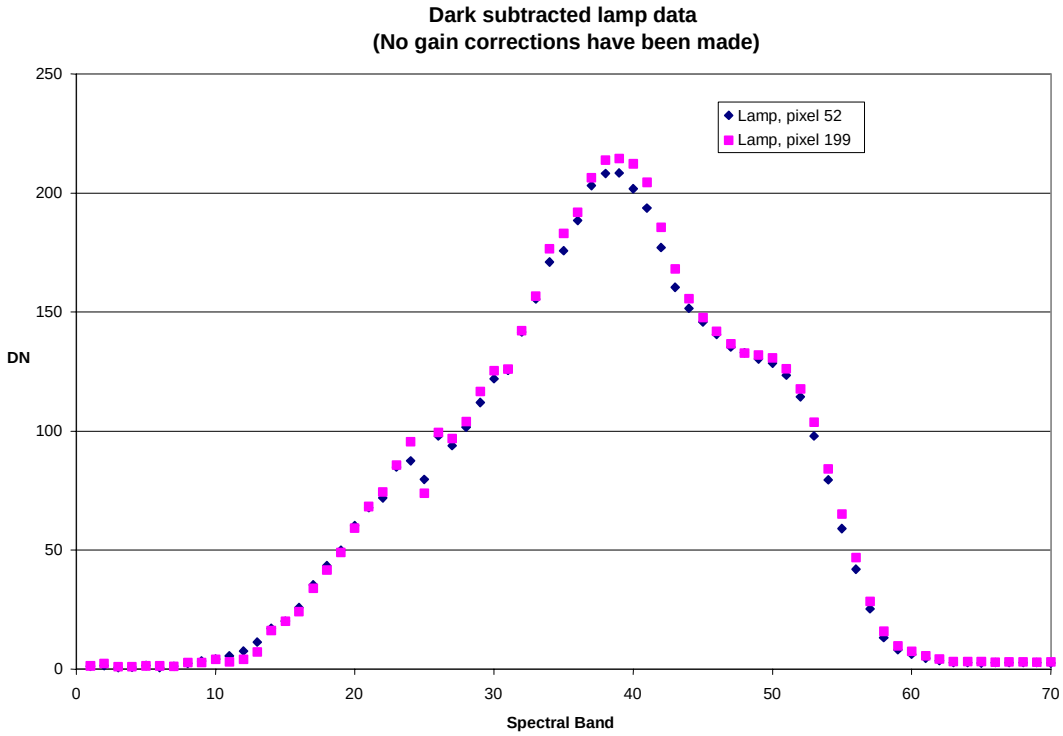

Figure 3.4-6: Dark subtracted lamp data for solar calibration data set. Note that no gain correction has been applied for pixel to pixel variations.

These data indicate that if the signal level is above a threshold value, the elevated noise is not present. The solar image data corroborates this as the elevated temporal noise is not seen at any wavelength with all signal levels >50 counts.

3.4.2 Quantization Noise

The data will have some induced noise simply due to the fact that the readout is only at 12 bit resolution so each electron does not have a corresponding digital value. The least significant bit corresponds to ~100 e^- in the VNIR electronics. Thus the minimum amount of noise present in a measurement is +/- ~50 electrons or ~0.5 DN.

3.4.3 Shot Noise

In addition to the readout noise, the primary source of noise in a CCD is the so-called “shot noise” which is simply due to Poisson statistics of the photo-generated electrons. In a theoretical sense it corresponds to the square root of the number of captured electrons, whether they were photo-generated or thermally generated in the form of dark current.

A plot of the dark subtracted signal v. noise for a solar calibration image is shown in Figure 3.4-7. The slope for each quadrant allows calculation of the measured noise as a function of signal level. As noted in 3.4.1, all quadrants show good performance at all but the lowest illumination levels.

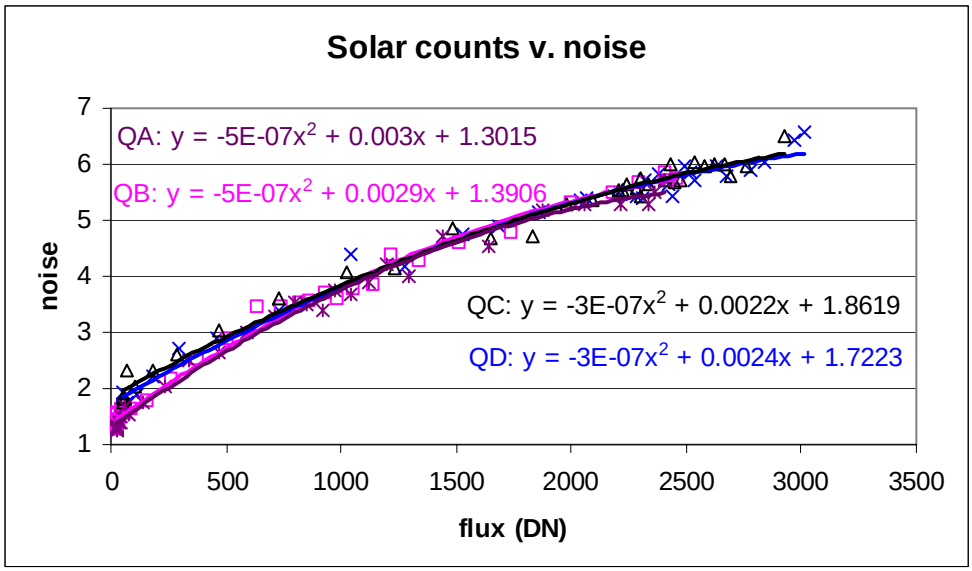

Figure 3.4-7: Signal v. Noise plot with a 2 dimensional polynomial fit done for each quadrant.

The requirements for SNR in the VNIR are listed in Table 3.4-1 and 3.4-2 below along with the measured noise at the specified signal level. The defined signal level is reference to the radiance level one would expect for 30% albedo scene, 45-degree latitude north with 60 degrees solar zenith angle. The VNIR SNR exceeds requirements and is consistent with the ground measurements. This is considered the single sample noise. The precision of the VNIR is discussed in section 5.5.

There will remain a single sample noise in the scene data of ~3.25 DN for very low illumination levels. The breakpoint based on the lamp data appears to be near 5 DN (4.5 DN for the upper left quadrant and 3.5 DN for the lower left quadrant). When the signal is above this level, the single sample noise is approximately 1.5 DN plus photon noise in all quadrants. As no performance requirements exist at low illumination levels, there is no impact on the instrument performance compared to the specification.

Table 3.4-1: Signal-to-Noise Ratio Requirements

Wave length (nm)	Defined Signal Level (W/m^2-s-um)	Required SNR to Exceed	On-Orbit Measured SNR	Ground Measured SNR
550	71.1	60	192	150
650	59.3	60	140	140
700	51	60	140	140

[1] Based on On-Orbit Responsivity File

Table 3.4-2: Signal-to-Noise Ratio Requirements

Wave length (nm)	Spectral Channel	Defined Signal Level (W/m^2-s-um)	Defined Signal Hyperion (DN^1)	Measured noise
550	20	71.1	590	3.06
650	30	59.3	494	2.88
700	35	51	509	2.90

[1] Based on Pre-Flight Measured Hyperion responsivity

3.5 VNIR Dynamic Range

3.5.1 Saturation

Direction was received from NASA/GSFC in 1999 to reset the gain on the Hyperion VNIR and SWIR focal planes so that they would saturate at 110% top-of-the-atmosphere solar radiance levels. It is easy to understand, therefore, that saturation is observed in very few scenes and to only a limited extent within these scenes. There are a few specific examples in which saturation occurs: cloud tops (VNIR only), (see Figures 3.5-1 and 3.5-2) hot spots within active volcanoes and artificial (man-made) flares such as the gas flares found at the Moomba oil fields in Australia (SWIR only).

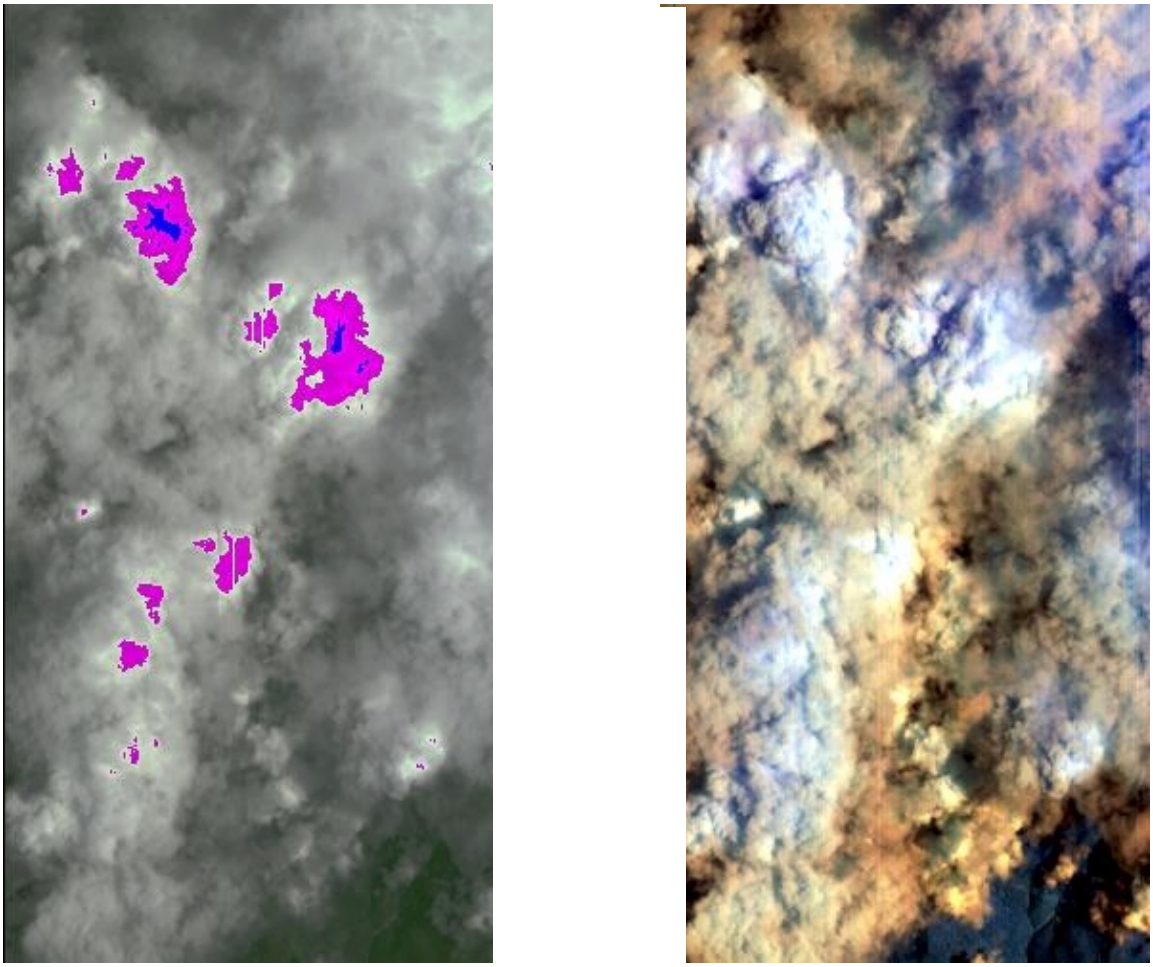

Figure 3.5.1 Example of VNIR Saturation: Image of cloud tops in which saturation is observed in the VNIR region of the spectrum but not in the corresponding SWIR image.

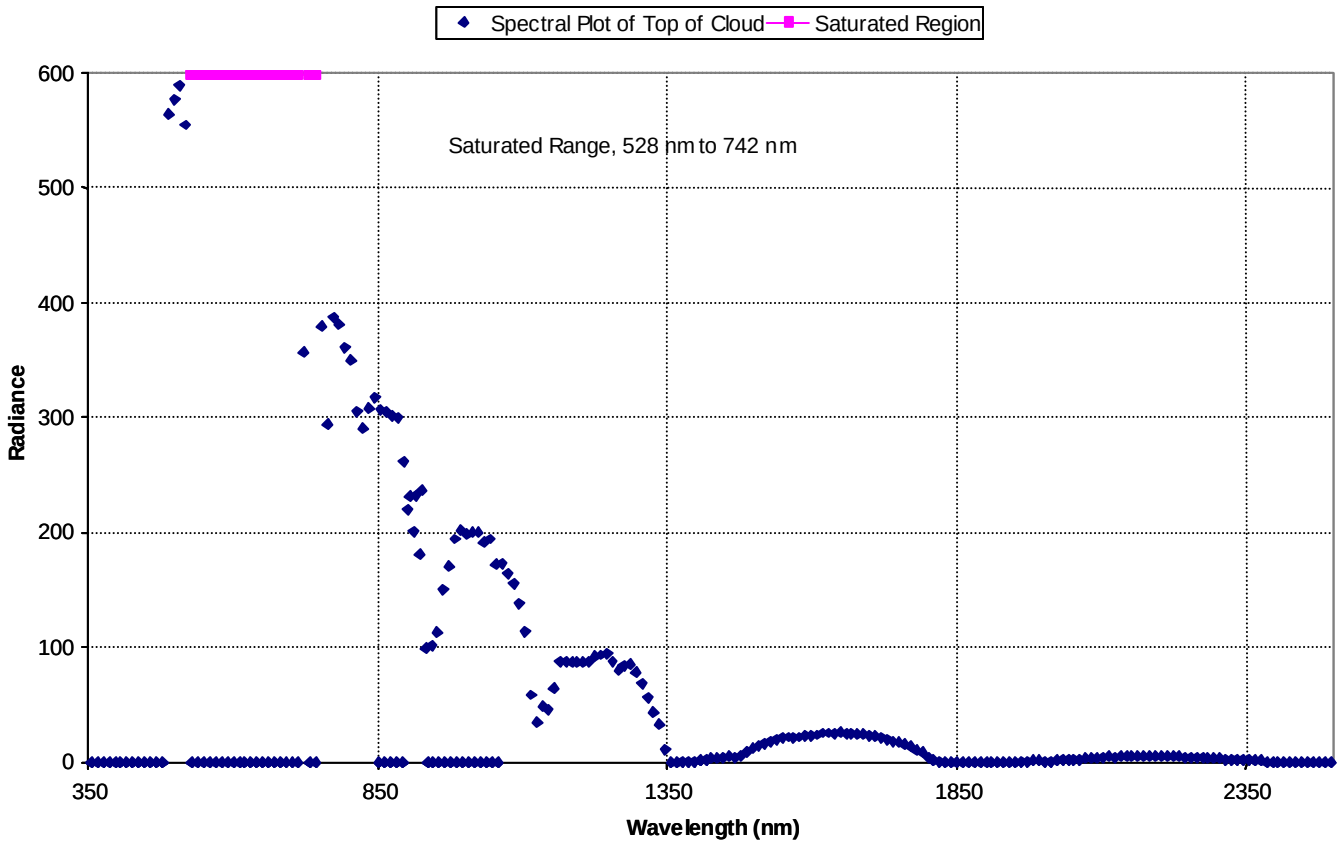

Figure 3.5.2 Radiance levels associated with the image in Figure 3.5-1 as a function of wavelength demonstrating the limited region in which saturation occurs. It should be noted that saturation on cloud tops has been very rarely observed during the instrument checkout period.

3.5.2 Linearity

Although there is no formal requirement on the linearity of the instrument, there is a flow down requirement on the linearity in order to meet the 6% radiometric accuracy over the dynamic range of the sensor. The flow down requirement stems from the sensor being calibrated at only one radiance level and the application of this calibration to the entire dynamic range of the instrument.

The responsivity of both the VNIR and SWIR were determined to be linear based on ground tests. A linearity on the order of 1% is required to meet the radiometric requirements. Linearity has not been measured on-orbit.

3.6 VNIR Repeatability

3.6.1 VNIR DCE-to-DCE Repeatability

The data set collected as part of the calibration lamp trending was used to assess the repeatability of the VNIR and SWIR. As is discussed in Chapter 5, the initial on-orbit output of the lamp was considerably (30-40%) greater than ground operation. Since that time, the output has been steadily decreasing. The Fig. 3.6-1 shows the trend of the calibration lamp output for a single wavelength in the VNIR and a single wavelength in the SWIR. This data set was used to assess the VNIR and SWIR DCE-to-DCE repeatability. A linear fit was applied to each band that was trended, and the difference between the actual lamp output and

the fit output was calculated. The standard deviation of this difference was calculated and two times this variation is taken as the DCE-to-DCE repeatability, see Table 3.6-1. Note that for this trending data set the signal for each band was averaged across the field-of-view range from pixel 50 to 200. The VNIR the repeatability is taken to be 0.60%

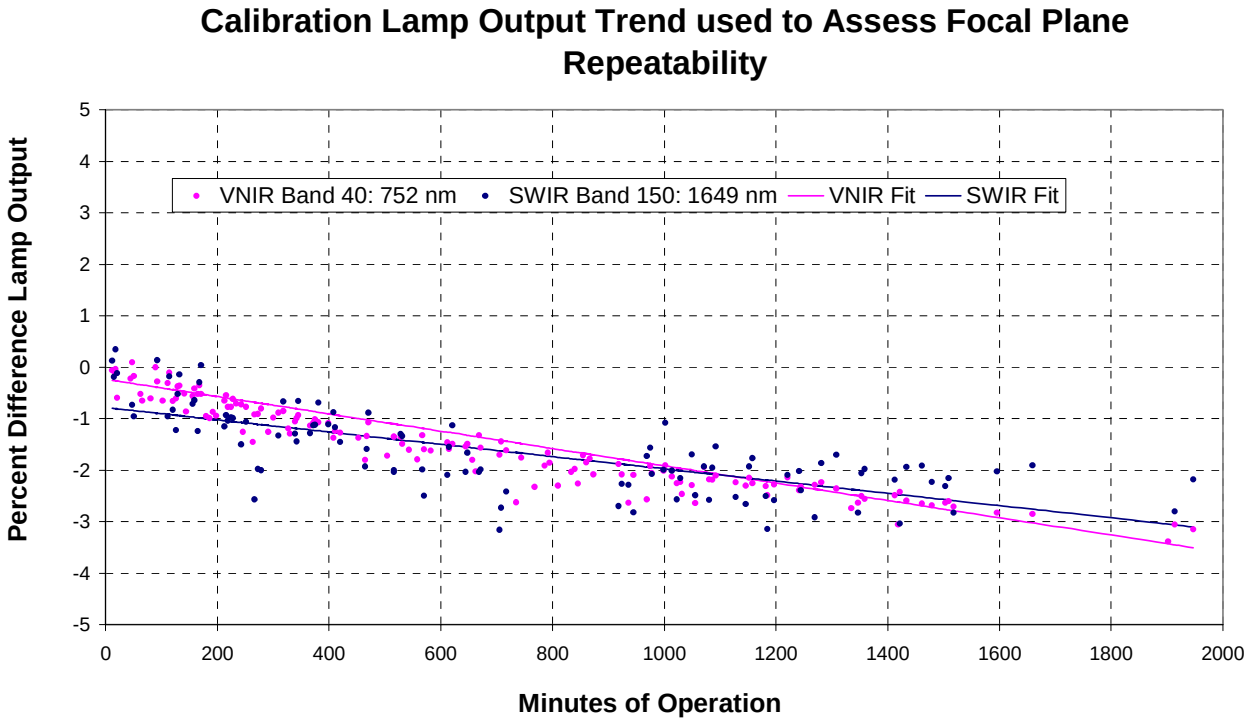

Figure 3.6-1 The calibration lamp trend data set was used to assess the instrument repeatability

Table 3.6-1 VNIR Repeatability

VNIR	Repeatability
Band 30	0.57
Band 34	0.56
Band 37	0.52
Band 40	0.43
Band 50	0.53

3.6.2 VNIR Pixel-to-Pixel Repeatability

The solar calibration data collects have the unique advantage of providing a collect that is, by definition, uniform across the field of view. A set of solar calibration collects were analyzed and compared with each other to determine how much the pixel response varied across the field of view. There are two types of variation. One in which one could consider the average focal plane response, and another in which the focus is the pixel to pixel variation in the response. The later is the focus in this section. The solar calibrations obtained on Day 047, 051, 054, 057, 061 and 068 were used. The on-orbit calibration file was adjusted in the field-of-view direction using Day 047. Hence for this analysis the average of each solar calibration event was compared with the one obtained on Day 047.

The ratio of each solar cal to the Day 047 solar cal was obtained. The standard deviation of the ratio across the field of view was calculated for each band. This was used as a measure for the pixel-to-pixel variation. For the VNIR the pixel-to-pixel variation was approximately 0.05 %.

3.7 VNIR Pixel Status

3.7.1 VNIR Outlier Pixels

The pre-flight calibration and the on-orbit calibration based on the pixel-to-pixel variation correction of the pre-flight calibration using Day 047 solar calibration were compared (see Figure 3.7-1). The comparison was used to identify pixels whose response changed more than the surrounding pixels and to identify dead pixels. The steps taken are discussed in the SWIR section 4.7.1.

There were no new dead pixels identified in the VNIR. There were pixels that were identified as outlier pixels. These are listed in Table 3.7-2 below. Outliers that were less than 5% different from the surrounding pixels were not included

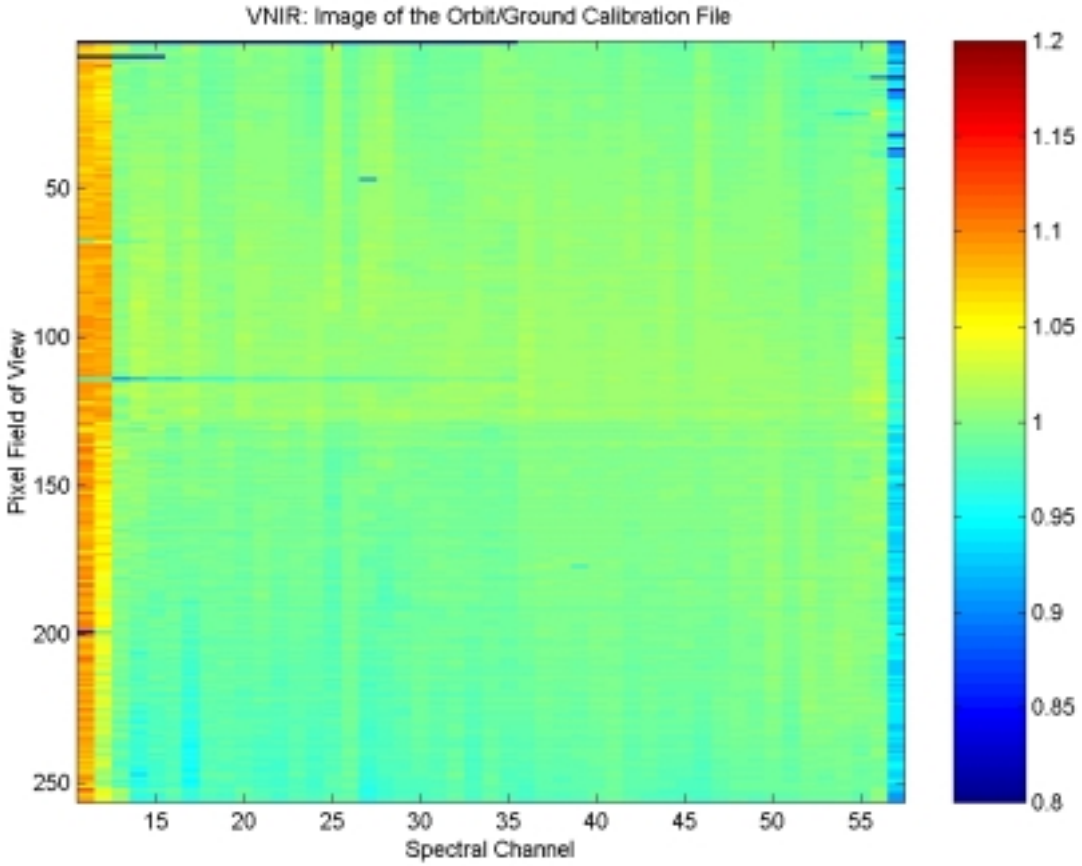

Figure 3.7-1 Ratio of On-Orbit Calibration file to Pre-Flight Calibration file.

Table 3.7-1 VNIR Outlier Pixels

Field of View Position	Spectral Channel	Percent Different
1	57	-8.8
6	11	-26.6%
6	12	-26.1%
6	13	-27.6%
6	14	-28.3%
13	56	-11.3%
13	57	-15.2%
17	57	-12.4%
25	54	-5.41%
32	57	-9.0%
37	57	-9.3%
177	39	-5.6%
199	11	-23.7%

3.7.2 VNIR Sensitivity to the South Atlantic Anomaly (SAA)

This discussion applies equally to the VNIR and SWIR. Browse images were routinely produced for Hyperion DCEs that were used for the performance verification check out. On select scenes, the images contained random pixels that stood out. This phenomenon was especially noticeable in the Nacunan data collect. The extreme pixels occurred randomly though out the VNIR and SWIR. The location of the extreme pixels varied spatially and spectrally. The scenes that contained extreme pixels were primarily in Argentina and in regions in South America. It is believed the extreme pixels are caused by the South Atlantic Anomaly. The effect was limited to the time of the data collect. For example, Los Menucos is taken 1 orbit before Cape Canaveral and there were no residual effects on the instrument observed in the Cape Canaveral scene.

Day 047 Nacunan: Many extreme pixels were noted.
Day 045 Los Menucos: Few extreme pixels were noted
Day 045 Cape Canaveral: No extreme pixels.

Day 048 Africa: No extreme pixels.

An enhanced particle flux is associated with the South Atlantic Anomaly, which penetrates the detector material and produces spurious signals. Single or multiple pixel events can be produced depending on the particle direction of travel. These can be produced at any time but the higher density in the SAA enhances the density of the occurrence of spurious pixels.

3.8 VNIR Summary

The VNIR focal plane has been discussed in detail. The process of dark removal was highlighted. The pattern noise seen in Quadrant D was reviewed with implications to the science data which is minimal since it was shown to be effectively removed. Drift was also studied and should have a negligible effect once corrected for as part of the level 1 processing. Scatter in the instrument was evaluated on-orbit and is discussed in more detail in section 5.0 The VNIR was also found to be sensitive to the South Atlantic Anomaly.

The VNIR noise was characterized using the data from a solar calibration event. The SNR meets requirements. Comparison of the on-orbit calibration file with the pre-flight calibration file was used to determine that there were no new dead pixels, and to identify pixels that warrant additional monitoring.

Cases of saturation in the VNIR were rare and when they occurred it was limited in the spectral direction. Trending of the lamp was used to assess the repeatability of the focal plane.

The influence of each of the topics discussed in this chapter were assessed. In section 5.5 the terms are combined to create an overall precision error. The VNIR precision error is 2.2 % and is a combination of repeatability, calibration drift, residual artifact and residual dark field removal errors. Overall the VNIR has indicated consistent and stable performance. There are a minimal number of pixels whose responsivity vary more than the surrounding pixels. When they occur, the resulting image appears to have streaks.

4 SWIR FOCAL PLANE CHARACTERISTICS

This chapter discusses the performance characterization of the SWIR focal plane. Discussion of the dark removal is presented as well as discussions on SWIR smear and echo artifacts. Focal plane repeatability, and noise are evaluated.

The data in Table 4-1 was used to characterize various aspects of the SWIR focal plane and are referred to in following sections.

Table 4-1

Day	Image	Used for
01-010	Lunar Calibration (missed moon)	Drift
01-032	SWIR Spectral Test	Drift
01-037	Erta Ale Night	Echo/Saturation
01-008	Moomba	Echo/Saturation
01-025	Moomba	Echo
01-056	Moomba	Echo
01-038	Palmyra Syria	Edge Echo
01-038	Lunar Calibration	Scatter
01-047	Solar Calibration	Outlier Pixels
01-47 to 61	Solar Calibration	Pixel-to-Pixel

4.1 SWIR Introduction

4.1.1 SWIR Focal Plane Description

The HgCdTe shortwave infrared (SWIR) FPA was developed specifically for hyperspectral imaging applications. This 2-D FPA has 256 x 256 pixels of 60 μm pitch and a custom pixel readout integrated circuit that is highly linear at low photon flux levels. For the Hyperion instrument, only a 172 pixel (spectral) x 256 pixel (spatial) section of the FPA was used. The spectral bandwidth for each pixel is approximately 10 nm.

The SWIR is maintained at operational temperature by a cryocooler that is connected to the sensor via a thermal strap. The cryocooler setpoint temperature is 110 K.

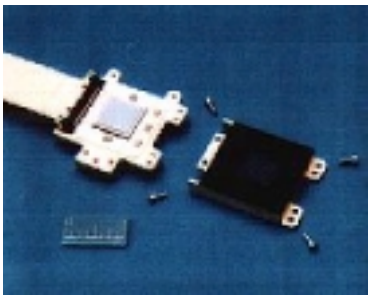

4.1.2 SWIR Focal Plane Readout Process

The SWIR FPA contains 256 spectral x 256 spatial pixels of which 172 spectral and 256 spatial pixels are digitized and stored. The FPA has four readout channels.

4.1.3 SWIR Focal Plane Thermal Cycling

The SWIR is maintained at operational temperature by a cryocooler that is connected to the sensor via a thermal strap. The cryocooler setpoint temperature is 110 K for the cooler coldblock. The SWIR-FPE is typically 8-10K warmer. Due to contamination within the instrument acquired during spacecraft testing, the cooler is able to maintain the operational temperature for a limited amount of time. The contamination deposits on the cold surfaces, changing the emissivity of the cold surfaces and effectively increasing the heat load on the cooler. As a result, the cooler must periodically undergo thermal cycling in which the system is allowed to warm up to permit the contaminants to desorb. This causes the SWIR FPA to undergo periodic thermal cycles.

The manufacturer of the SWIR FPA guaranteed that the FPA would survive 100 thermal cycles. Previous experience, however, indicates that focal planes that survive the initial thermal cycles last much longer than the average cycle lifetime would indicate.

During each data collection event (DCE), data from the VNIR and SWIR are collected. SWIR data may be provided whether or not the SWIR was at the proper operational temperature. The telemetry should be reviewed for verification of the proper operational temperature. The absolute calibration is only valid if the SWIR is at the proper operational temperaure of 110 ± 0.25K. It has been noticed that, at higher temperatures, SWIR data may consist of zeroes.

4.2 SWIR Background Level Removal

4.2.1 SWIR Dark Drift and Residual

The instrument is nominally in idle mode. The instrument is commanded to standby mode 10 minutes before a Hyperion DCE sequence is obtained. When the instrument is commanded to standby mode the VNIR and SWIR Analog Signal Processors (ASPs) are powered. The powering of the SWIR ASP increases the heat load on the cryocooler. The 10-minute wait period was designed to allow the SWIR FPA to return to thermal equilibrium prior to the DCE sequence. While the SWIR FPA is transitioning to thermal equilibrium the SWIR dark level is also transitioning. The difference between the dark collect obtained before and after the image is referred to the dark drift.

The drift of the SWIR dark was reviewed during the on-orbit check out period. Figure 4.2.1-1 below presents the difference between pre- and post-image dark for two selected points on the SWIR focal plane that were trended for each DCE processed.

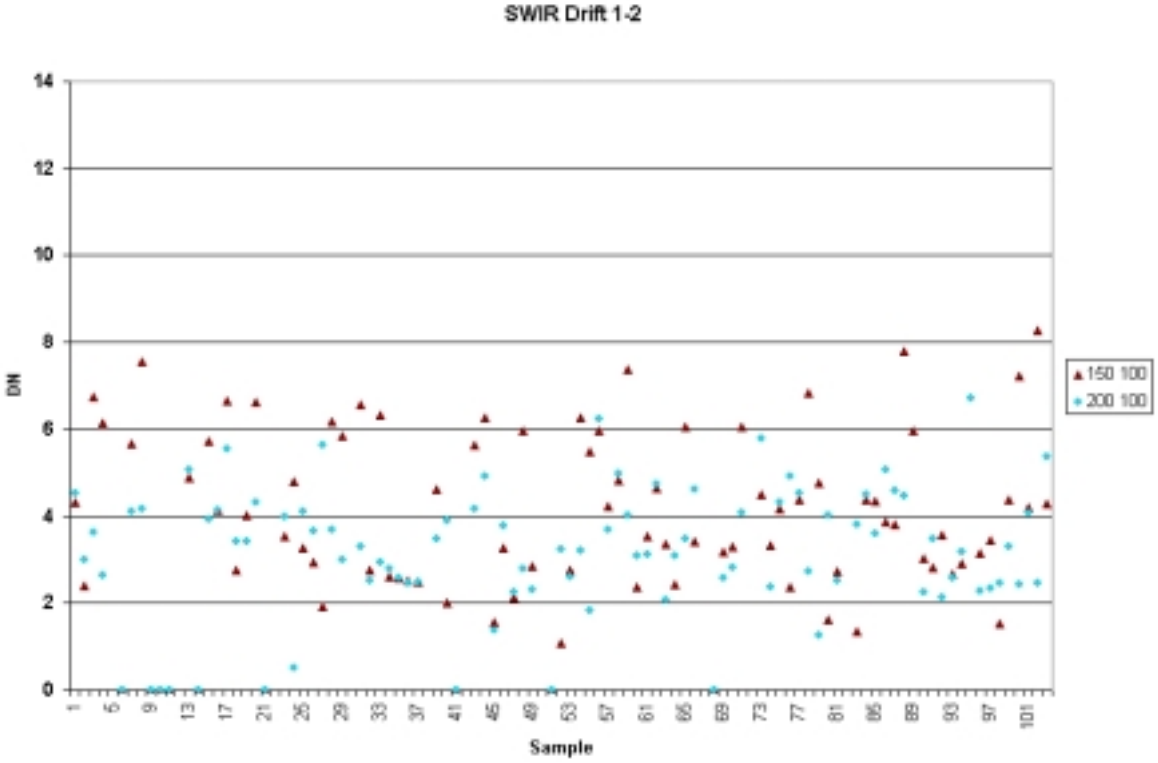

Figure 4.2.1-1 Difference between pre- and post-image dark for two select points on the SWIR focal plane trended for each DCE processed.

Hyperion on-orbit data was analyzed to verify that the dark drift was a linear effect. The Day 010 Lunar Calibration DCE missed the moon, so the image data set covered deep space and provided an effectively dark collect. Four simulated dark frames were subset from the image. Plotted in Figure 4.2.1-2 is the average number of counts (DN) as a function of minutes since Standby mode was commanded for four select points in the SWIR. The drift is sufficiently linear over the time scale of the DCE.

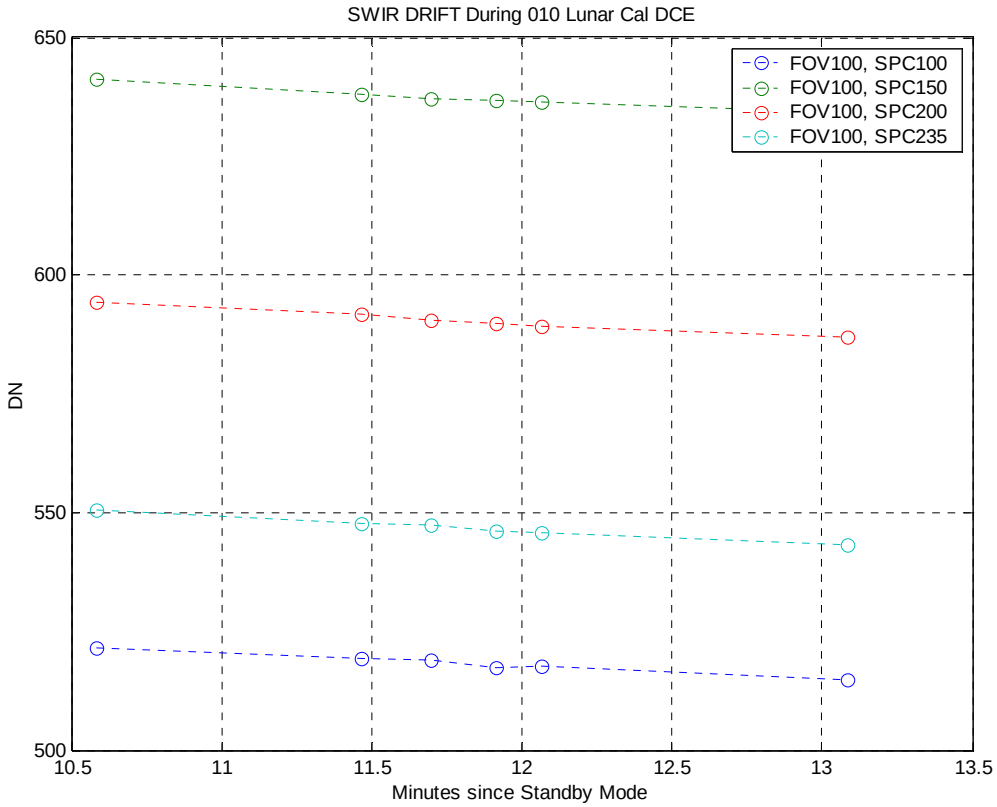

Figure 4.2.1-2: SWIR drift is linear

Level 1 processing uses an interpolation scheme to eliminate any significant contribution of the drift to the noise. The residual error is estimated to be 0.05%

4.2.2 SWIR Scatter

There is optical scatter evident in the SWIR image data. It is identified by the dark subtracted Lunar calibration file not going to zero at the wavelengths in which there should be no signal detected. The pixels most significantly affected by scatter are not included in the Level 1 processing data product because there is negligible response from the SWIR focal plane at these wavelengths. The residual effect is estimated to be 0.5% based on a comparison of the Day 038 Lunar Calibration data set and the signal at the spectral edges with a near maximum signal.

4.3 SWIR Artifact Removal and Residual

The SWIR has two known artifacts, SWIR Smear and SWIR Echo. These artifacts were detected and analyzed during ground testing. On-orbit data collects were reviewed to assess the effectiveness of the algorithms on orbit.

4.3.1 Smear in the SWIR data

SWIR Smear is the leakage of signal from one pixel into the 'next readout' pixel in the spectral direction. This artifact is effectively removed during level 1 processing, as shown in Figure 4.3.1-1.

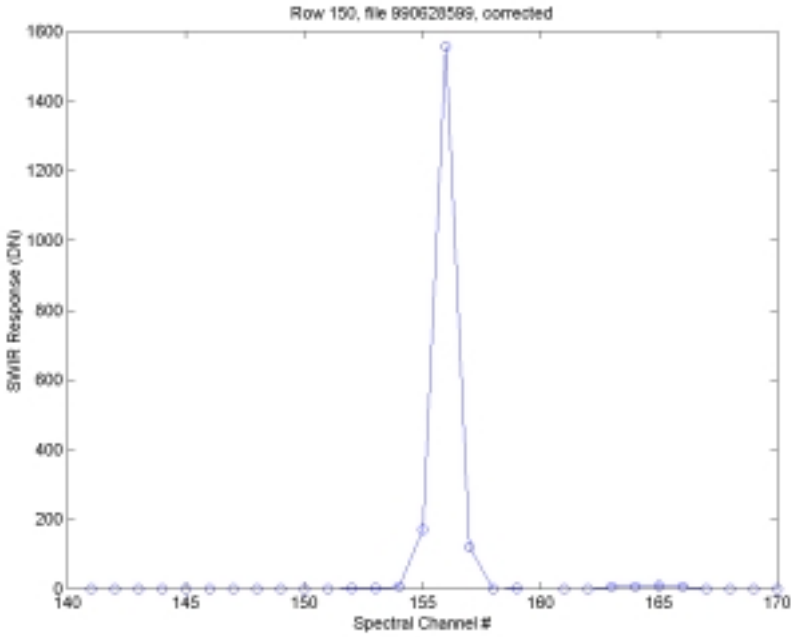

Figure 4.3.1-1. Example of artifact removed. (Note: This data was obtained during TRW testing so the spectral channel number ordering is reversed.)

4.3.2 Echo in the SWIR image

Echo in the SWIR is an artifact where signal from one image "echos" into a later pixel. Echo has about a 6.5% magnitude, and the echo occurs later in time but within the same spectral channel.

Frame Echo:
Investigating echo on-orbit requires data that has a significant feature with a dark background. The night collect of a hot-gas flare such as Moomba and the image of active volcanoes are good examples for this analysis

Various Moomba data sets were analyzed. The Moomba data was processed with and without the echo correction applied.

The results from the Moomba flare present in the Day 056 collect is presented in Figure 4.3.2-1. The first image is a data set processed without the echo correction. The uncorrected data was averaged over the spectral bands. A spatial subset of the entire scene is presented as log base 10. The gas flare as well as the echo and negative echo are indicated. Figure 4.3.2-2 is an image of the same data set processed with the echo correction. The corrected data was averaged over the spectral bands and again is log base 10. This image visually indicates the echo correction is working. The accuracy of the echo correction was measured by comparing the echo, and the residual of the echo with the source.

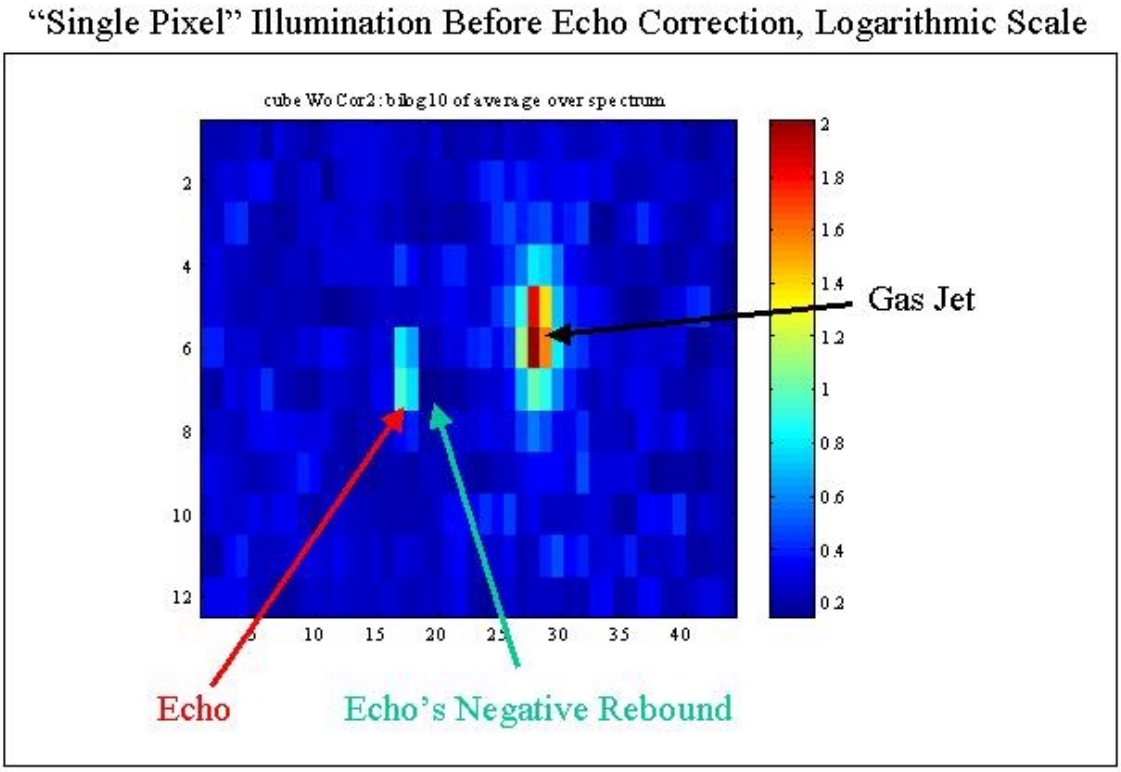

Figure 4.3.2-1 Example of Uncorrected Scene of the Moomba Flare

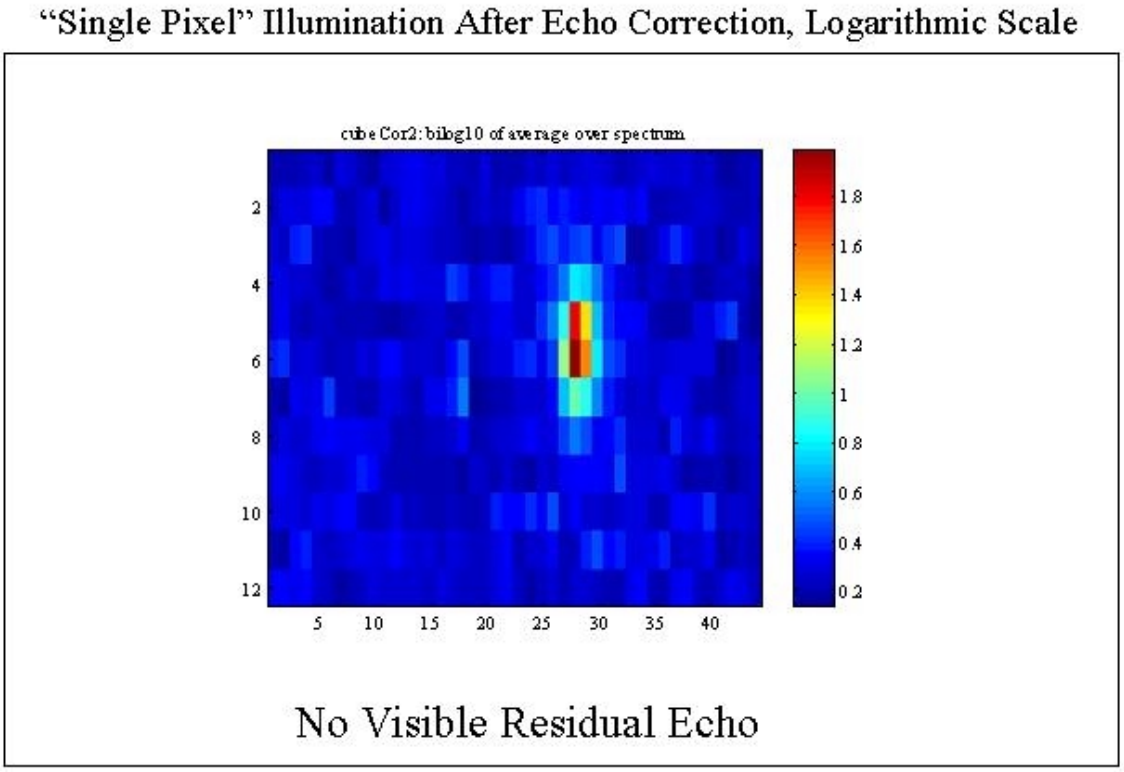

Figure 4.3.2-2 Example of Corrected Scene of the Moomba Flare

Table 4.3.2-1 below indicates the peak value of the source as well as the percent signal for the echo, the residual echo and the echo negative rebound. The units of the source signal is 10 multiplied by the radiance, averaged over the spectral wavelengths, then log 10. Hence, it is a relative unit. The residual echo is less than 0.8% of the source and the negative rebound is comparable to the residual. The current Level 1 processing code does not correct for the negative rebound echo. A residual echo error of 0.8% is assumed.

Table 4.3.2-1 Summary of Moomba Echos

	Source	Echo	Residual Echo	Negative Rebound
Location 1	42	5.8%	0.77%	0.67%
Location 2	101	6.9%	0.60%	0.41%

4.4 SWIR Sources of Noise and Their Characteristics

4.4.1 Readout Noise

The noise in the dark frames is calculated by taking the standard deviation of a single pixel through the 220 samples of a single dark frame. This is done for every pixel in the detector and is referred to as the temporal noise. This measured noise will be a contributor to the error in the data frames, which cannot be measured in a scene where the scene is varying significantly from frame to frame. This should reflect the readout noise of the detector and associated electronics plus a component due to shot noise from the SWIR dark current (which is low and should not be a significant contribution).

An image of the SWIR dark data and the SWIR noise is presented in Figure 4.4.1-1. The data are based on the first dark (pre-image) file collected during the DAY 047 Solar Calibration event. The noise in the dark file represents the readout noise and varies for the focal plane.

Included in Figure 4.4.1-2 is an image of the raw SWIR solar signal and variation of the solar data set. This was used to characterize the SWIR noise as a functional of signal level.

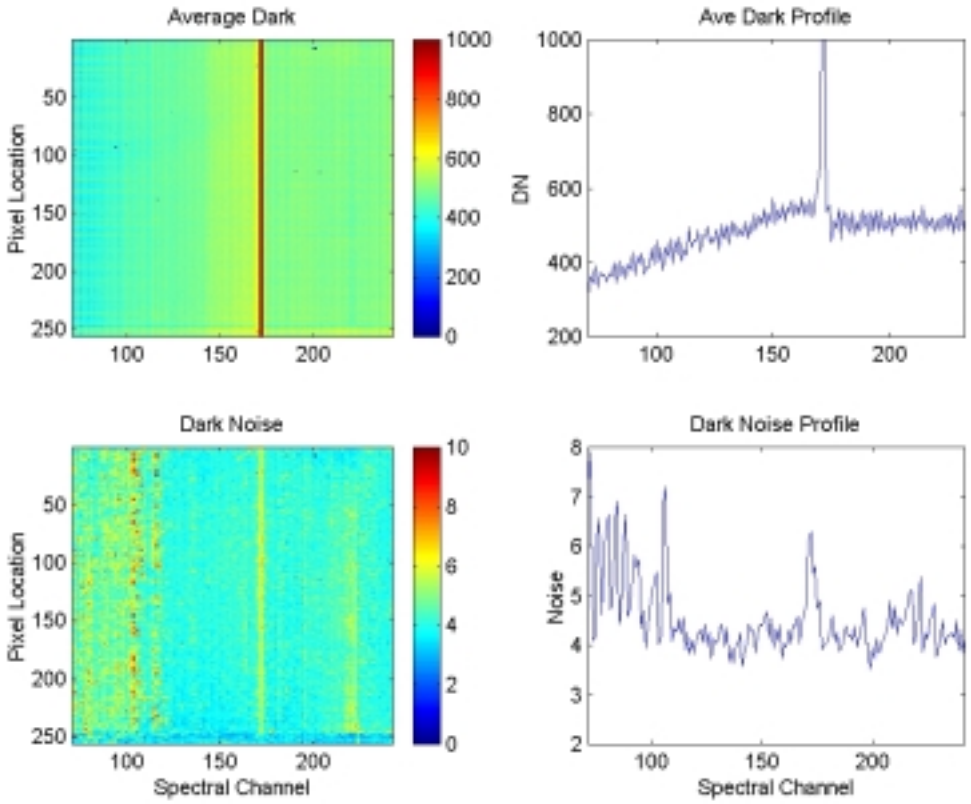

Figure 4.4.1-1 Example of SWIR average dark and temporal noise based on a dark data collect taken during a solar calibration event on day 2001- 047.

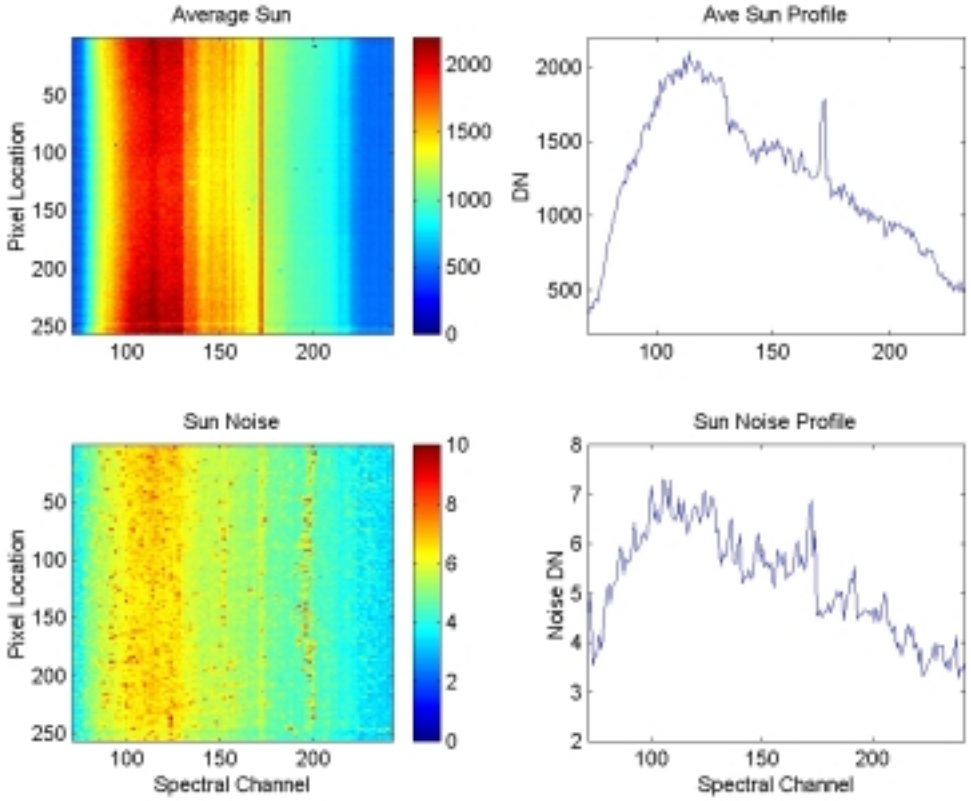

Figure 4.4.1-2 Example of SWIR average raw signal from a solar calibration event on day 2001-04 and temporal noise.

4.4.2 Quantization Noise

The data will have some induced noise simply due to the fact that the readout is only 12 bits so each electron does not have a corresponding digital value. For the SWIR it is by definition 0.5 DN.

4.4.3 Shot Noise

In addition to the readout noise, the primary source of noise in a CCD is the so-called "shot noise" which is simply due to Poisson statistics of the photo-generated electrons. In a theoretical sense it corresponds to the square root of the number of captured electrons, whether they were photo-generated or thermally generated in the form of dark current.

The data from the solar calibration were used to plot the noise as a function of signal level. The noise was taken from the raw solar data file and the signal was taken from the dark subtracted average solar data file. The data was segmented into four groups, representing each of the four channels for the SWIR. The results indicate that for the most part the measured noise as a function of signal level is independent of channel. The image data in Figure 4.4.1-2 suggests that certain regions of the focal plane may have a slightly different noise function. Figure 4.4.3-1 below contains the results.

Applying a linear fit to the data, the amount of noise for any signal level can be approximated. The requirements for SNR in the SWIR are listed in Table 4.4.3-1 below, along with the measured noise at the specified signal level in Table 4.4.3-2. The defined signal level is referenced to the radiance level one would expect for 30% albedo scene, 45-degree latitude north with 60 degrees solar zenith angle. The SWIR SNR meets or exceeds requirements. Differences between the pre-flight and on-orbit measurements could be attributed to the method used for the measurement. The responsivity varies across the focal plane. This was taken into account in the current analysis. The noise measurement using in this analysis is considered the single sample noise. The SWIR meets the requirements. The precision of the SWIR is discussed in section 5.5.

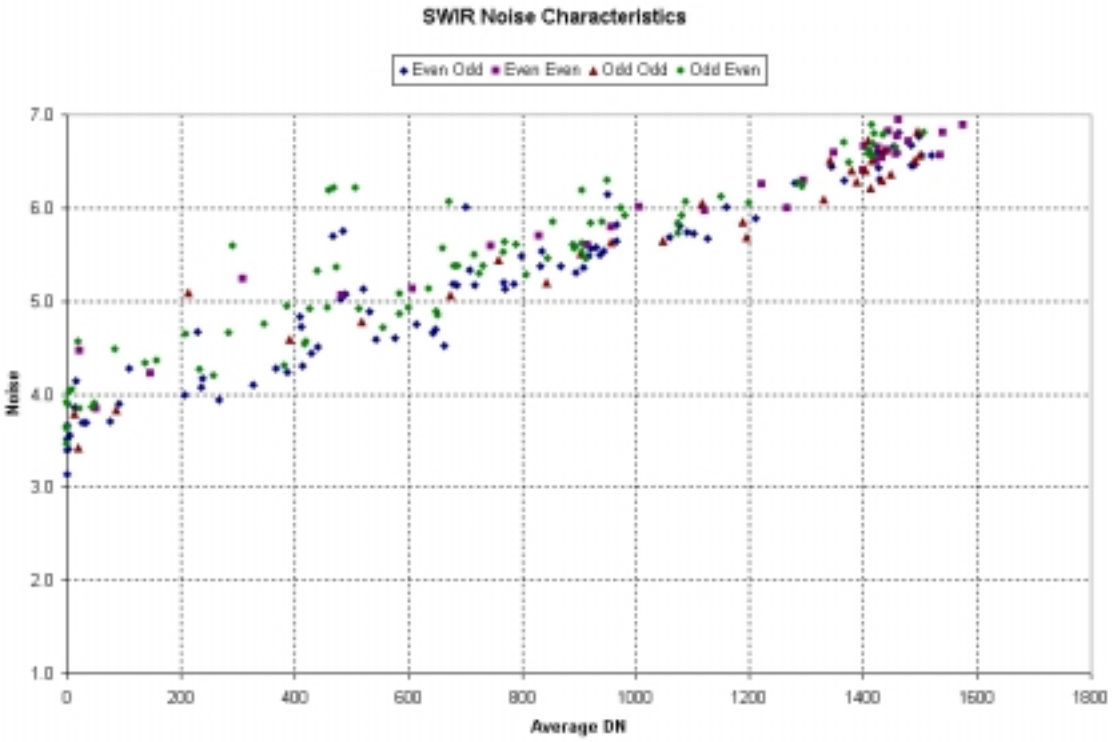

Figure 4.4.3-1 Signal versus Noise plot for each SWIR readout channel

Table 4.4.3-1 Signal To Noise Ratio Requirement

Wave-length	Defined Signal Level ($W/(m^2 \cdot sr.um)$)	Required SNR to Exceed	On-Orbit Measured Noise	Pre-flight Measured SNR
1025	30.8	60	65	90
1225	19.4	60	96	110
1575	10.6	60	64	89
2125	3.8	30	38	40

Table 4.4.3-2 Signal–to-Noise Ratio Support Data

Wave-length	Spectral Channel	Defined Signal Level ($W/(m^2 \cdot sr.um)$	Defined Signal Hyperion CNTS[1]	Measured Noise
1025	88	30.8	253.5	4.26
1225	108	19.4	406.7	4.59
1575	143	10.6	250.0	4.25
2125	197	3.8	140.7	3.98

[1] Based on Pre-Flight Measured Hyperion responsivity

4.5 SWIR Dynamic Range

4.5.1 Saturation

Direction was received from NASA/GSFC in 1999 to reset the gain on the Hyperion VNIR and SWIR focal planes so that they would saturate at 110% top-of-the-atmosphere solar radiance levels. It is easy to understand, therefore, that saturation is observed in very few scenes and to only a limited extent within these scenes. There are a few specific examples (see Figure 4.5.1-1) in which saturation occurs: cloud tops, hot spots within active volcanoes and artificial (man-made) flares such as the gas flares found at the Moomba oil fields in Australia.

The artifact correction routines for both SWIR spectral smear and SWIR echo are not designed to handle saturated data. Since the measured signal saturates in the digital domain first and the spectral smear happens in the analog domain, the data cannot be properly corrected. Due to these artifacts, the saturated pixel itself, the "next" read-out pixel, and the echo-affected pixel all contain invalid data.

Modifications are being made to the Level 1 processing for Hyperion in which saturated pixels and affected smear- and echo-corrected pixels are flagged as being invalid.

Saturation was observed to occur in the SWIR for man-made and natural hot spots such as the Erta-ale volcano in Ethiopia and the gas flare at the Moomba Oil and Gas Field in South Australia. Figure 4.5.1-1 shows the difficulty associated with saturation in the SWIR using an image of the Moomba gas flare. The image was taken at night to reduce the background around the flare. The Moomba data in this figure shows the large primary signal on the right side of both representations of the image. Because the flare image is saturated, the echo correction is incomplete and residual echo persists as demonstrated by the significant echo peak remaining on the left side of the image, Figure 4.5.1-2..

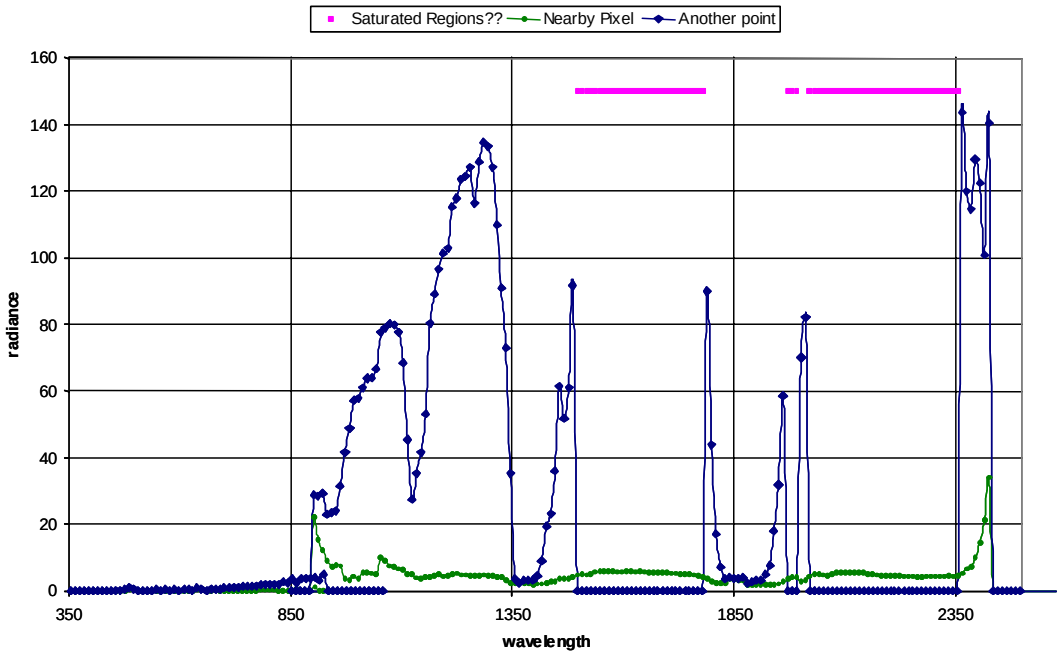

Figure 4.5.1-1 Example of Saturation

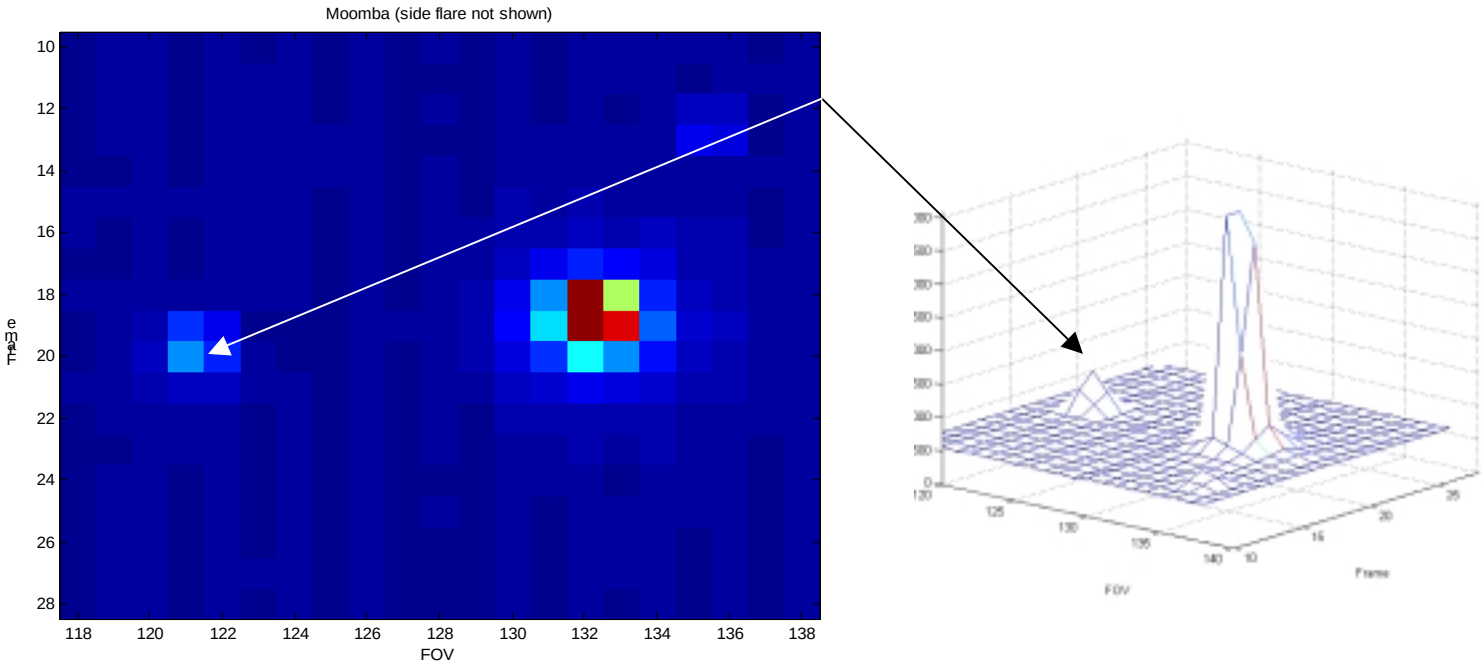

Figure 4.5.1-2 Echo removal based on saturated SWIR pixels is inaccurate and leaves a residual echo. The flare is the large peak on the right of both images while the smaller peak on the left is what remains after correction of the echo located there.

4.5.2 Linearity

Although there is no formal requirement on the linearity of the instrument, there is a flow-down requirement on the linearity in order to meet the 6% radiometric accuracy over the dynamic range of the sensor. The flow-down requirement stems from the sensor being calibrated at only one radiance level and the application of this calibration to the entire dynamic range of the instrument.

The linearity of both the VNIR and SWIR were determined to be linear based on ground tests. Linearity on the order of 1% is required to meet the radiometric requirements. Linearity has not been measured on-orbit.

4.6 SWIR Repeatability

4.6.1 SWIR DCE-to-DCE Repeatability

The data set collected as part of the calibration lamp trending was used to assess the repeatability of the VNIR and SWIR. Section 3.6.1 describes the analysis. Table 4.6.1-1 presents the results for the SWIR. The SWIR the repeatability is taken to be 1.6 %.

Table 4.6.1-1 SWIR Repeatability

SWIR	Repeatability
Band 100	1.42
Band 150	1.15
Band 200	1.51

4.6.2 SWIR Pixel-to-Pixel Repeatability

The solar calibration data collects have the unique advantage of providing a collect that is by definition, uniform across the field of view. A set of solar calibration collects were analyzed and compared with each other to determine how much the pixel response varied across the field of view. There are two types of variation. One in which one could consider the average focal plane response, and another in which the focus is the pixel to pixel variation in the response. The later is the focus in this section. The solar calibrations obtained on Day 047, 051, 054, 057, 061 and 068 were used. The on-orbit calibration file was adjusted in the field-of-view direction using Day 047. Hence for this analysis the average of each solar calibration event was compared with the one obtained on Day 047.

The ratio of each solar cal to the Day 047 solar cal was obtained. The standard deviation of the ratio across the field of view was calculated for each band. This was used as a measure for the pixel-to-pixel variation. For the SWIR the pixel-to-pixel variation was approximately 0.75 %.

4.7 SWIR Pixel Status

4.7.1 SWIR Outlier Pixels

The pre-flight calibration and the on-orbit calibration based on the update of the pre-flight calibration using Day 047 solar calibration were compared. The comparison was used to identify pixels whose response changed more than the surrounding pixels and to identify dead pixels.

The following steps were taken to identify outlier pixels:

1. Ratio of the on-orbit to pre-flight calibration calculated. See figure 4.7.1-1.

2. Characterize each region, calculate the mean and standard deviation of the ratio for each field of view location

3. Identify pixels whose calibration changed by more than 3 times the standard deviation of the rest of the field of view location.

The results are listed in the Table 4.7.1-1. No new dead pixels were identified. Pixels listed on Table 4.7.1-1 should be monitored to determine whether they can be reliably used or if they should be removed from the Level 1 data product.

Table 4.7.1-1 does not include the region near the edge of the field of view that behaves differently from the entire focal plane and will be looked at in more detail. This region appears to be the same region affected by edge echo, see figure 4.7.1-2.

Table 4.7.1-1

Field of View Position	Spectral Channel	Percent Different
1	225	28.9%
2	225	36.7%
8	81	5.7%
98	222	41.1%
159	92	11.1%

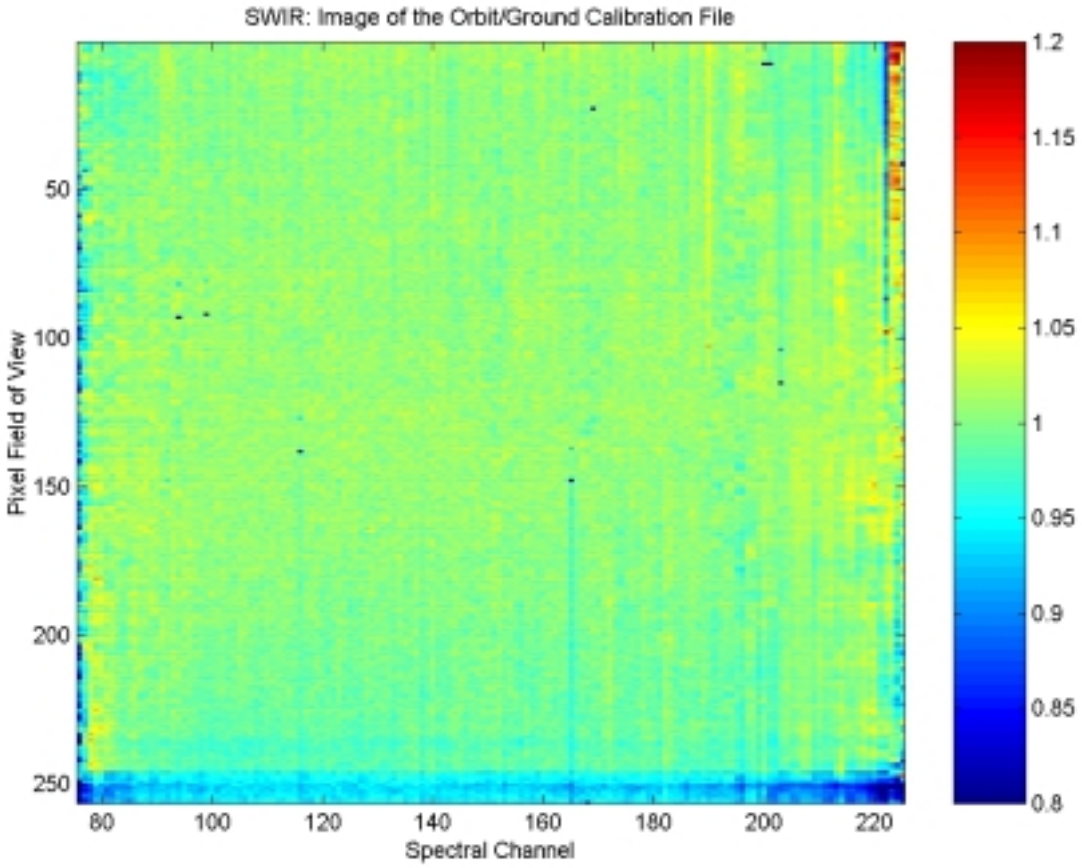

Figure 4.7.1-1

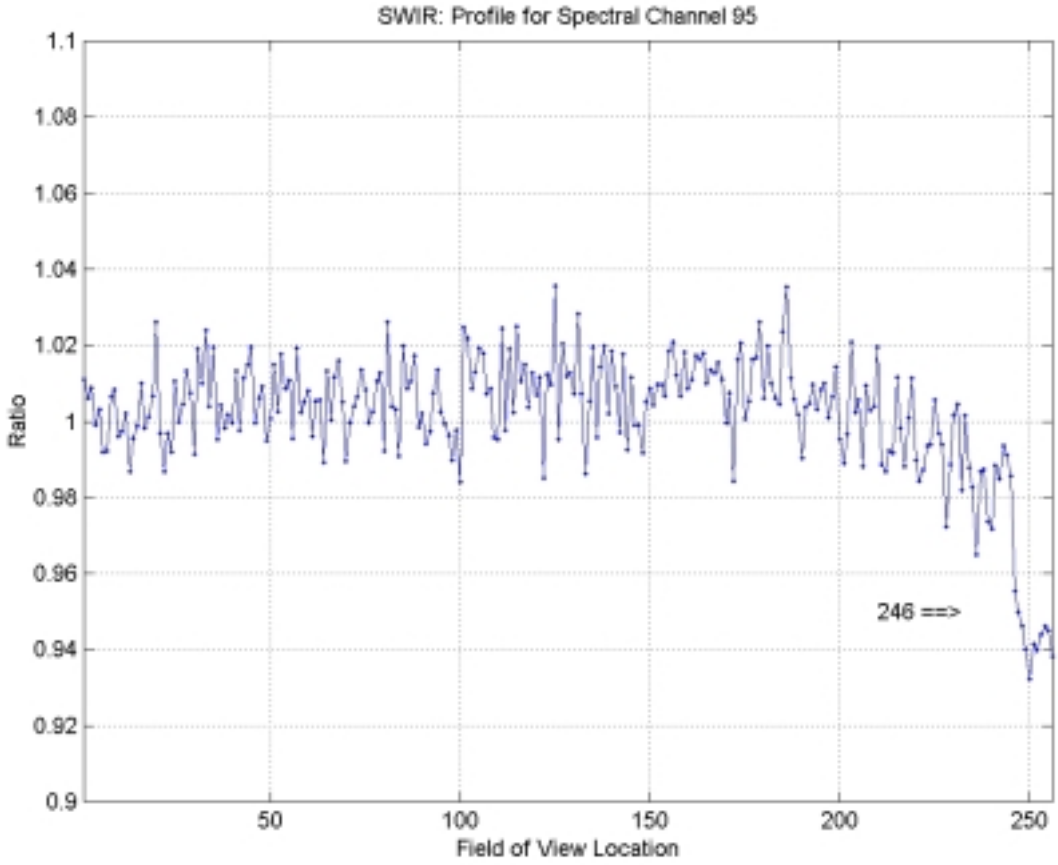

Figure 4.7.1-2

4.7.2 SWIR Sensitivity to the South Atlantic Anomaly

The SWIR is impacted by the SAA in the same manner as the VNIR detector, refer to section 3.7.2.

4.8 SWIR Summary

The SWIR focal plane was discussed in detail. The process of dark removal and the evaluation of the SWIR drift were reviewed. Level 1 processing reduces this effect to negligible levels. To the degree the correction algorithms could be verified, the SWIR Echo algorithm appears to be applicable for on-orbit operations with the investigation spurring a revisit to the original correction file developed on the ground. The SWIR was found to be sensitive to the South Atlantic Anomaly.

The noise in the SWIR was evaluated using the solar calibration event and meets the specification. The SWIR was studied for outlier pixels, and several pixels were identified for monitoring. The trending of the lamp was used to assess the repeatability of the focal plane.

The influence of each of the topics discussed in this chapter was assessed. In section 5.5 the terms are combined to create an overall precision error. The SWIR Precision error is 2.2 % and

is a combination of repeatability, calibration drift, residual artifact and residual dark field removal errors.

5 ABSOLUTE CALIBRATION AND ACCURACY

5.1 Pre-Flight Calibration

The pre-flight calibration process has been described by Jarecke [1] and some of the material has been abstracted as an overview for this section.

5.1.1 Primary Standard

The source of radiant power for realizing an irradiance scale at TRW is the Sylvania FEL 1000 watt Quartz Tungsten Halogen (QTH) lamp. Four lamps were purchased from Optronics Inc. Two of the four lamps were calibrated by Optronics Laboratories, Inc. relative to the same type of lamp, which Optronics procured from the National Institute of Standards and Technology (NIST). The calibration of the lamp from NIST is calibrated by a procedure defined in the NIST special publication, Standard Irradiance Calibrations No.250-20 Sept. 1987 [2].

An independent cross-calibration all four lamps was made using three detector based irradiance standards each fitted with a different precision entrance aperture. Two of the standards are based on the high quantum efficiency (HQE) photodiode trap detector. For a discussion of the solid state physics tractability and the validation of the standards see [3], [4] and [5]. The two independent HQE trap detectors are a UDT (Graseby) QED-150 that uses three EG&G UV444B Silicon detectors and an SPR-73, which is supplied by Cambridge Instrumentation and Research, Inc (CRI). The SPR-73 uses three windowless Hamamatsu S1337-1010 detectors. The third primary detector standard is the LaserProbe Inc. RS-5900 SN 9409-035 electrically calibrated pyroelectric radiometer (ECPR). This absolute self-calibration technology was developed by Doyle, McIntosh (Laser Precision Corp) and Geist (NIST) [6].

An HQE trap Silicon photodiode primary standard detector using Hamamatsu photodiodes has been cross-calibrated with a helium cooled active cavity radiometer primary standard at CRI and agreement of 0.02 % was achieved [7]. While the systematic error of the ECPR, estimated at about 1% (Ref 5), is much greater than the Silicon trap detector error, it serves two purposes for the Hyperion calibration. First, it is a crosscheck to rule out large errors in the use of the HQE trap detector out to the 0.9 micron cutoff of the silicon. Secondly, it extends the lamp calibration out to the 2.5 micron cutoff of the Hyperion HgCdTe SWIR focal plane array.

The source of irradiance for the scale is the FEL 1000 watt lamp. Comparisons of the three primary standards are made to realize an irradiance scale for Hyperion. First, the two trap detectors' spectral responsivity is compared using a HeNe laser line source that under filled each entrance aperture (so the comparison was in radiant power). The signal is varied using a polarizer over the dynamic range from 1 to 60 microwatts and the agreement is 0.080 % ± 0.033 % 1σ using linear regression over 12 signal levels. When the same comparison is made between the QED-150 and the LaserProbe ECPR an agreement in response to the HeNe laser line source of 0.34 % ± 0.014 % is obtained from the linear regression.

Spectral irradiance levels as a function of wavelength are measured using a set of narrow bandpass filters whose transmission characteristics have been measured with a CARY 50E spectrometer calibrated with NIST transmission standards. The linearity of the spectrometer was verified. A linear regression of the responses between the QED-150 and the LaserProbe ECPR to the lamp irradiance in 9 of the spectral bands produced an agreement in relative response of 0.68

% ± 0.88 % 1 σ. The dynamic range for the regression is set by the change in lamp irradiance from 0.4 to 0.9 microns in the narrow bands. A second linear regression of the responses of the QED-150 and SPR-73 in 8 of the bands (one was being replaced at the time) produced an agreement in response of 0.34 % ± 0.76 %.

Using the absolute irradiance measurements of the lamp in 10 wavebands from 0.4 to 0.9 microns and measurements made with the ECPR in another 19 wavebands from 1.0 to 2.5 microns, an absolute spectral irradiance curve for the lamp is generated. The curve fit through the points is a graybody with temperature of 3100 Kelvins and an emittance, which is smoothly, and monotonically decreasing by 35 % over the wavelength range. The RMS variation of the points about the curve fit is 0.97 % if four of the bands are not included. These four bands were high by > 3 σ which may have been due to residual, uncorrected out-of-band response. Spectral irradiance for all bands is plotted in Figure 5.1.1-1. The Optronics calibration delivered with the lamps is shown as gray circles. The deviation between the Optronics calibration and the TRW measurement is shown in Figure 5.1.1-2.

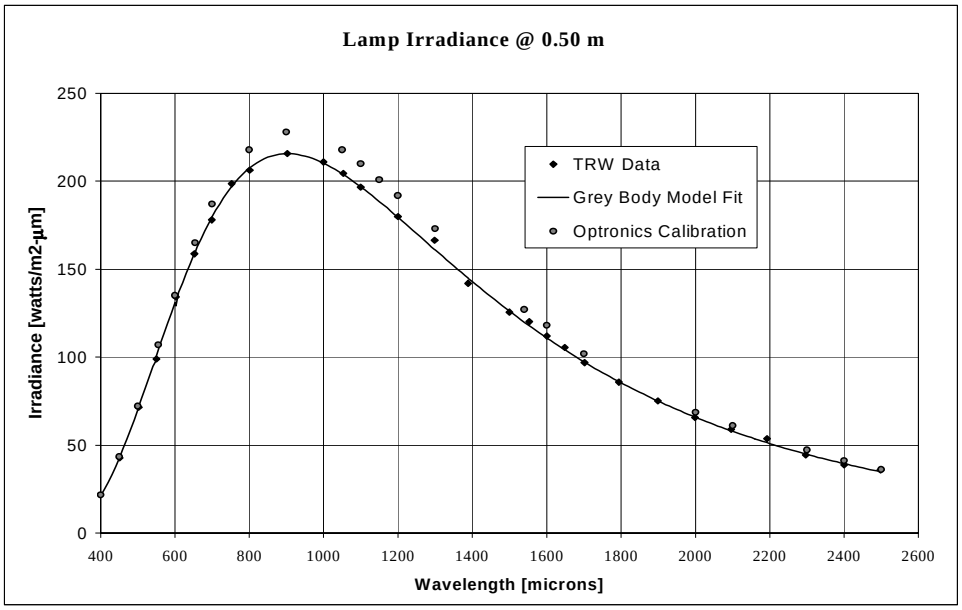

Figure 5.1.1-1. Spectral Irradiance of the FEL Lamp (SN 543) Measured With the Primary Standard Detectors filtered with the Narrow Band Filters.

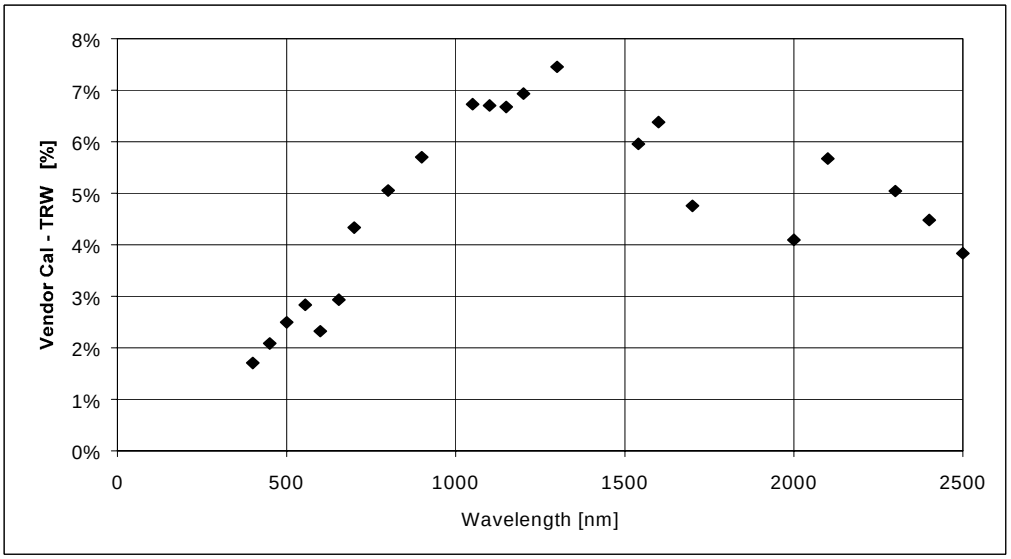

Figure 5.1.1-2. The vendor lamp calibration values are from 2 % to 7 % higher that the TRW Silicon Photodiode Primary Standard.

5.1.2 The Secondary Radiance Standard Source

To create a secondary standard source of radiance, an assembly is used to hold the FEL lamp at a distance from a square Spectralon plate. The lamp illuminates the plate at a normal angle and the assembly is mounted on the door of the vacuum chamber used for radiometric

calibration of the sensor. The sensor views the plate from inside the chamber through an uncoated SiO_2 window. A wall in the assembly prevents direct view of the window by the lamp.

A Spectralon panel was expressly chosen over an integrating sphere. The reason is that the integrating sphere cannot be modeled accurately enough for a calculation of the exit aperture radiance. A Spectralon panel can and this permits a critical opportunity for a cross check for systematic errors.

To first order, the radiance from the Spectralon plane is the incident lamp irradiance divided by π if the BRDF of the panel is perfectly Lambertian. It is critical to know the BRDF and reflectance of the plate over the angles and spatial extent viewed by the sensor. Reflectance properties of the Spectralon plate are taken from vendor specifications and measurements made at TRW with the Optical Scatter and Contamination Effects Facility. The BRDF angle of scatter of the lamp irradiance to the sensor varies from 19 degrees to 33 degrees.

5.1.3 Use of the Transfer Radiometer for Cross-Calibration of the Calibration Panel Assembly (CPA) Panel

As a cross-check of the assumed properties of the Spectralon used to convert irradiance to radiance, a transfer radiometer is employed which uses an off-axis parabola mirror and a fold mirror with a precision entrance aperture and the SPF-73 trap detector. A 0.7 to 0.9 micron band pass filter limits the spectral range. The increased spectral bandwidth is necessary to allow adequate signal at the reduced values produced by the radiance from the Spectralon plate. This radiometer is placed in the CPA at about 0.5 meters from the plate in a position to view the plate along the same line of sight as the Hyperion sensor.

Data are taken with the transfer radiometer in three configurations: 1) with the lamp and plate alone without any assembly structure in place; 2) with the CPA fully assembled; and 3) with the CPA mounted on the vacuum chamber wall. The expected signal from the trap detector in the transfer radiometer is calculated, in advance, using the measured lamp irradiance, the reflectance properties of the Spectralon and the throughput of the transfer radiometer. The throughput is determined from the $A\Omega$ of the transfer radiometer, which is calculated from precision measurements of the aperture areas and the focal length of the off-axis parabola (OAP) in the radiometer. The transmittance of the 0.7 to 0.9 μm band pass and the reflectances of the protected silver coated OAP mirror and fold mirror are included in the calculation. This calculated value is compared in Table 2 below with four measurements taken in the three configurations listed above.

The radiance from the CPA, which is mounted on the chamber wall, is used to absolutely calibrate the Hyperion sensor. This radiance is corrected for the $\cos^4$ profile described above and the transmittance of the uncoated SiO_2 vacuum chamber window. The vacuum chamber wall on which the CPA is mounted is painted white. A black painted sheet of aluminum is hung on the wall to reduce the light from the lamp that is scattered back to the SPA panel. Measurements of this scatter radiance from the black sheet were made with the ASD Field Spec spectral radiometer. Illumination from this source produces less than 0.1 % increase in radiance of that from direct illumination by the lamp. The SiO_2 window also reflects back to the panel with a reflectance of about 4 % per surface. A calculation of the expected return to the CPA panel from

this source is also about 0.1 %. This reduction is produced radiometrically by the ratio of the apparent solid angle of the panel (as it views its own reflection) to the solid angle, π, into which the 8 % contribution is re-scattered.

Table 5.1.4-1. Agreement between Measured and Calculated Transfer Radiometer Radiance Values for the CPA.

Date	Configuration	Lamp Age [Hours]	Expected Signal [μA]	Measured Signal [μA]	Relative Difference [%]
5/6/99	Panel on open bench	25.4	0.3487	0.3502	0.41
5/6/99	Panel mounted in assembly on bench	30.1	0.3487	0.3527	1.13
6/8/99	Panel assembly mounted on Vacuum chamber	39.4	0.3487	0.3505	0.51
7/2/99	Panel assembly mounted on Vacuum chamber	68.6	0.3487	0.3509	0.61

5.1.4 Pre-flight Absolute Calibration Error Estimates

The results in Table 5.1.4-1 suggest that the radiance scale produced by calculating the expected conversion from irradiance of the lamp at the Spectralon plate to radiance using the assumed properties of reflectance and scatter characteristics the plate is consistent with the optical throughput of the transfer radiometer at about the 0.8 % difference level (RMS of Table 5.1.4-1 results). To determine the expected agreement between these two radiance determinations, an error estimate for the two conversion processes described in sections 5.1.2 and 5.1.3 is made based on the steps in the processes and presented in Table 5.1.4-2a and 5.1.4-2b. All error estimates in the tables are 1 σ and combined by RSS.

It would appear that the predicted errors in comparison of the two conversions of the irradiance on the CPA to radiance are larger than the measurements in Table 5.1.4-1. Perhaps two of the larger error terms were in the same direction and cancelled out. We conclude from the results in Table 5.1.4-2a and 5.1.4-2b that the conversion has a probable error on the order of 1% using both methods as a self-consistency check. Table 5.1.4-3 shows the error estimates for the lamp irradiance measurement the entire CPA radiance source error. Note that the same detector is used for both the lamp irradiance measurements and the transfer radiometer so that detector response error cancels out.

A primary irradiance scale is realized at TRW with agreement between absolute detector standards better that 1 %. This scale is used to create a secondary radiance scale using a Spectralon Panel. The predicted radiance accuracy of than 2 % is based on the agreement between the cross comparison of two different ways of determining the irradiance to radiance conversion. One comparison use validated relative BRDF properties of Spectralon and vendor

data for absolute reflectance. The other use a transfer radiometer with an independently determined AΩ. This Spectralon panel radiance source is used to calibrate the Hyperion sensor.

Table 5.1.4-2a. Conversion from Irradiance to Radiance Using Spectralon Scatter Properties

Error Term	Error [%]
Reflectance at 26° Angle of Incidence	1.0
Scatter Uniformity with Angle	0.5
Stray Light	0.2
Total Error	1.35

Table 5.1.4-2b. Direct Measurement of Radiance with Calculation of AΩ for the Transfer Radiometer

Error Term	Error [%]
Entrance Aperture Area	0.5
Field Stop Area	0.2
OAP Focal Length	0.4
AΩ Calculation	0.3
Total Error	0.73

Table 5.1.4-3 Error Estimates for Lamp Spectral Irradiance Which is Given as a Sub-total and Total CPA Radiance Below. Errors are 1 σ RMS.

Lamp Irradiance		**Error [%]**
Primary Standards		0.29
Agreement	0.1	
Trap Detector Ammeter Calibration	0.3	
HQE Correction	0.1	
Lamp-Trap Detector Distance		0.5
Precision Aperture Area		0.5
Filament Alignment Repeatability		0.3
Lamp Current Repeatability		0.1
Filter Effective Bandwidth		1.0
Interpolation Between Band Data Points		0.5
Total Lamp Irradiance (Subtotal)		**1.39**
Conversion to Radiance		1.0
Stray Light Contamination		0.5
SiO_2 Window Transmittance		0.5
Total Error		1.85

The error estimations in Tables 5.1.4-1, 5.1.4-2a, 5.1.4-2b and 5.1.4-3 are limited to coverage of calibration of the instrument on the ground. They do not cover the errors in transfer of the calibration from the instrument to the internal calibration subsystem. This is discussed in the next section.

5.1.5 Calibration Transfer to the In-Flight Calibration Source (IFCS)

5.1.5.1 Pre-flight Test Results

The IFCS uses four quartz tungsten halogen (QTH) lamps (1.06 Amp, 4.25 Volt) to illuminate the back of the telescope cover in the closed position. The cover, located at the aperture stop of the telescope, is painted with a diffuse, reflecting, white, silicone, thermal control paint. The lamps are powered in two pairs making a primary and a secondary set (IFCS 1 and IFCS 2). Two lamps per set are required to achieve an adequate level of illumination.

The transfer was made during ground data processing by taking a sequence of collects including a dark field (measured with the cover closed) another dark field, a primary internal source (IFCS 1) measurement, a measurement of primary plus secondary, a measurement of IFCS 2 and a final dark field. From these data, the radiance from the IFCS diffuse panel cover was derived.

The purpose of the internal calibration lamps was to be used as a constant source of radiance that could be used to update the instrument calibration on-orbit. During pre-flight tests, a set of six IFCS lamps were cycled 2500 times using the flight duty cycle. The current and voltage drop across the string of six bulbs was monitored continuously while the radiant output of a single bulb in the set was measured. No significant degradation in the lamp performance was observed. However, it was noticed prior to and then verified during thermal vacuum testing on the EO-1 spacecraft at Goddard in April, 2000 that the output from the primary lamp was varying.

Upon investigation, it was found that the calibration lamps had not undergone a burn-in process. As a result, burn-in runs were performed while the spacecraft was at Vandenburg AirForce Base just prior to launch. The testing took place on September 1, 2000. The Hyperion calibration lamps were operated for 5 hours to stabilize the radiometric output. During this test the primary lamp burned out. Figure 5.1.5.1-1 graph shows the demise of the primary lamp and the history of the secondary lamp since the baseline was performed on July 1, 1999. The second graph shows the stabilization of the secondary calibration lamp that was achieved during the burn-in process. The cause of the lamp fluctuation during burn-in was investigated to determine if there was any correlation with lamp voltage and various VNIR temperatures. No significant correlation has been determined with any of these parameters.

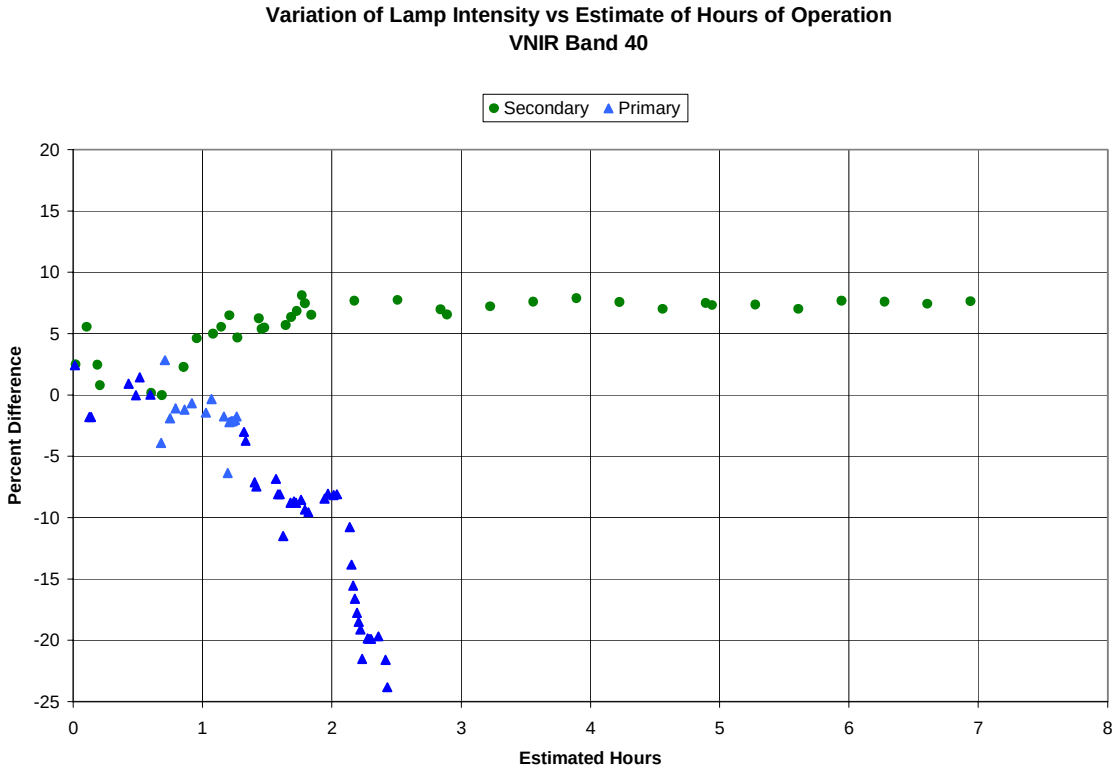

Figure 5.1.5.1-1 History of the In-Flight Calibration Sources Before Flight

Prior to launch fifteen lamps, from the same lot as the flight lamps, were selected for a life test. The testing was performed at Goddard Space Flight Center under their direction. Each lamp was powered individually with its own solar cell detector, mounting fixture, and constant current power supply. The lamps were operated continuously at a constant current of 0.98A. Relative radiant output was monitored along with the voltage across the lamp terminals and current through the bulb filament. The lamps were operated for 50 hours. At this point the lamp output had decreased by 1 to 6 %. Six lamps, subset from the fifteen lamp set, which spanned the range of stability exhibited at 50 hours of operation were selected to be operated beyond the expected 146 hr lifetime of the Hyperion instrument. These six lamps were operated for a total of 218 hours with no failures. After 150 hours of operation, the light output decreased by 4 to 10 % with one bulb decreasing by 17 %. This behavior is consistent with the on-orbit trending of the secondary calibration lamp output as discussed in Section 5.2.2.

5.2 On-Orbit Calibration

5.2.1 In-Flight Calibration Source Performance.

Shortly after launch, an internal calibration data collect was performed. The intensity of the lamp on-orbit appeared to have increased significantly from pre-flight levels. Figure 5.2.1-1 compares the dark subtracted signal of the instrument in response to the calibration lamp. The data presented in this figure is from the second internal calibration data collect since it is the first

collect with the SWIR was at operational temperature. Both the VNIR and SWIR indicated that the intensity of the lamp had increased. For reference, the increase at band 40 was 30%. Figure 5.2.1-1 compares the on-orbit result with a sample taken during the second EO-1 Thermal Vacuum Test at Goddard (summer-2001) and with the reference taken at TRW during the absolute calibration tests (summer-1999). It is hypothesized that the temperature of the filament was operating at a higher temperature because the lack of gravity on-orbit. The lack of gravity limits the onset of convection cooling resulting in a higher filament temperature. The increase in lamp operating voltage supports this hypothesis, refer to Part 1 of this document. The spectral variation of the lamp output was used to further investigate this hypothesis.

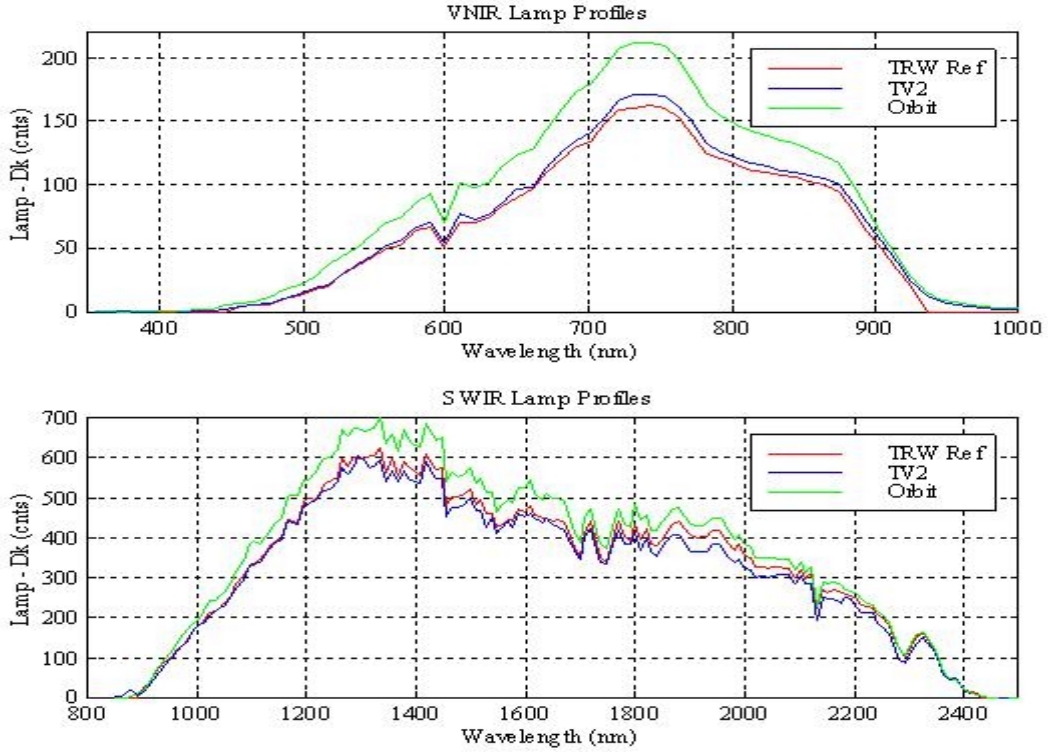

Figure 5.2.1-1 Internal Calibration Data Collects show the VNIR and SWIR response increased significantly from ground measurements.

Figure 5.2.1-2 presents the theoretical black body profile for three different temperatures. The bottom plot demonstrates that changes in the black body temperature can be detected by comparing the ratio of two profiles. This was essentially the method used to determine what type of temperature change could correspond to the type of change detected by the instrument. The approach was to generate theoretical black body profiles for a range of temperatures in the vicinity (+/- 250K) of the expected filament operating temperature (3000K). Then the ratio of two selected temperature profiles were compared with the ratio of the instrument measurement on-orbit to on-ground.

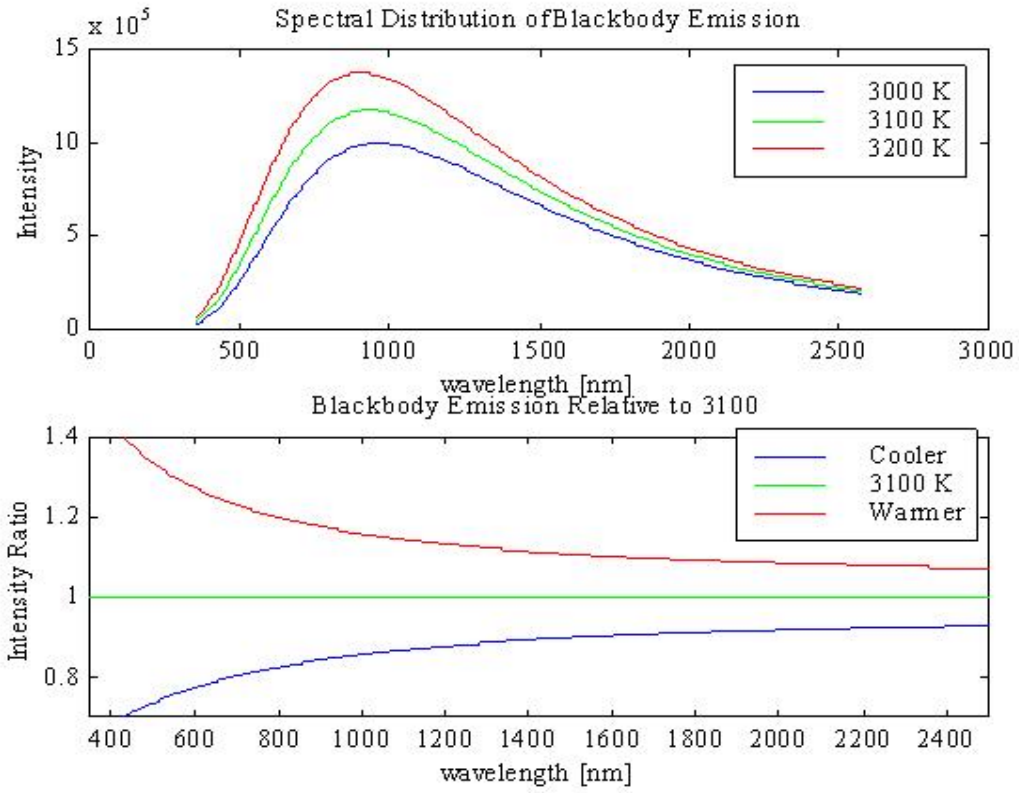

Figure 5.2.1-2 Example of theoretical Black Body profiles and the variation in the ratio of profiles of different temperatures.

Figure 5.2.1-3 is a comparison between the lamp on-orbit to ground ratio with the theoretical ratios of the blackbody curves at different temperatures, and using on-orbit data for two different days (2000, Day 332 and Day 343). The ratio is dependent on the assumed temperature on the ground, and the simulated increase in temperature for the on-orbit case. The ratio is not a unique value. Figure 5.2.1-3 shows that there is a range of initial temperatures and correspondingly different temperature deltas, which result in a ratio profile that closely matches the ratio of the VNIR data. Figure 5.2.1-3 also displays the ratio of the SWIR on-orbit to ground data. The SWIR ratio does not match as well as would be desired. The analysis assumes that the filament emission follows a black body profile. One possible source of discrepancy, therefore, is that the emittance of the filament rises with temperature faster in the SWIR than in the VNIR.

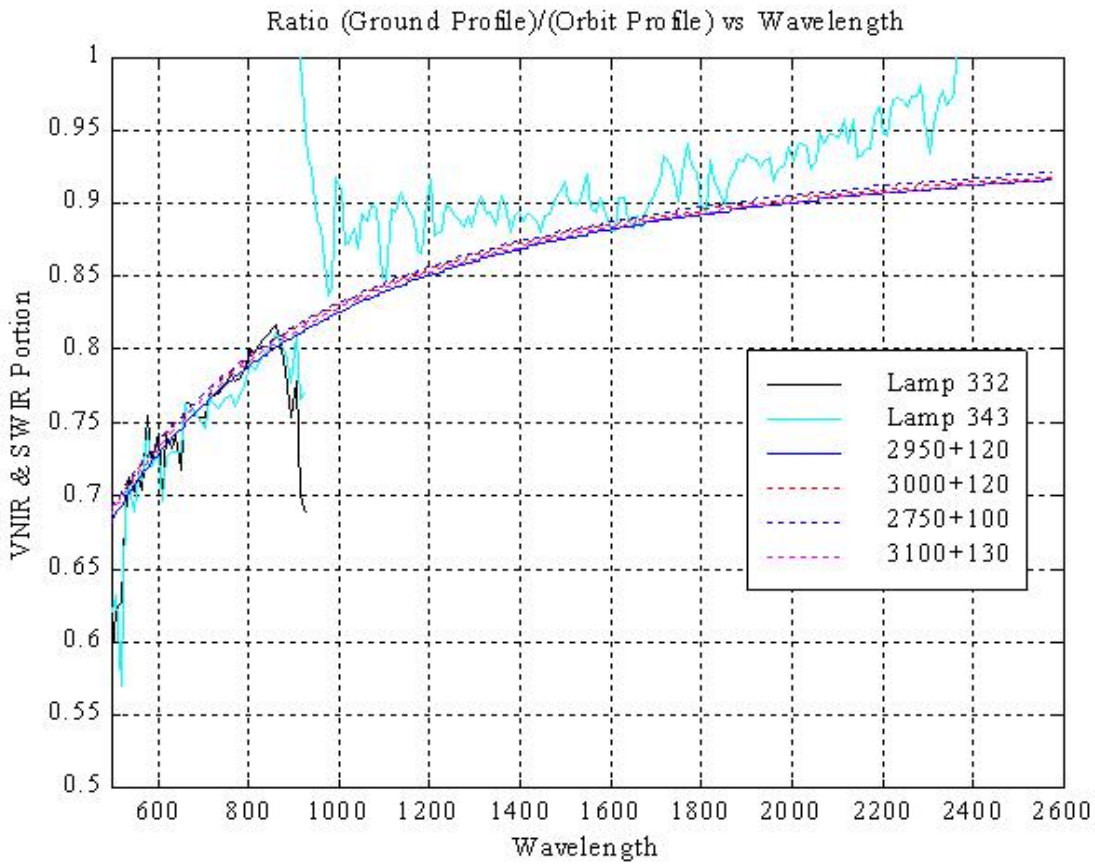

Figure 5.2.1-3 Trend of the assumed ground temperature and corresponding increase in filament temperature which approximates VNIR detected on-orbit to ground ratio.

Figure 5.2.1-4 is a linear plot of the assumed ground temperature and corresponding increase in filament temperature which approximates VNIR detected on-orbit to ground ratio. The results indicate that for an assumed filament temperature of 2900 K the increased radiance detected by the VNIR is consistent with an increase of temperature on the order of 100-130 K. This rise in temperature is reasonable and expected (private communication with Henning Leidecker (GSFC)). A detailed analysis requires knowledge of the gas pressure and composition inside of the bulb and was beyond the scope of this analysis. It should also be noted that the increase in operating temperature is consistent with the increase in voltage (associated with an increase in resistance) across the filament.

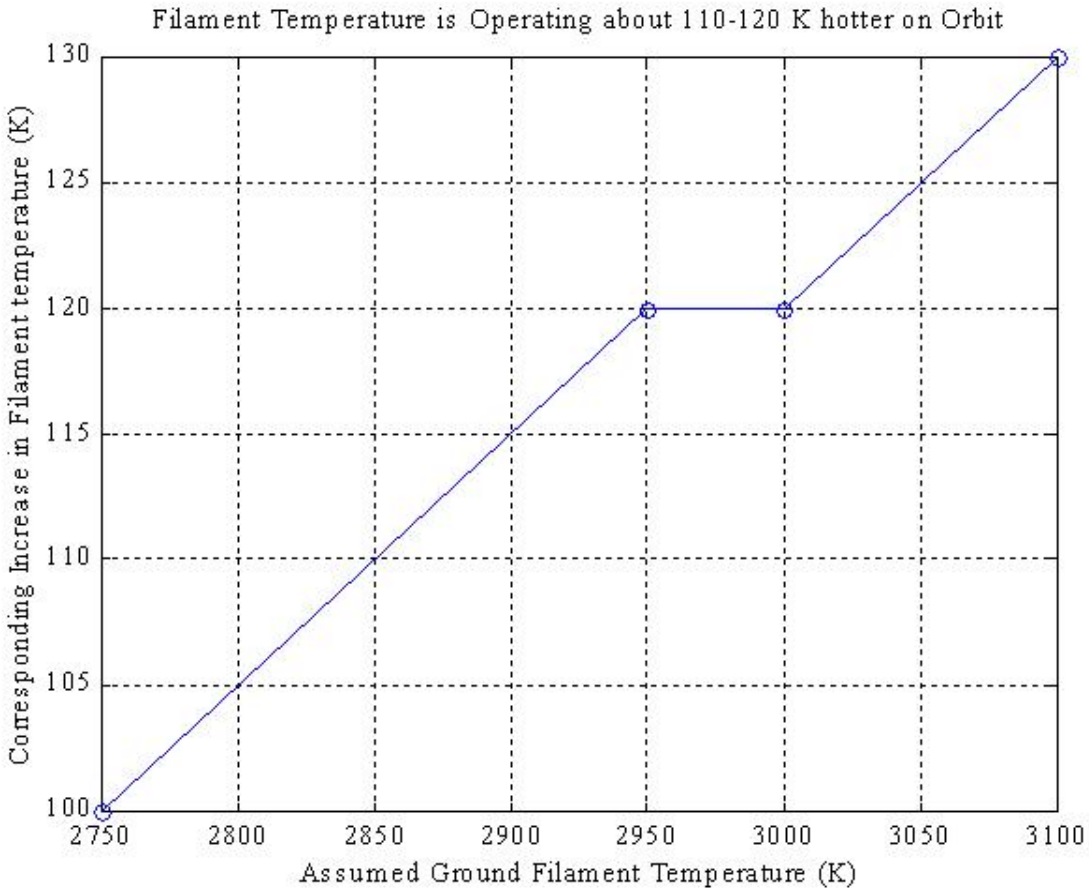

Figure 5.2.1-4 The results support a 100K – 130K increase in filament temperature assuming an ground filament temperature around 2900K.

5.2.2 On-Orbit Trending of the Calibration Lamp

A lamp data collect is obtained during each DCE. The lamp output has been trended for each DCE that was processed during the performance verification process. Figure 5.2.2-1 shows the average across the field of view (from pixel 50 to pixel 200) for one band in the VNIR and one band in the SWIR that have been used for trending. The data is presented as percent difference from a reference lamp chosen as the one taken during the Day 347 solar calibration. The data is presented as a function of minutes of operation, where there is 3 minutes of on time for each DCE obtained. The results indicate that after the initial increase in output, the lamp intensity continues to decrease. Based on this trend a request was made to modify Level 1 processing so that no adjustment in the calibration coefficients was made based on the lamp intensity. The plot also clearly indicates DCEs in which the SWIR was not at the operational temperature. Therefore, the lamp collect is still a part of the DCE sequence and can be used for trending and verifying the SWIR operational temperature. However the SWIR FPE temperature provided as part of the Hyperion normal telemetry should also be monitored. The trending database of the

lamp was also used to assess the VNIR and SWIR DCE-to-DCE repeatability as described in chapters 3 and 4.

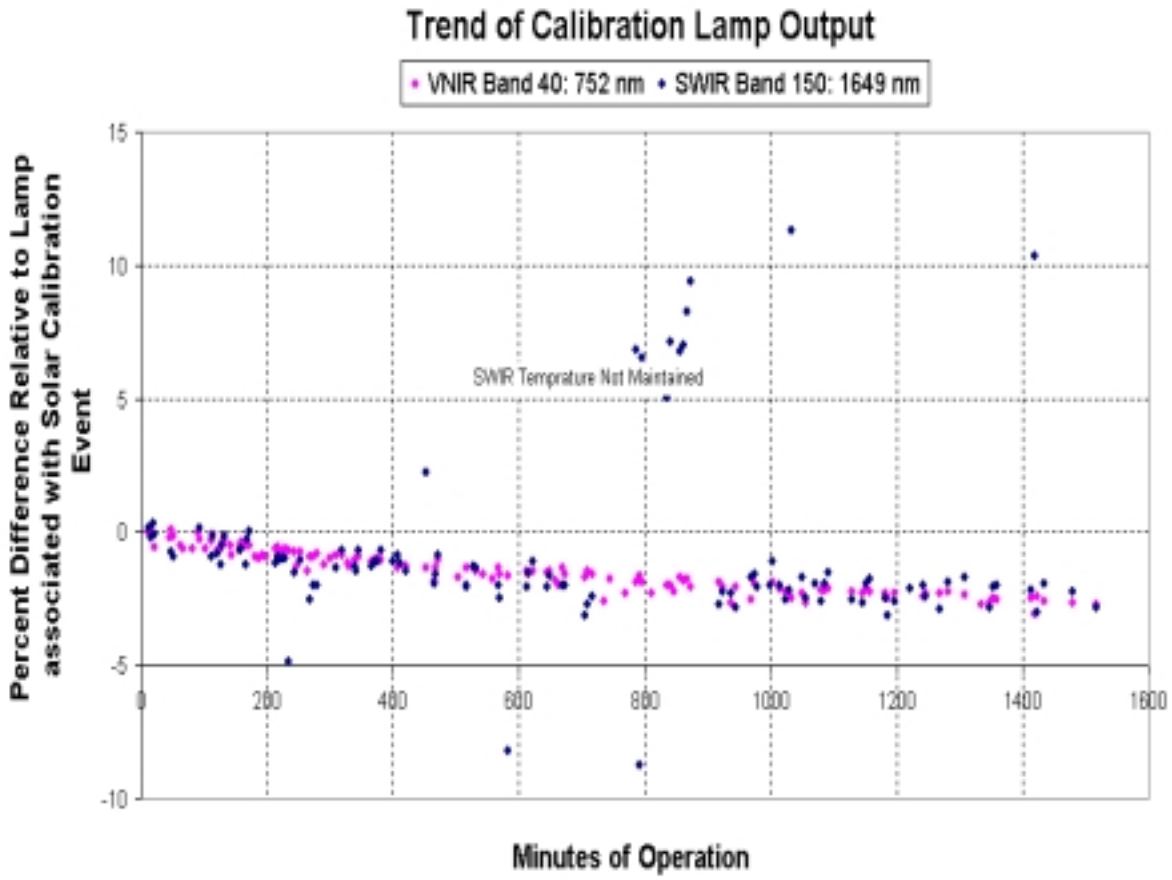

Figure 5.2.2-1. The average across the field of view (from pixel 50 to pixel 200) for one band in the VNIR and one band in the SWIR that have been used for trending. The lamp intensity continues to decrease in a manner consistent with the long-term life testing of lamps described in 5.1.5.1.

5.2.3 Error Estimation for the In-Flight Calibration System

The IFCS has demonstrated a large change in output from ground to on-orbit. Analysis indicates that the change is consistent with an increase in filament temperature. It is very unlikely that the VNIR focal plane would have changed in response as a function of wavelength. Furthermore, the SWIR would have to change in a prescribed way as well. The conclusion for this error estimate is that the lamp change was real and the focal plane responses did not change and the possible change in responsivity is less than ± 3 % in the VNIR and ± 5-8 % in the SWIR.

5.3 Solar Calibration

5.3.1 Definition of the Data Collection Event (DCE)

A Hyperion solar calibration event follows a procedure similar to that of a standard image DCE. Once the spacecraft has been maneuvered into position to view the sun, the sequence begins with a 1 second, 224 frame dark collect. The Hyperion cover is then opened to the 37 degree position to view the sun's reflectance off of the white paint on the cover. This is immediately followed by a 10 second, 2234 frame image collect after which the cover is closed. The sequence continues with a second dark collect followed by a 3 second, 670 frame lamp collect. Finally, the sequence is finished with a third dark collect. The solar angle of incidence is 53 degrees and the scatter angle of the diffusely reflected radiance is - 16 degrees (i.e. it lies between the incident ray and the specular ray).

5.3.1.1 Solar Irradiance Model

Three spectral solar irradiance models were used for the cross-comparison. One is the spectral solar irradiance data that was published in the World Climate Research Programme by C. Wehrli [8]. It was a compilation of data from H.Neckel, D.Labs in the VNIR and E.V.P.Smith, D.M.Gottlieb in the SWIR. The second was by G. Thuillier [9] and the third was by R. Kurcuz [10]. These spectral radiance curves are normalized by equating the total spectral integral over wavelength to the solar constant as defined by the World Radiance Reference which is absolutely accurate to better than 1 % by using irradiance scales established by active cavity radiometers operating in ambient conditions.

5.3.1.2 Solar Diffuser Characterization and Conversion from Solar Irradiance to Radiance

The solar radiance is derived from the solar irradiance and knowledge of the scatter characteristics of the white paint on the Hyperion cover. In mathematical terms, the solar radiance is defined as

$$L_{solar}(\lambda, \Theta_{sun}, \gamma) = \cos(\Theta_{sun}) * E_{solar}(\lambda) * r_{whitepaint}(\lambda) * BRDF(\lambda, \gamma)$$

where $r_{whitepaint}$ = the relative spectral diffuse reflectance of the white paint at the scatter angle to the Hyperion view of the panel
BRDF = the ratio of the scattered surface radiance at scatter angle, γ, to the radiance from a Lambertian surface
E_{solar} = the solar irradiance as a function of wavelength
Θ_{sun} = the angle of incidence of the sun – 53 degrees.

In order to derive absolute responsivity on-orbit using solar calibration, the scatter characteristics of the diffuse white paint were measured. A Cary 5 spectrometer was used to measure the absolute, total, hemispherical reflectance of a white paint witness sample. This measurement was referenced to a sample of Spectralon. The absolute reflectance of the white paint is shown in Figure 5.3.1.2-1.

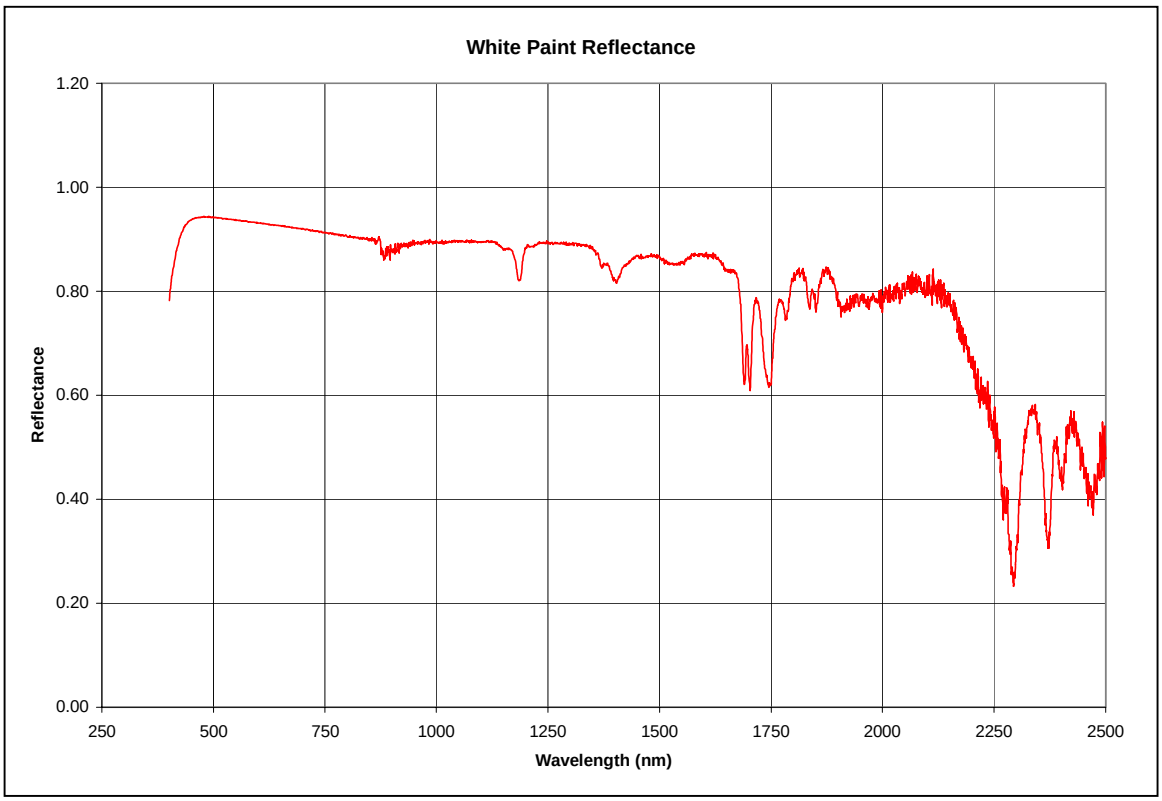

Figure 5.3.1.2-1. Total Hemispherical Reflectance of Hyperion Cover Paint

The TRW Optical Contamination and Scatter Effects Facility (OSCEF) was used to determine the BRDF of the white diffuse paint at the Hyperion solar calibration geometry. Measurements were made at 0.6328 μm. The angle between the sample normal and the detector was fixed at the 37 degrees defined by the calibration cover geometry. In order to understand the sensitivity to variations in the position of the sun within the region defined by the solar baffle, the source angle of incidence was varied between 47 and 58 degrees. In this way, the scatter angle is varied between –10 and –21 degrees. The nominal scatter angle for Hyperion solar calibration events is –16 degrees at a 53 degree angle of incidence. The results of the BRDF measurements are shown in Figure 5.3.1.2-2.

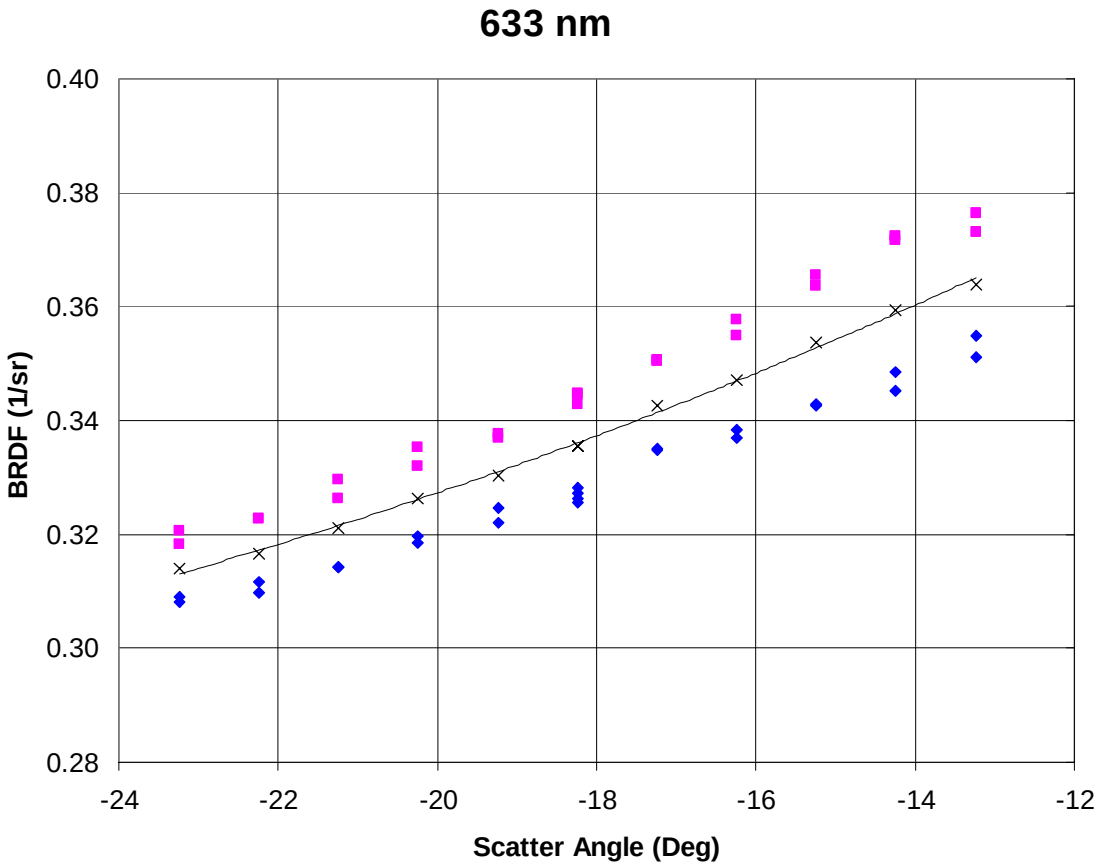

Figure 5.3.1.2-1. BRDF Curves at 633nm

The first solar data collect with both the VNIR and the SWIR focal planes operating was on December 12, 2000. The sun nominally is incident on the back of the telescope cover at a 53 degree angle of incidence. Initial comparisons of the collected data to the solar irradiance models showed differences that were well outside the error bounds of the Hyperion measurement. To verify that the pointing was correct, on January 5, 2001, the spacecraft was maneuvered so that the sun angle varied over ± 6 degrees about normal to induce vignetting of the solar radiation by the solar baffle. The results of the solar scan across the diffuse panel baffle field of regard are shown in Figure 5.3.1.2-2a. The data indicated that the pointing error was approximately –1.9 degrees. On January 26, 2001, the S/C pointing parameters were changed to include the 4.9 degree tilt offset of the Hyperion instrument. A second solar scan was performed on February 9, 2001 showing that the pointing uncertainty was reduced to +0.7 degrees as shown in Figure 5.3.1.2-2b. No further adjustments in the S/C pointing for solar calibrations have been made since then.

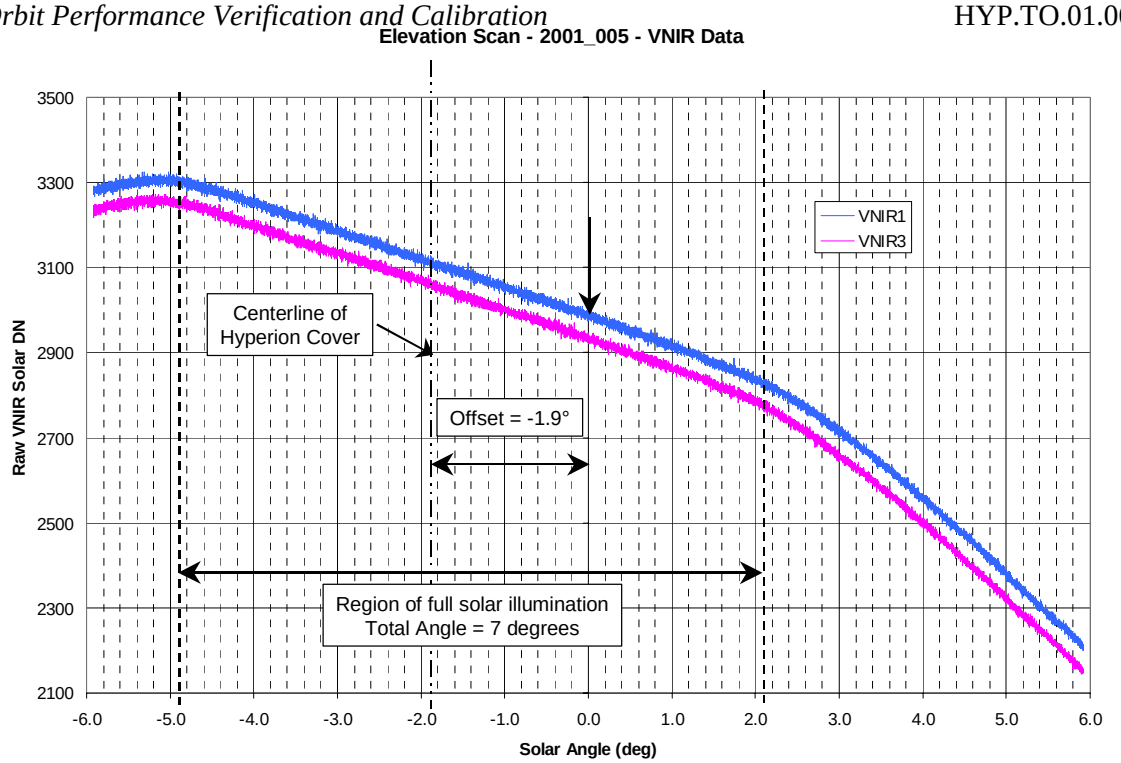

(a) Results of January 5, 2001 Solar Scan

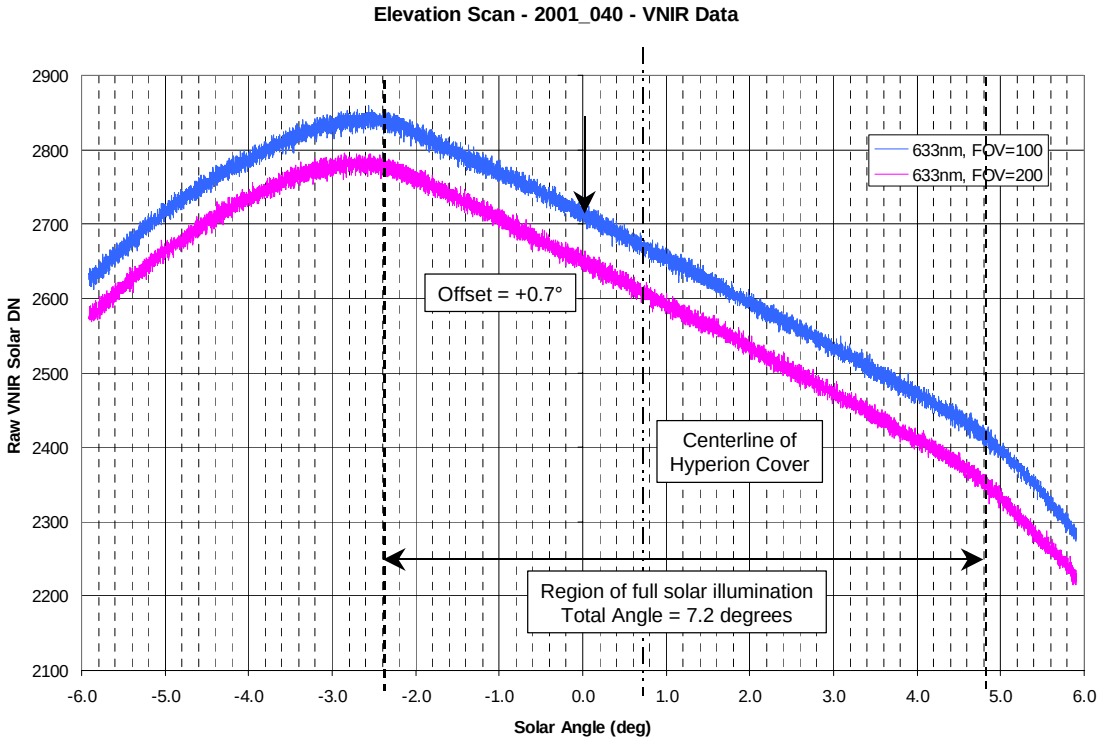

(b) Results of February 9, 2001 Solar Scan

Figure 5.3.1.2-2. Results of the Spacecraft Scan of the Sun Across the Diffuse Panel Baffle.

5.3.2 Comparison of Hyperion with the Solar Irradiance

The responsivity of the Hyperion radiometer has been used to derive a measure of the solar spectral irradiance by viewing the sun on-orbit. By measuring L_{solar} (λ) during a solar calibration a value for E_{solar} (λ) can be obtained and compared with the solar models to perform a cross-comparison.

The first solar calibration with certain solar position knowledge occurred on February 16, 2001 (Day 47 - 2001). The VNIR results are shown in Figure 5.3.2-1. The agreement is better than that expected from the error estimates for the diffuse paint reflectance accuracy and can only be considered a verification of the ground absolute responsivity at the over all accuracy of the solar error estimates discussed in Section 5.3.4 below.

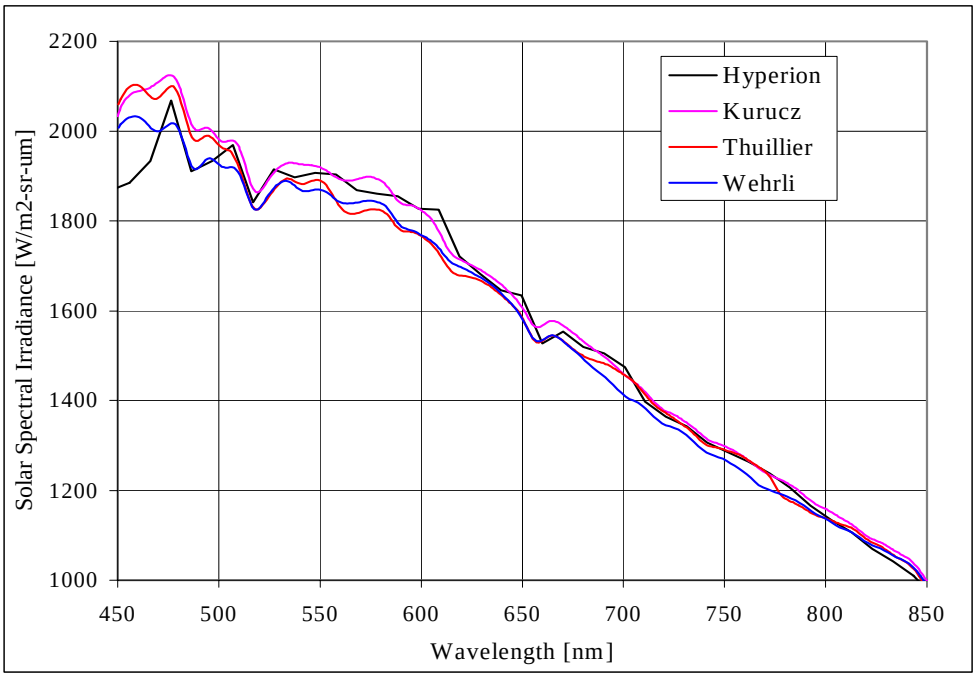

Figure 5.3.2-1 Comparison of the Solar Irradiance Measured by Hyperion on February 16, 2001 with the Solar Spectral Irradiance Models.

Figure 5.3.2-2 shows the SWIR comparison with the WRC Wehrli Model. The sharp drops in the ratios in the 1100 to 1900 nm region are located at absorption features in the paint on the cover indicating the paint measurements are too low in the paint model. Beyond 2200 nm the paint absorption becomes too dominant to permit a solar measurement. Ignoring the presence of overcorrection in the paint absorption, the comparison indicates the Hyperion determined irradiance is 5 to 8 percent above the WRC curve.

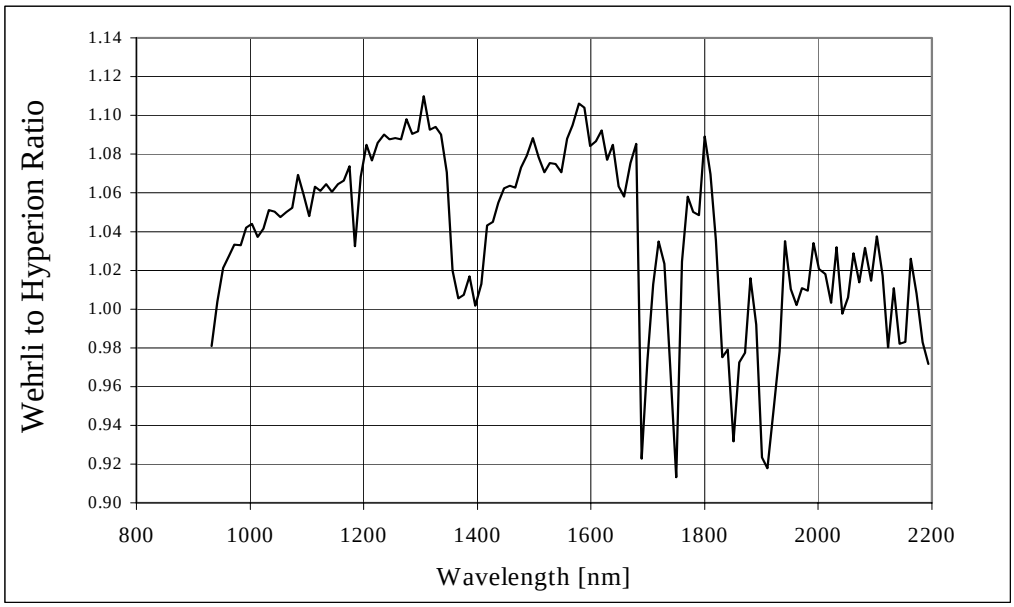

Figure 5.3.2-2 Comparison of the Solar Irradiance Measured by Hyperion on February 16, 2001 with the Wehrli Solar Spectral Irradiance Model.. Note: Features not following the general trend can be traced to the absorption features of the white paint (see Figure 5.3.1.2-1).

5.3.3 Optical Scatter and Signal Contamination

During the processing of the raw VNIR solar calibration data after dark field removal the existence of an additional offset in the dark field appeared at wavelengths in the very blue (< 400 nm) and the very red (< 950 nm). It was noticed because there was obviously no real spectral signal in the dark corrected counts. It is assumed that this is integrated scatter from the optics. Consider that the integrated solar spectrum in the VNIR is relatively large and that the entire integrated spectrum will scatter at very small angles (note that the total FOV of Hyperion is only 0.43 degrees although the required scatter angle will be somewhat different due to optical gain from the fore optics to the spectrometer FPA). This scattered energy will fall on the spectral pixels with very little response in the red or blue and where there is a small signal. The effect will not be noticed at those spectral pixels in the mid wavelength range where the solar response is strong.

This scatter does not appear as wings on the spectral (line) slit response function because radiant energy used for that measurement is limited to the spectral pixel under test and not integrated over the entire solar spectrum. The size of the scatter for a solar calibration data collection is on the order of 70 counts in the VNIR and 10 counts in the SWIR. In practice, an algorithm could be constructed to integrate for each given pixel, a scattered offset term, by summing the signal from all other pixels in the array weighted by the distance between the given pixel and the pixel being summed.

For solar calibration, a fixed supplemental dark offset has been derived and is applied so that the responsivities are not affected. When the responsivity array is applied to a scene, however, there will be an apparent excess scene radiance in the spectral regions with low scene radiance. The

responsivity array that has been developed for scene calibration has had the worst regions zeroed out. The regions being calibrated are from 445 nm (pixel 10) to 925 nm (pixel 57) in the VNIR and from 892 nm (pixel 75) to 2466 nm (pixel 231) in the SWIR.

5.3.4 Error Estimates for Solar Calibration

The solar calibration data collection was used to compare the Hyperion measured solar radiance with a theoretical solar radiance. The theoretical solar radiance was based on solar irradiance and then transferred to an estimated solar radiance by knowledge of the scatter characteristics of the white paint on the Hyperion cover. The error estimate for the solar calibration involves the combination of the error of the absolute knowledge of the solar irradiance and the error of the knowledge of the BRDF of the Hyperion cover as shown in Table 5.3.4-1.

The error budget associated with the BRDF has been generated for both the VNIR and SWIR spectral regions. The uncertainty in the solar irradiance model has been deliberately excluded to facilitate an independent comparison of Hyperion measurements of the solar irradiance to existing models (see Figure 5.3.2-1). The BRDF error budget has been divided into sections, 1) the uncertainty in the ground measurements of the scatter characteristics of the white paint and 2) the on-orbit uncertainties introduced in the application of the BRDF model.

A comprehensive list of error terms has been compiled to address uncertainties in the ground based BRDF measurements. These terms include not only the experimental uncertainty of the measurement itself, but also uncertainties in how well the ground samples match the characteristics of the actual Hyperion cover. Since BRDF measurements can not be made at all wavelengths of interest, a wavelength scaling uncertainty has been included. This term accounts for spectral variations in the BRDF.

The on-orbit BRDF uncertainty includes estimates of the accuracy of the model prediction given assumed uncertainties in the knowledge of the pixel wavelength and spacecraft pointing. The latter determines the angle of incidence of the incoming solar radiation as well as the scatter angle.

Table 5.3.4-1 Solar Error Estimates

line		VNIR	SWIR
1	**TOTAL ACCURACY (%)**	**6.75**	**8.64**
2	**WHITE PAINT SCATTER MEASUREMENT ERROR (%)**	6.25	7.42
3	White Paint BRDF Measurement Uncertainty	6.15	7.33
4	BRDF sample to sample variation	3.51	3.51
5	BRDF measurement uncertainty	0.53	0.53
6	BRDF measurement SNR	0.10	0.10
7	BRDF measurement repeatability	0.52	0.52
8	Tested white paint sample mismatch with on-orbit cover	3.98	5.64
9	Wavelength scaling uncertainty	3.06	3.06
10	Absolute angle error in BRDF measurements (.06%/degree)	0.10	0.10
11	initial offset (deg)	0.20	0.20
12	error in individual measurement angles (deg)	0.02	0.02
13	detector misalignment (deg)	0.20	0.20
14	boom decentration (deg)	0.20	0.20
15	target angle uncertainty (deg)	1.00	1.00
16	Cary5 Absolute Reflectance Measurement Accuracy	1.13	1.13
17	PTFE aging/contamination	0.10	0.10
18	Sample recess	0.10	0.10
19	Standard inaccuracy	1.00	1.00
20	Electronic drift	0.50	0.50
21	**BRDF ON-ORBIT UNCERTAINTY (%)**	2.49	4.17
22	BRDF model uncertainty (%)	1.80	3.80
23	Wavelength uncertainty (nm)	2.00	2.00
24	S/C pointing knowledge (deg)	0.70	0.70
25	Repeatability of cover position (deg)	< 2 cnt	< 2 cnt
26	Cosine projection error	0.60	0.60
27	S/C pointing knowledge (deg)	0.70	0.70
28	Relative reflectance uncertainty	1.50	1.50
29	Hyperion viewing angle uncertainty(%)	0.60	0.60
30	Mechanical assembly tolerance (deg)	0.50	0.50
31	**INSTRUMENT REPEATABILITY (%)**	0.50	1.50
32	ASP Temperature Drift		
33	FPE Temperature Drift		
34	Dark Current Removal Error		
35	S/C Pointing Uncertainty		

5.4 Additional Instrument Responsivity Verification by Cross-Calibration

It is beyond the scope of this document, but a program of additional verification campaigns will be carried out to augment the on-going results gathered from solar calibration and internal calibration data collection. These include cross-measurements of common sites at the same time between sensors within the constellation of Terra, EO-1 and Landsat 7. In addition, there are

ground truth validation campaigns such as that carried out at Lake Frome, Australia and there is the beginning of a series of lunar calibration data collections by the instruments on EO-1.

Detailed in a separate report, a vicarious calibration effort at Lake Frome in Australia was incorporated into the performance verification of the Hyperion imaging spectrometer instrument. The ground reflectance measurements and atmospheric correction leading to TOA radiances are consistent with the Hyperion ground and solar calibration at the 5 % to 8 % level in the 450 to 850 nm spectral range. The SWIR agreement is 10 % to 15 %.

5.5 End-to-End Measurement Error Estimates

Figure 5.5-1 shows block diagram that is an attempt to be a comprehensive coverage of all error terms for a single measurement of a scene element by Hyperion. The top of the atmosphere radiance measurement error of a scene by a given single pixel at a given spatial location and spectral wavelength is the result of the combination of an absolute bias (systematic) error and a precision error. Each term that exists should be located on one of the boxes. Tables 5.5-1a and 5.5-1b show the error estimates. Table 5.5-1b also indicates the section of this document which discusses the term.

Box 1.0 The absolute bias error is estimated from evaluation of errors present in the overall process of the measurement of the top of the atmosphere radiance. These errors are fixed over the time scale of the mission and are inherently not determinable unless they are revealed outside of the overall measurement process. (e.g. by comparison with a measurement made by a mostly independent process).

Box 1.1 The primary standard of radiance is a scale created by hardware to result in a realization of some physical quantity that can be tied directly to the radiant energy (spectral radiance). This is used in a transfer process to calibrate the responsivity of the radiometer to spectral radiance.

Box 1.2 The Calibration Panel Assembly (CPA) is the secondary standard source of spectral radiance traceable to the primary standard. The CPA was used to illuminate the Hyperion radiometer for determining responsivity in counts per units of illuminating spectral radiance.

Box 1.3 Carrying out the process of item 1.2 above creates bias errors (e.g. the transmittance of the chamber window is a calibration term with a hidden bias error in its determination for use in the calculation of responsivity)

Box 1.4 The internal lamp calibration source is put on the spectral radiance scale at the time of ground calibration. There is a bias error introduced in this step. The lamp is used as a transfer source from ground to space for linkage to the solar calibration once on orbit. The stability of the lamp is a source of bias error if is used to adjust the absolute calibration, otherwise it can be used to expose absolute bias errors.

Box 1.5 The responsivity change on launch is a bias error that must be either estimated or if an update is required then the update contains a bias error.

Box 1.6 External calibration comparisons with other instruments viewing the same point on the ground at the same time exposes absolute bias errors. Ground truth at the time of the measurement is another source of calibration support. These techniques include their own bias errors from the new sources of measurements.

Box 2.0 The precision errors are randomly distributed when they occur from measurement to measurement. The amplitude of these errors can be determined by collecting and comparing many measurements internally for variance about a mean. They occur at a time scale short relative to given pair of measurements can not be removed from the measurement error.

Box 2.1 Once the responsivity has been applied to the raw data counts, relative errors in the pixel to pixel response are a source of random error. The errors produce in-track streaks in the image at a given wavelength. The relative errors can be identified and removed by a streak removal algorithm, but some residual may remain.

Box 2.2 The long term variations in the radiometer responsivity are measured using the solar calibration results. Each responsivity update will have random error present in the process. For example, the long term reflectance of the cover reflectance will drift in an unknown way that is considered random (and not a bias) error.

Box 2.3 A random error term is included to account for uncorrected responsivity drifts between solar calibrations. The internal calibration lamp source measurements can be used to mitigate this error.

Box 2.4 The raw counts of a frame have radiometer artifacts that are removed and a random error is incurred in the process. (These include, e.g., echo, smear, non-linearity and scatter)

Box 2.5 The dark field is measured with the cover closed before and after the scene exposure. The frame of counts used to remove the dark field present at the time of the exposure are calculated by interpolation and a residual random error remains after the process.

Box 2.6 There is a random noise in the counts present in any single frame of exposure in each pixel. The relative error introduced to the measurement result depends on the signal to noise.

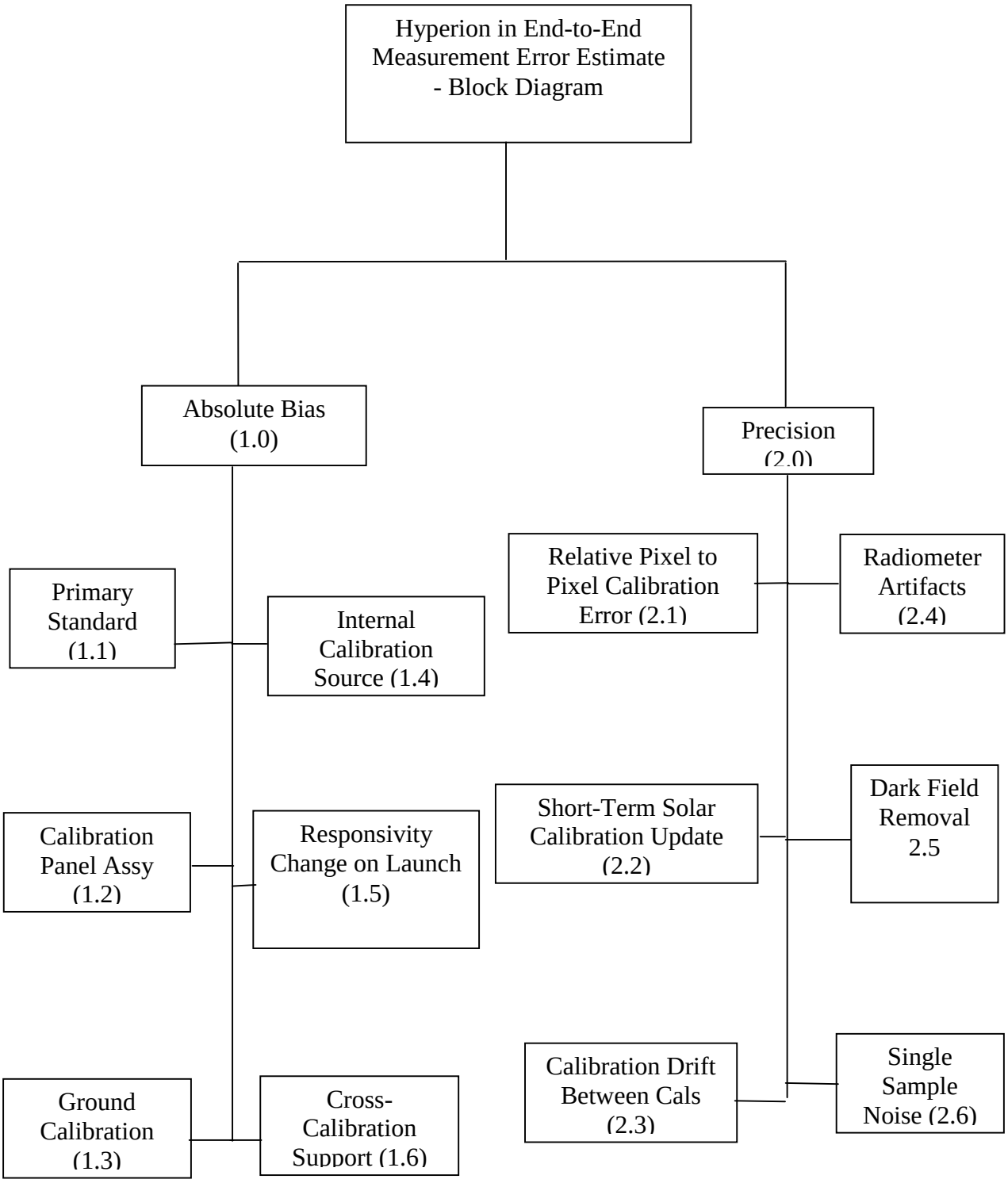

Figure 5.5-1 A Block Diagram of all the Hyperion Measurement Errors

Table 5.5-1a End-to-End Measurement Error Estimates

Total Measurement Error						**VNIR**	**SWIR**
						2.95	**3.39**
Precision from 2nd sheet				**VNIR**	**SWIR**		
				1.60	**2.30**		
Absolute (Systematic) Bias				**2.49**	**2.49**		
Error 1.1 - Primary Standard			**0.29**				
Agreement	0.10						
Ammeter	0.25						
HQE Correction	0.10						
Error 1.2 - Calibration Panel Assembly			**1.83**				
Lamp Irradiance		1.36					
Lamp-Trap Det Distance	0.50						
Precision Aperture Area	0.50						
Filament Alignment Repeatability	0.30						
Lamp Current Repeatability	0.10						
Filter Effective Bandwidth	1.00						
Interpolation between band data points	0.50						
Conversion to Radiance		1.00					
Error 1.3 - Ground Calibration			**0.71**				
Stray Light		0.50					
SiO2 Window Transmittance		0.50					
Error 1.4 - Internal Calibration Source			**1.12**				
Uniformity		0.50					
Repeatability		1.00					
Error 1.5 - Responsivity Change on Launch			**1.00**				
Solar Calibration							
Internal Calibration Transfer							
Error 1.6 - Cross-Calibration Support			**0.00**				

Table 5.5-1b

Precision	**VNIR**			**SWIR**		
RSS combination			**1.6**			**2.3**
Error 2.1 Field Flattening		**0.65**			**1.6**	
Pixel-to-pixel	0.25 (5.0)			1.5 (5.0)		
DCE-to-DCE	0.60 (3.6)			1.6 (4.6)		
Error 2.2 Long Term Solar Calibration Update		**1.0**			**1.0**	
Error 2.3 Calibration Drifts Between Calibration Updated		**0.3**			**0.3**	
Error 2.4 Radiometer Artifacts		**0.64**			**1.07**	
Echo Residual	-			0.8 (4.3)		
Smear Residual	-			0.5 (4.3)		
Non-Linearity	0.5 (3.5)			0.5 (3.5)		
Pattern Noise	0.05 (3.3)					
Cross-Talk	0.40 (3.3)					
Error 2.5 Dark Removal		**0.78**			**.51**	
Scatter	0.75 (3.2)			0.5 (4.2)		
Interpolation	0.2 (3.2)			0.1 (4.2)		
Error 2.6 Single Sample Noise		**0.2**			**0.52**	

Note: The number in parenthesis is the section that describes the error estimate.

5.6 References

[1] P. Jarecke, K. Yokoyama, "Radiometric Calibration of the Hyperion Imaging Spectrometer Instrument From Primary Standards to End-to-End Calibration" ", *Proc. of SPIE*, Vol. 4135, pp 254-263, July 2000

[2] J. H. Walker, R. D. Saunders, J. K. Jackson, D.A. McSparron, "Standard Irradiance Calibrations", NBS Special Publication No.250-20 (1987)

[3] J. Geist, "Quantum Efficiency of the p-n Junction in Silicon as an Absolute Radiometric Standard.", Appl. Opt. 18, 760 (1979)

[4] J. Geist, E.F. Zalewski and A.R. Schaefer, "Spectral Response Self-Calibration and Interpolation and Silicon Photodiodes", Appl. Opt., 19, 3795 (1980)

[5] N. P. Fox, "Trap Detectors and Their Properties", Metrologia, 28, 197 (1991)

[6] W. M. Doyle, B. C. McIntosh and J. Geist, "Implementation of a System of Optical Calibration Based on Pyroelectric Radiometry", Optical Eng., 15, 541, (1976)

[7] E. F. Zalewski and C. C. Hoyt, "Comparison Between Cryogenic Radiometry and the Predicted Quantum Efficiency of pn Silicon Photodiode Light Traps", Metrologia, 28, 203, (1991)

[8] C. Wehrli, World Radiation Center Davos-Dorf, Switzerland, (WCRP) Publication Series No. 7, WMO ITD-No. 149, pp 119-126, October 1986.

[9] G. Thuillier, M. Herse, P. C. Simon, D. Labs, H. Mandel, D. Gillotay, and T. Foujols, "The visible solar spectral irradiance from 350 to 850 nm as measured by the SOLSPEC spectrometer during the ATLAS-1 mission", *Solar Physics*, **177**, 41-61, 1998

[10] Kurucz, R. L., I. Furenlid, J. Brault, and L. Testerman, Solar Flux Atlas from 296 nm to 1300 nm, National Solar Observatory Atlas No. 1, 1984.

6 SPECTRAL VERIFICATION

The chapter discusses the steps taken to determine whether the pre-flight spectral calibration is applicable to on-orbit operations. The results indicate that for the SWIR spectral wavelengths, the pre-flight calibration should be used. The results for the VNIR spectral wavelengths suggest that a rotation may have occurred. However, the pre-flight calibration will be used because the changes observed on-orbit are the same as the pre-flight results within the errors of the measurements

6.1 Introduction

The VNIR and SWIR grating imaging spectrometers share a common set of fore-optics and slit. The Hyperion fore-optics is a reflective telescope design. The fore-optics image the Earth onto a slit that defines the instantaneous field-of-view (fov) of 0.624^0 wide (i.e., 7.5 Km swath width from a 705 Km altitude) by 42.55 μ radians (30 meters) in the satellite velocity direction. A dichroic filter behind the slit reflects the image spectrum from 400 to 1,000 nm to one spectrometer (bands 1-70) and transmits the spectral information from 900 to 2,500 nm to the other spectrometer (bands 71-242). The imaging spectrometers used the NASA JPL 3-reflector Offner design with convex gratings. The two grating imaging spectrometers relay the slit image of the Earth to two focal planes at a magnification of 1.38 :1. The focal plane dimension parallel to the slit axis provides the cross-track spatial image of the Earth through the slit while the axis perpendicular to the slit provides the spectral information on each cross-track pixel.

The final absolute calibration file extends from band 9 (436 nm) to band 57 (926 nm) in the VNIR (49 channels) and extends from band 75 (892 nm) to band 225 (2406 nm) in the SWIR (151 channels). Resulting in a total range from 436 nm to 2406 nm comprised of 200 spectral channels (196 different channels) with 4 channels overlap.

6.2 Pre-Flight Calibration

At multiple locations on each focal plane array (FPA), spectral line profiles were mapped out in detail using a nearly monochromatic source. The source was stepped in wavelength in fractional pixel steps. For the VNIR, a total of 20 spectral steps were taken at each location while a total of 25 spectral steps were performed for SWIR. The data herein was taken in late June of 1999 (after vibration testing).

Table 6.2.1, and 6.2.2 show the summary of the results for VNIR spectrometer. The numbers were derived by curve fitting a Gaussian function to each of the spectral profile data set. Thus, at each location that a spectral profile was measured, the center wavelength, as well as the FWHM, was derived. In a quick check on the dispersion based on each pair of wavelengths, band 31 was deemed to be an outlier. A doped Spectralon data set was collected in addition to the traditional monochromator test set. The doped Spectralon data set consisted of illuminated Spectralon, as well as illuminated Holmium and Erbium doped Spectralon samples. The doped Spectralon has numerous spectral features, primarily in the VNIR. Based on an independent doped Spectralon calibration, and based on band 31 in the VNIR seeming to be an outlier, the monochromator data at band 31 was replaced with the band 31 results of the doped Spectralon calibration.

A linear fit of the center wavelengths as a function of spectral channel number provides the dispersion (nm/pixel) for the spectrometer. Table 6.2.3 shows the results for 5 FOV locations. Note that the pixel starts at 1, not 0 for the calculation of the dispersion. A second-degree polynomial curve was also fitted through each of the data sets. These curves were used to calculate the maximum cross-track spectral error across the entire FOV of 256 pixels. The results as well as the requirements are listed in Table 6.2.4. The corresponding results for the SWIR are shown in Tables 6.2-5 through 6.2-8.

Table 6.2-1 VNIR Spectral Center Wavelengths

VNIR Channel Center Wavelengths (nm, accuracy +/- 0.5 nm)						
Spectral channel / FOV #	13	~~31~~	31	40	48	57
6	477.4	~~656.5~~	660.8	753.6	834.3	925.4
71	478.5	~~657.5~~	661.5	754.1	834.9	925.1
136	478.0	~~656.8~~	661.1	753.7	834.4	925.3
196	476.8	~~655.7~~	660.2	752.8	833.4	924.4
251	475.25	~~654.6~~	658.1	751.3	831.9	922.8

Table 6.2-2 VNIR Spectral Response Function FWHM

VNIR FWHM of Spectral Response Functions (nm)					
Spectral channel / FOV #	13	31	40	48	57
6	11.23	10.51	10.60	11.12	11.11
71	11.60	10.38	10.85	11.34	11.34
136	11.34	10.26	10.68	11.26	11.31
196	11.38	10.21	10.69	11.35	11.30
251	11.25	10.16	10.62	11.28	11.23

Table 6.2-3 VNIR Spectral Calibration

FOV	Dispersion	Offset
6	10.188	345.19
71	10.164	346.63
136	10.173	345.94
196	10.179	344.74
251	10.184	342.88

Table 6.2-4 VNIR Cross-track Spectral Error

spectral channel #	error (nm)	Requirement (nm)
13	3.59	1.5
31	3.27	1.5
40	3.12	1.5
48	2.98	1.5
57	2.84	1.5

Table 6.2-5 SWIR Spectral Center Wavelengths

SWIR channel Center Wavelengths (nm +/- 0.5 nm)					
Specral channel / FOV #	27	57	87	126	156
6	2314.1	2012.2	1711.2	1314.3	1013.3
71	2314.2	2012.1	1711.4	1315.3	1013.2
136	2314.0	2012.2	1711.6	1315.1	1013.2
196	2313.9	2012.1	1711.6	1315.1	1013.2
251	2313.7		1711.2	1314.2	1012.9

Table 6.2-6 SWIR Spectral Response Function FWHM

SWIR FWHM of Spectral Response Function (nm)					
Special channel / FOV #	27	57	87	126	156
6	10.44	10.64	11.55	10.55	10.69
71	10.45	10.79	11.40	10.60	11.01
136	10.42	10.93	11.84	10.83	11.18
196	10.45	11.05	11.59	10.80	11.19
251	10.19		11.33	10.60	11.02

Table 6.2-7 SWIR spectral calibration

FOV #	Dispersion (nm/pixel)	Offset (nm)
6	-10.0911	2587.26
71	-10.0892	2587.31
136	-10.0884	2587.22
196	-10.0879	2587.15
251	-10.0898	2586.86

Table 6.2-8 SWIR Cross-track Spectral Error

Spectral Channel #	Error (nm)	Requirement
27	0.45	2.5
57	0.17	2.5
87	0.57	2.5
126	0.98	2.5
156	0.45	2.5

The data above was used to determine the center wavelength and FWHM for each pixel in the spectrometer. A linear fit was applied in the spectral direction and a second order polynomial was applied in the spatial direction. The result is the spectral calibration supplied by SpectralL0 and BandwidthL0 and is presented as images below, Fig. 6.2-1 and 6.2-2 respectively.

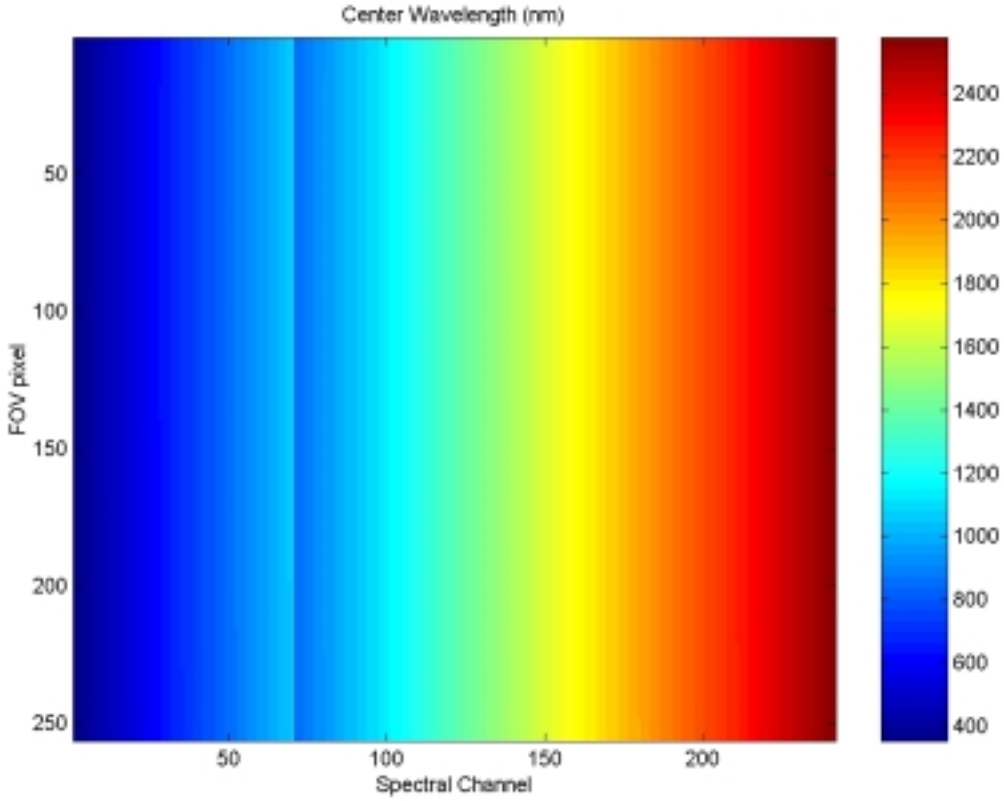

Figure 6.2-1: Image of the Center Wavelength Calibration File

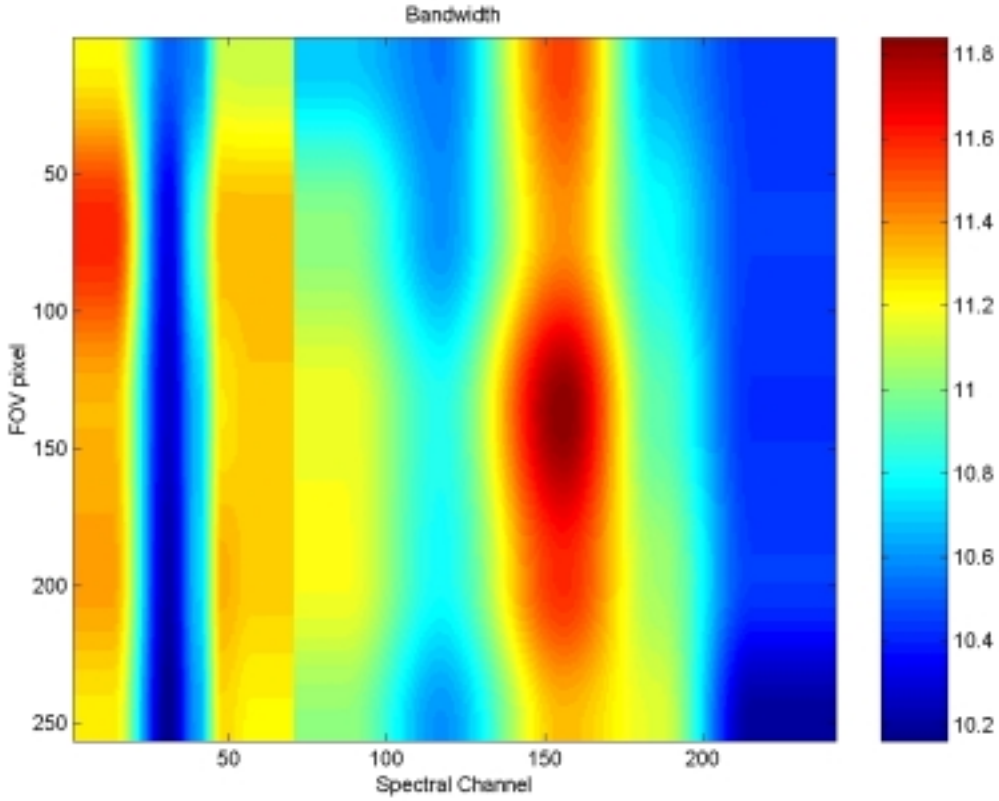

Figure 6.2-2: Image of the Full Width Half Maximum Calibration File

6.3 On-orbit Spectral Verification Process

Various techniques and data collects to verify the pre-flight spectral calibration on-orbit were attempted. The most valuable data collection event was the atmospheric limb collect. The atmospheric limb is essentially a solar calibration scheduled such that the instrument views the sun through different tangent heights of the atmosphere. In order to view the sun, the spacecraft performs a yaw maneuver such that sunlight reflects off the solar calibration panel into the instrument aperture. The result is a collect that is uniform across the field of view and contains spectral features, which can be matched with solar lines, atmospheric lines and absorption lines associated with the paint on the instrument cover. Correlating the positions of these lines with reference data, the center wavelength of each pixel across the field of view for the SWIR spectral regions of the imaging spectrometer was verified. A combination of the oxygen line and a line in the solar profile were used to verify the VNIR spectral calibration.

6.3.1 Atmospheric Limb Data Collection

The Hyperion instrument telescope cover has three normal positions: closed, open and the solar calibration position. When Hyperion views the pre-flight or the moon, the cover is in the open position. When Hyperion views the sun, the cover is in the solar calibration position, which is 37 degrees from the closed position, and the spacecraft must perform a yaw maneuver so that the instrument views the reflection of the sun off the inside of the cover. A diffuse white paint

containing distinct spectral lines coats this surface. The atmospheric limb collect is essentially the same as a solar calibration but timed so that the sun is rising through the limb of the earth and the sun's rays pass through the atmosphere before reaching the instrument, (Fig. 6.3.1-1). The orbital motion of EO-1 allows Hyperion to sample different cross-sections of the atmosphere during image acquisition, which typically lasts 12 seconds. Fig. 6.3.1-2 is an example of the data that the instrument collects during one atmospheric limb collect.

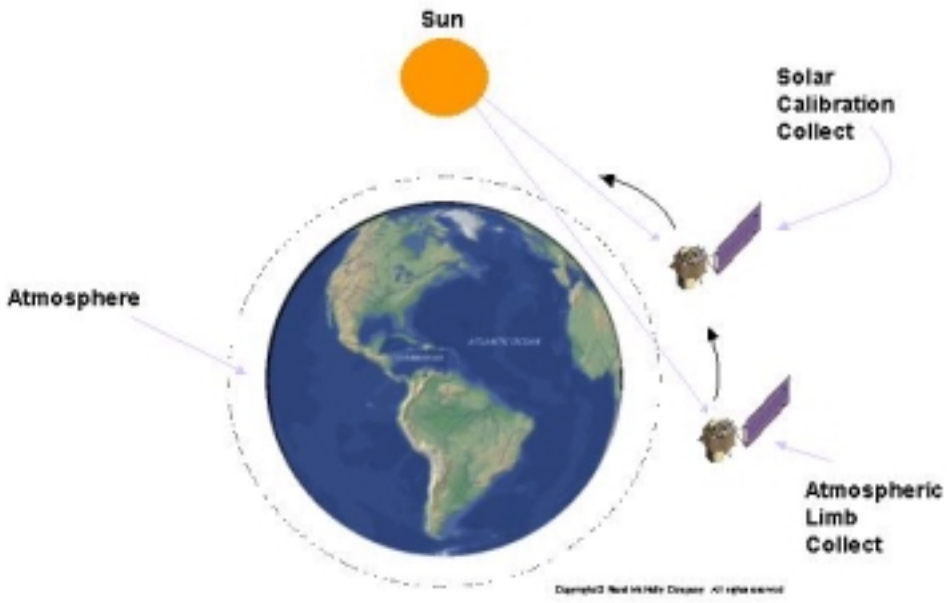

Fig. 6.3.1-1: Schematic of Atmospheric Limb Collect

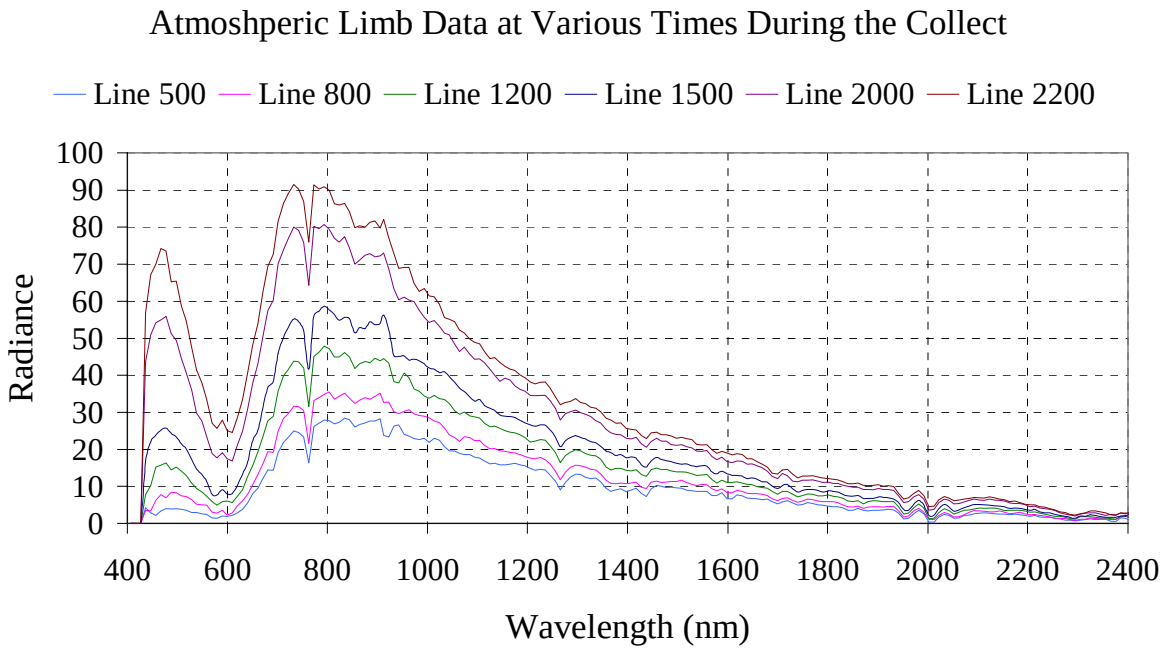

Fig. 6.3.1-2 Hyperion spectral profiles corresponding to six different grazing distances obtained during an atmospheric limb collect on Day 038

6.3.2 Reference Spectrum

In order to perform the spectral validation, the collected limb spectrum must not only have distinguishable features but also be referenced to a known spectrum. Fig. 6.3.2-1 compares the Hyperion spectra with the measured reflectance of the cover paint and the atmospheric lines. Correlation points between the Hyperion spectra and features in the cover paint or atmospheric spectra are indicated. The spectrum for the cover paint was obtained by making diffuse reflectance measurements of paint samples with a Cary 5 spectrometer and BioRad Fourier transform spectrometer at TRW. The atmospheric lines in the SWIR were obtained from PLEXUS —a general user interface built for MODTRAN-3, ver. 1.5.

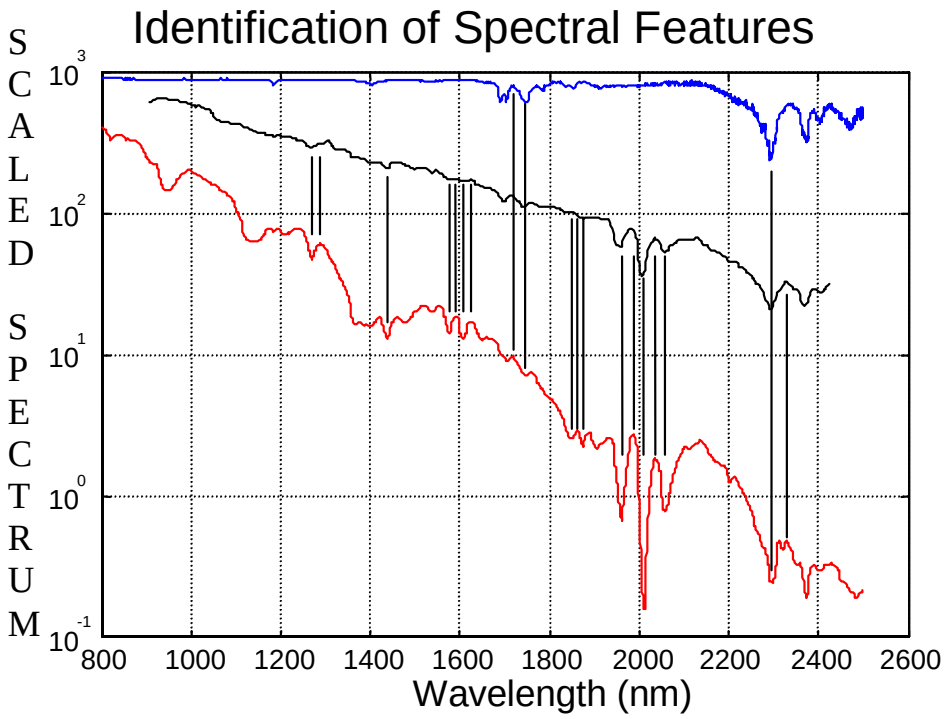

Figure. 6.3.2-1 Sample Hyperion Spectrum (black line) in the SWIR compared with an atmospheric model (red line) and the measured reflectance of the cover paint (blue line).

6.3.3 Data Analysis

The following steps were performed for the spectral verification. The complete process was performed for the SWIR. Due to the lack of sufficiently known reference lines in the VNIR, an abbreviated process was employed for the VNIR. The two axes of the focal plane are referred to as 1) the spectral *band*, and 2) the spatial field-of-view (*FOV*).

1.) *Create Pseudo-Hyperion Spectra from the Reference Data:* The calculated atmospheric limb profile was adjusted to include cover reflectance effects: paint reflectance, BDRF (bi-directional reflection factor), and the spectral angle of reflection. The high-resolution spectrum, sampled at 0.5 nm intervals, was convolved with the instrument's spectral broadening coefficient. This operation was performed on a pixel-by-pixel basis because the broadening coefficient varied slightly across the focal plane. The spectrum was fit with a cubic spline to more accurately determine the wavelength positions of peaks and troughs.

2) Correlate Spectral Features: First, a visual comparison between the Hyperion and reference spectra was made in order to identify features of significant strength and spatial presence to be included in the calculations. For the SWIR, nineteen features were identified in the Hyperion atmospheric limb spectrum. For the VNIR only two features were deemed usable. For each spectral feature—in a given FOV—the location of the peak or trough, in band number units, was

determined by applying a cubic spline and calculating the extremum. This was matched with the wavelength of the corresponding feature in the reference spectrum. We repeated this process for each FOV location to take into account the spectral smile. Calculating peak locations using spline interpolation introduced a ±1.1 nm error distribution (determined using empirical sampling of our high-resolution reference spectrum).

3) *Calculate Band-to-Wavelength Map:* The correlation process in step 2 resulted in a 2D surface: the Hyperion band position of a spectral feature (x), the field of view position (y), and the corresponding wavelength of the feature obtained from the reference spectrum (z). For the SWIR, a low order polynomial fit was applied to statistically reduce noise in the data and produce a band-to-wavelength map for the focal plane. For the VNIR, the comparison was limited to the two known wavelengths.

6.4 SWIR Spectral Verification Results

Pre-flight measurements were made at select wavelengths. There were four spectral features in the atmospheric limb reference spectra that were close in wavelength to these pre-flight measurements. These wavelengths and those corresponding to the spectral band number are compared in Table 6.4-1. The most significant difference occurs in a region where there are multiple lines in the atmosphere. We have reservations about the wavelength accuracy of the calculated features in the vicinity 2000 ± 15 nm (having found another suspected error in the VNIR regime, perhaps related to inaccurate model parameters). The results based on the cover lines are in much better agreement with the pre-flight calibration. The accuracy of the technique is limited to the accuracy of the reference spectra. The next largest source of error is due to the use of the spline in determining the peak and trough positions (±1.1 nm). Overall, this comparison indicates that the on-orbit measurements support the pre-flight calibration to near a third of a pixel. Each pixel has about a 10 nm bandwidth.

Table 6.4-1 SWIR Comparison Of On-Orbit And Pre-Flight Results Fov 136

Spectral Pixel No.	TRW [nm]	On-Orbit [nm]	Delta [nm]	Reference
17	1013.00	--	--	--
47	1315.12	1315.4	+0.28	Atm.
86	1711.55	1710.5	-1.05	Cover
116	2012.19	2015.5	+3.31	Atm.
146	2313.97	2315.4	+1.43	Cover

The pre-flight calibration was extended to the entire focal plane by applying a polynomial fit to the data. The resulting full calibration consisted of a center wavelength value for each pixel. We applied the same process to our results. The following two figures, Fig. 6.4-1 and 6.4-2, compare the results from the pre-flight spectral measurements to the pre-flight based spectral calibration and the on-orbit calibration. Note that for Band 17, Fig. 6.4-1, the center wavelength as well as the variation of the center wavelength across the field of view is in excellent agreement with the pre-flight calibration. For Band 146, Fig. 6.4-2, the on-orbit spectral calibration has about a 1.5 nm offset, and the center wavelength variation across the field of view has the same trend as the pre-flight spectral calibration.

Fig. 6.4-3 presents the difference between the on-orbit and the pre-flight calibrations. The largest difference is in the 2000 nm regime, which is dominated by uncertainties in the reference atmospheric profile. Observed differences are within the accuracy of the verification method.

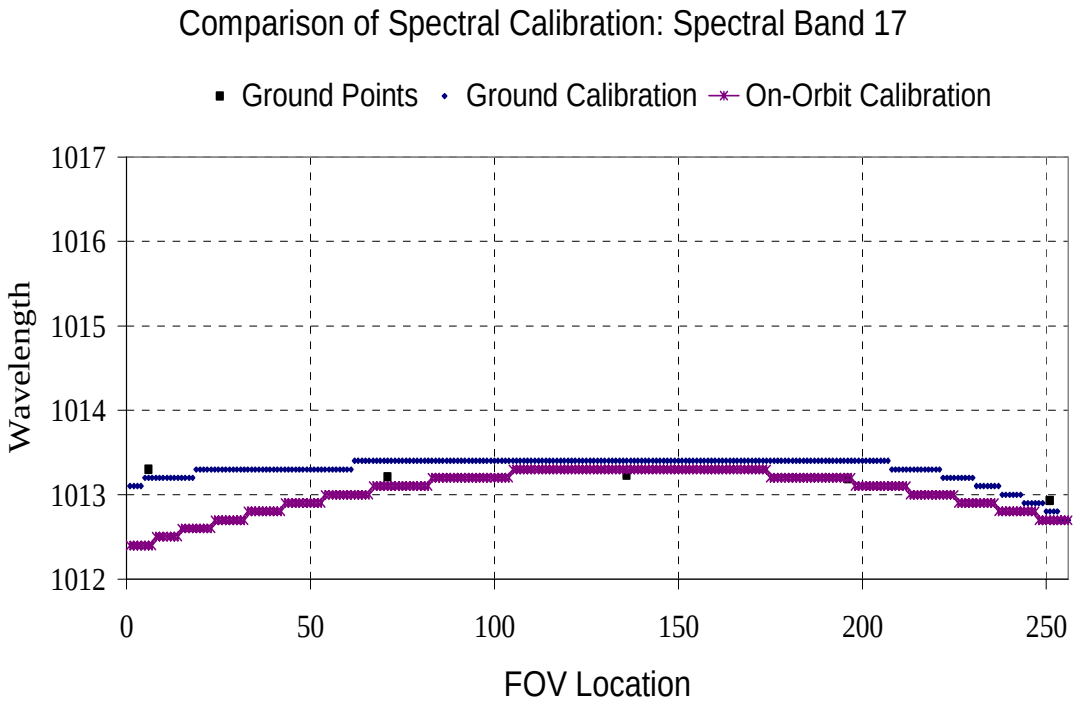

Fig. 6.4-1 Comparison of Spectral Calibrations for Band 17

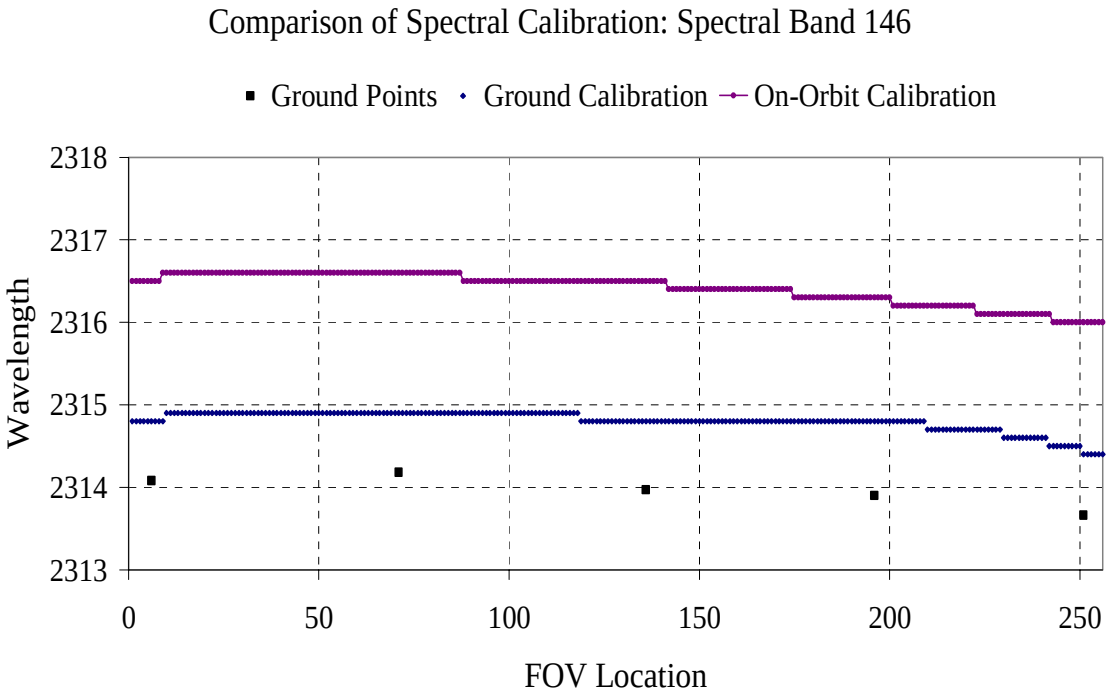

Fig. 6.4-2. Comparison of Spectral Calibrations for Band 146

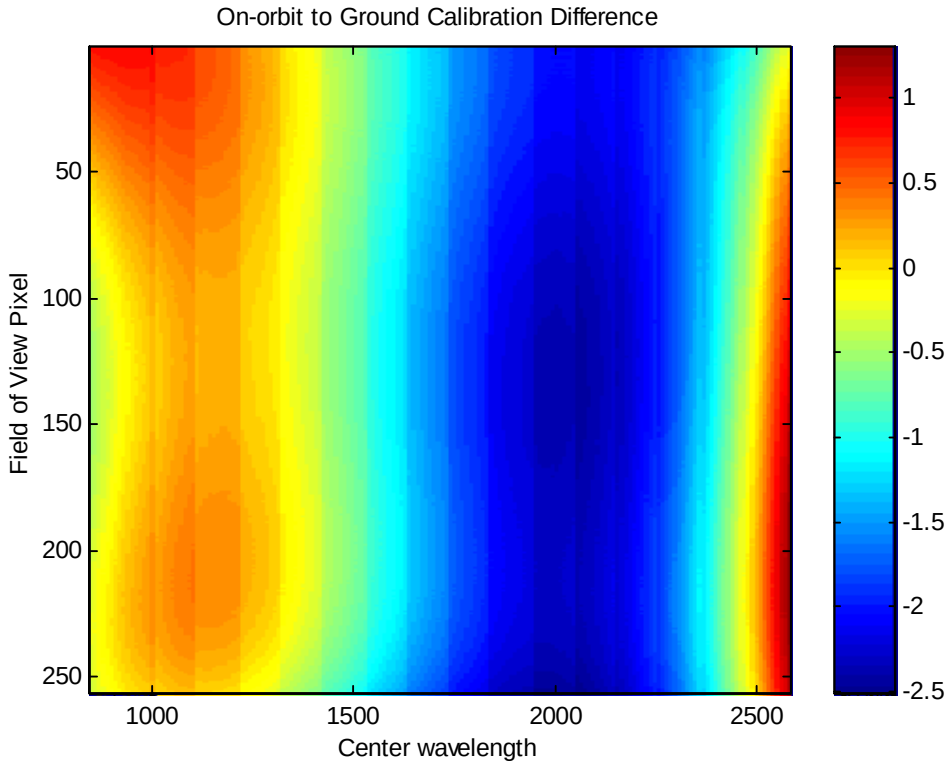

Fig. 6.4-3 Difference Between On-Orbit and Pre-flight Calibration

In addition to the above comparison, the dispersion and cross track spectral error were compared to the pre-flight measurements and requirements. Both results indicate very good agreement between the pre-flight and on-orbit measurements. The SWIR cross track spectral error meets the requirements as shown in Table 6.4-2 and 6.4-3. Recall that the ordering of the spectral channels in the Level 0/1 data products is reversed from the ordering used during the pre-flight testing. As a result, the data is presented with both spectral channel numbers being referenced.

Table 6.4-2 SWIR spectral calibration

	Pre-flight Measurements Pre-Level 0 spectral ordering		Orbit Measurements Pre-Level 0 spectral ordering, using pre-flight offset	Orbit Measurements Level 0 spectral ordering	
FOV #	Dispersion (nm/pixel)	Offset (nm)		Dispersion (nm/pixel)	Offset (nm)
6	-10.0911	2587.26	-10.087	10.106	841.055
71	-10.0892	2587.31	-10.084	10.101	841.775
136	-10.0884	2587.22	-10.082	10.098	842.075
196	-10.0879	2587.15	-10.083	10.097	841.979
251	-10.0898	2586.86	-10.083	10.099	841.582

Table 6.4-3 SWIR Cross-track Spectral Error

Pre-flight Measurement		Orbit Measurement		
Spectral Channel #	Error (nm)	Spectral Channel #	Error (nm)	Requirement
27	0.45	145	0.58	2.5
57	0.17	115	0.42	2.5
87	0.57	85	0.40	2.5
126	0.98	46	0.41	2.5
156	0.45	16	0.97	2.5

6.5 VNIR Spectral Verification Results

The VNIR spectral calibration was based on two lines. A solar line (520 nm) and the oxygen (762.5 nm). Since there were only two points, a complete spectral fit was not possible. Instead the Spectral L0 was adjusted by an offset and a tilt to match the solar and oxygen reference lines. The results are presented below. Table 6.5-1 compares the pre-flight calibration with the on-orbit calibration for a single FOV location. The results indicate subpixel agreement. Figures 6.5-1 and 6.5-2 compare the pre-flight and on-orbit center wavelength across the field-of-view for spectral band 17 and 41, respectively. These bands are closest to the solar line and oxygen line used for this analysis.

Table 6.5-1 VNIR: Comparison of Pre-Flight and On-Orbit Calibration for FOV 136

Spectral Pixel No.	TRW [nm]	On-Orbit [nm]	Delta [nm]
13	478.31	478.52	+0.20
31	661.36	661.96	+0.60
40	752.89	753.69	+0.80
48	834.24	835.22	+0.98
57	925.77	926.95	+1.18

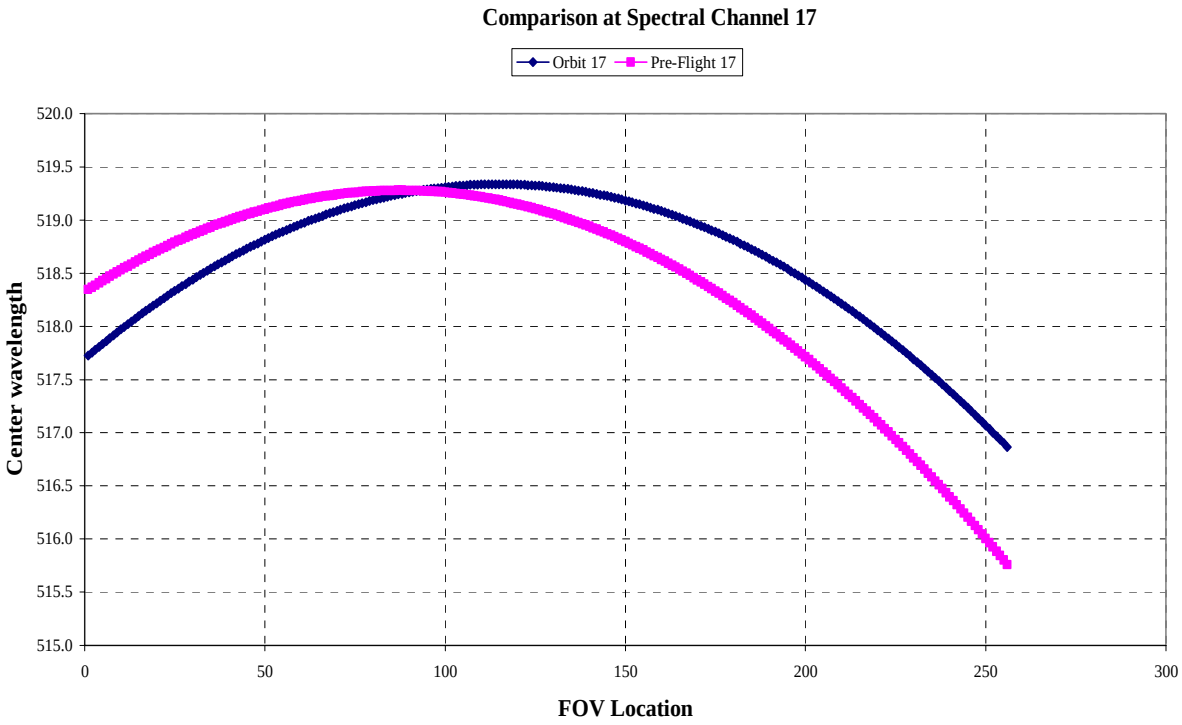

Figure 6.5-1 VNIR Band 17: Comparison of the Pre-Flight and On-Orbit Calibration for the spectral band closest to the Solar Line.

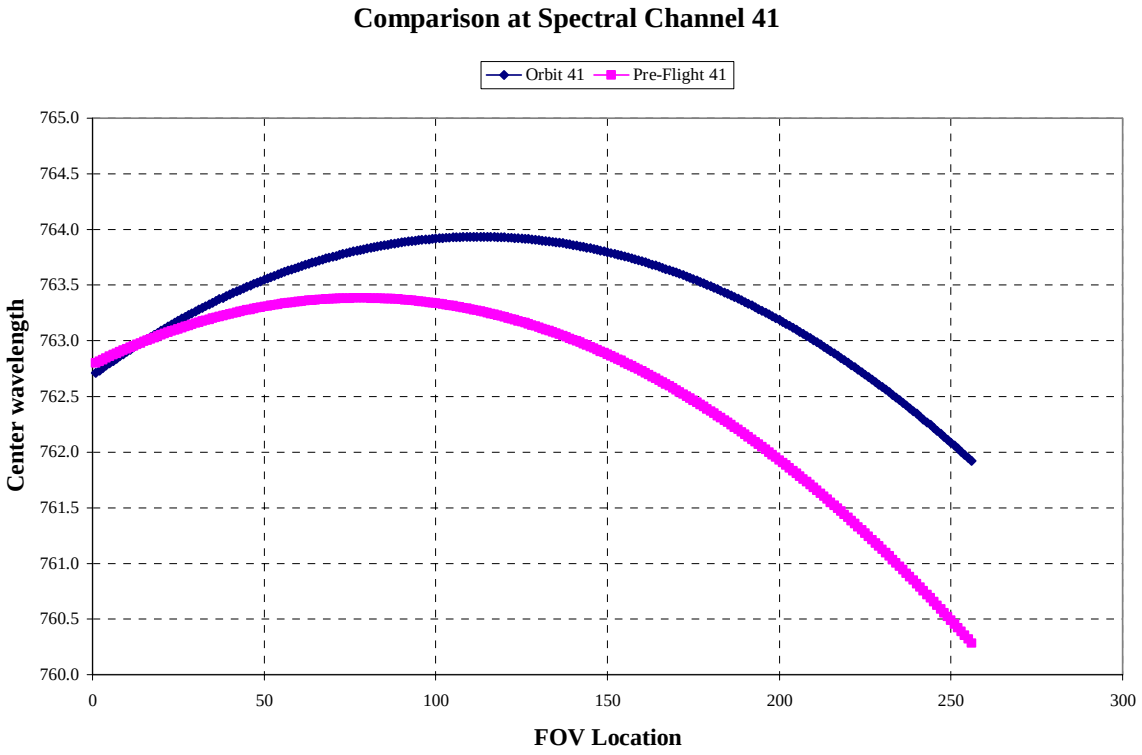

Figure 6.5-2 VNIR Band 41: Comparison of the Pre-Flight and On-Orbit Calibration for the spectral band closest to the Oxygen Line.

The two comparisons suggest a slight rotation may have occurred. The direction of rotation is a reverse of the rotation that occurred at TRW between pre-and post vibration testing. (i.e. the calibration has returned to the pre-vibration testing results). Figure 6.5-3 is the difference between the pre-flight VNIR calibration and the results of the on-orbit fit. The maximum difference was 2.3 nm, which is sub-pixel accuracy and is within the accuracy of the technique employed.

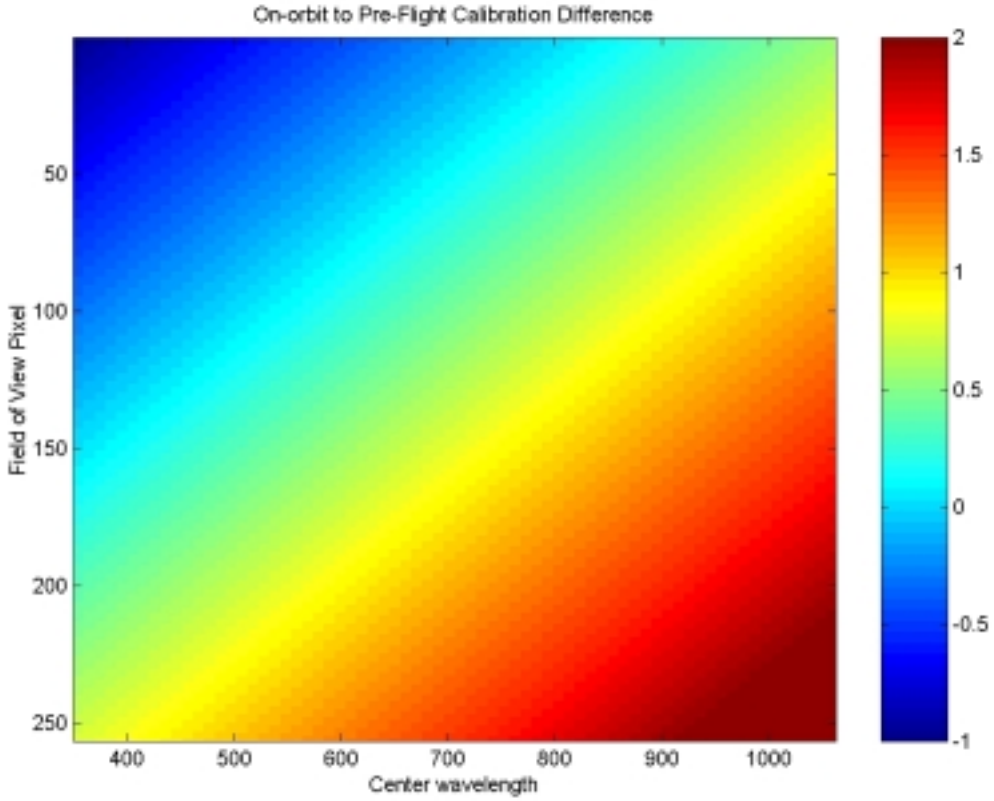

Figure 6.5-3: VNIR On-Orbit to Pre-Flight Difference.

The dispersion and offset were determined by applying a linear fit through the spectral calibration. There is no discernable difference between the two as seen in Table 6.5-2. Since the on-orbit calibration was based on an offset and rotation of the pre-flight calibration, a direct calculation of the on-orbit dispersion was made using the results from the two reference lines. The dispersion was approximately 10.15 and the center wavelength was 346.7. Table 6.5-3 contains the results for the cross track spectral error, which was measured as the difference between the maximum and minimum wavelength for the band numbers indicated. The pre-flight characterization indicated the instrument did not meet specification for this requirement. Although, the on-orbit errors may potentially be smaller, there are not significantly different to change the pre-flight conclusions.

Table 6.5-2 VNIR spectral calibration

	Pre-flight Measurements		Orbit Measurements Level 0 spectral ordering	
FOV #	Dispersion (nm/pixel)	Offset (nm)	Dispersion (nm/pixel)	Offset (nm)
6	10.188	345.19	10.206	344.35
71	10.164	346.63	10.194	345.78
136	10.173	345.94	10.192	346.02
196	10.179	344.74	10.197	345.17
251	10.184	342.88	10.209	343.48

Table 6.5-3 VNIR Cross-track Spectral Error

Pre-flight Measurement		Orbit Measurement		
Spectral Channel #	Error (nm)	Spectral Channel #	Error (nm)	Requirement
13	3.59	13	2.55	1.5
31	3.27	31	2.21	1.5
40	3.12	40	2.03	1.5
48	2.98	48	1.88	1.5
57	2.84	57	1.71	1.5

6.6 Spectral Verification Conclusions

A data collection and analysis process to validate the spectral calibration of Hyperion from space was developed. The process was based on a solar data collect and an atmospheric limb data collect in which the rays of the sun passing through the atmosphere and reflecting off the Hyperion cover is used. The results for the SWIR wavelengths confirm that the Hyperion pre-flight spectral calibration for the SWIR is valid for on-orbit operations. Additional results presented elsewhere with Mt Fitton further support the SWIR spectral characterization. The VNIR results indicate that the rotation that occurred between pre- and post vibration testing on the pre-flight has reversed. However, the maximum difference between the pre-flight and on-orbit calibration are within the measurement error of the technique. As a result, the VNIR spectral calibration will not be updated. The largest sources of uncertainty in the process are suspected errors in the atmospheric profile. The approach used herein is limited to the accuracy of the reference spectrum. It should be noted that through this process the spectral calibration was updated based solely on pre-flight test data but employing techniques developed for on-orbit characterization. Hence the spectral calibration file is SpectralL0_revA.

7 IMAGE QUALITY

7.1 Ground Sample Distance (GSD) and Swath Width

7.1.1 Measurement Description

The GSD is measured by correlating the images from space with map information to determine the distance between the points in the image. The GSD is then the ratio of the distance between the objects and the number of pixels between the points in the image. The swath width is the product of the GSD and the number of spatial pixels (256).

7.1.2 GSD and Swath Width Requirement

The GSD requirement is 30 ±1 meters. The swath width requirement is 7.5 km minimum. The swath width and the GSD are determined by the FOV and IFOV with the satellite altitude. For a GSD of 30 meters and altitude of 705 km the IFOV should be 42.55 μrad. The FOV is determined from the number of cross-track pixels and the IFOV. The FOV should be 256 * 30 meters/705 km = 10.89 mrad = 0.6241 deg. The pre-flight measurement directed a slit image at the center of the FOV and near both edges. For the VNIR the FOV was measured to be 0.62258^{o} and the IFOV was 42.45 μrad. For the SWIR the FOV was measured to be 0.62317^{o} and the IFOV was 42.49 μrad.

7.1.3 On-orbit Measurement Technique

The GSD measurement objective is to calculate the GSD on several scenes to develop a statistically significant result for VNIR and SWIR. An additional objective is to determine any difference between VNIR and SWIR GSD.

The GSD calculation is performed by selecting at least 3 points in the image that have been found on a map. Points 1 and 2 are selected to be as near to the edge of the Hyperion swath as possible while keeping the in-track distance differential to a minimum as shown in the Figure 7.1.3-1. Point 3 is selected to be a significant amount of the swath length from points 1 and 2. It is not important to match the cross-track

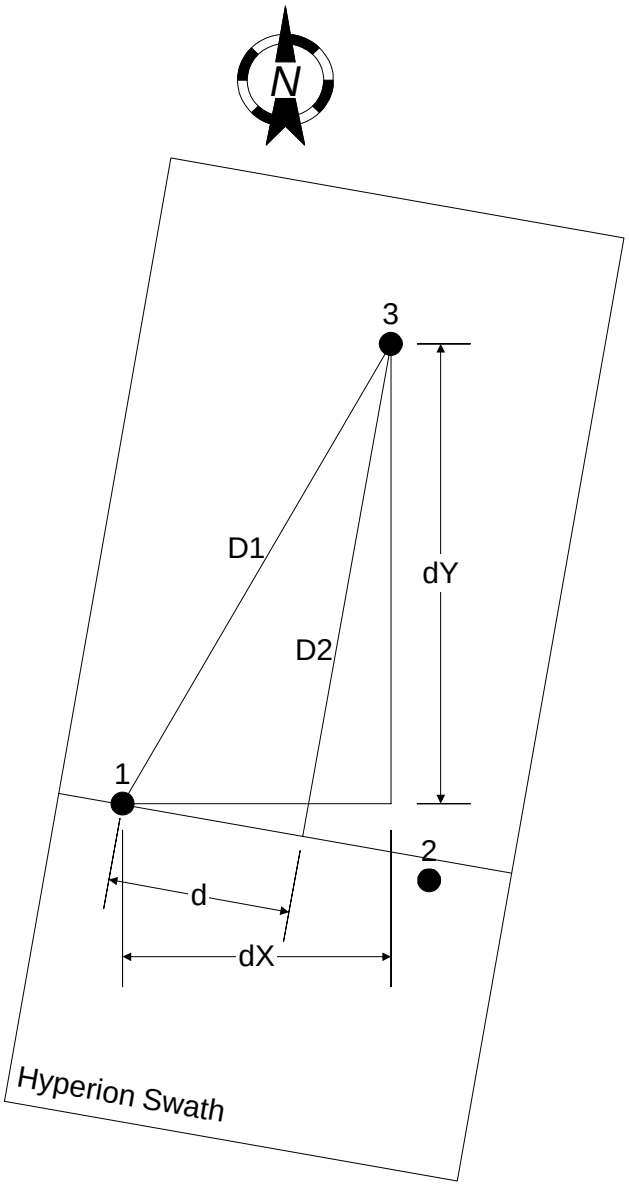

Figure 7.1.3-1 Reference points for on-orbit GSD determination

position because the swath length is so long that the error is insignificant. The map provides the latitude and longitude, which can be converted into ground distance. The pixel value is obtained from the Hyperion image. The cross-track and in-track pixel values for point 1 will be called (p_1,q_1) and (p_3,q_3) for point 3. The diagram in this figure shows the method to compute the Y (in-track) GSD. The distance D1 is

$$D1 = \sqrt{dY^2 + dX^2}$$

The distance d is

$$d = (p_3 - p_1) * X\,GSD$$

The distance D2 is

$$D2 = \sqrt{D1^2 - d^2} = (q_3 - q_1) * Y\,GSD$$

Now the Y GSD can be calculated if an assumption is made for X (cross-track) GSD. A similar process is used to determine the X GSD using points 1 and 2. Then the calculated value for X GSD is substituted into the assumed value that was used for the Y GSD calculation. This is done iteratively until the assumed is the same as the calculated GSD value.

7.1.4 Results and Discussion

The results are summarized in Table 7.1.4-1. Three scenes were used for SWIR GSD calculations and the remaining used for the VNIR only.

Table 7.1.4-1 On-orbit determination of Cross-track and Along-track GSD

Scene	X GSD [meters]	Y GSD [meters]
Washington DC, Day 356	30.207	30.715
New York City, Day 358	30.386	30.545
El Segundo, Day 362	30.143	30.604
Cape Canaveral, Day 013	30.023	30.551
Coleambally, Day 002	30.731	30.435
New York City, Day 040 (SWIR)	30.602	30.563
El Segundo, Day 362 (SWIR)	30.130	30.566
Lake Frome Tarps, Day 5	30.562	30.533
Lake Frome Tarps, Day 5 (SWIR)	30.527	30.529
Average	30.367	30.560
Standard Deviation (meter)	0.25	0.073
Standard Deviation (%)	0.82%	0.24%

The Y GSD can be determined more accurately since the ground error is negligible when compared to the swath length, and this shown by the small standard deviation in the measurements. The determination of the X GSD is limited by the small swath width. Normally the sites that were selected were large streets or coastlines. The accuracy of the pixel selection is about ±1 pixel in both directions. For the map information the primary source was Precision Mapping Streets 4.0 from Chicago Map Corporation. Other sources include a Landsat-5 image over El Segundo from June 28, 1989 and a 4 meter resolution aerial map of Coleambally. The accuracy estimate for the mapping program is ±30 meters. Landsat-7 map accuracy is typically

±100 meters. Differences have been found between the Landsat-5 image and the mapping program to be as much as 200 meters in absolute position. The relative difference is needed for a GSD measurement because the calculation looks at two points on the ground. The relative difference has been measured to be within 20 meters. If a separation of 200 pixels is used between the objects the relative error in the image is ±2 pixels or 1%. The distance measurement from the map is within ±30 meters or 0.5%. Thus the total expected error in X GSD is 1.5% so a standard deviation of 0.87% is reasonable.

7.1.5 Conclusion

The measured GSD is within the GSD requirement and the swath width, using the average X GSD and 255 cross-track pixels to account for the VNIR to SWIR co-registration, is 7.74 km which satisfies the requirement. The pre-flight measurement for VNIR and SWIR GSD had a difference of 0.25%. The on-orbit measurements were consistent but had a larger variance. To get this level of accuracy sub-pixel measurement of the object would be necessary and the object would need to be surveyed. This is not possible with a typical ground scene.

7.2 Modulation Transfer Function (MTF)

7.2.1 Measurement Description

MTF is a measure of spatial resolution of an imaging system. Common methods for measuring MTF use an edge or slit in the lab. For the edge technique a curve fit to an error function can be used to determine the width of the Gaussian Line Spread Function (LSF) analytically. The Edge Spread Function (ESF) can also be processed directly with a derivative to determine the LSF directly. Earlier methods have been presented by Barakat[1,2], Tatian[3] and Jones[4]. For the slit technique the LSF is convolved with slit image. The slit width must be known and be less than half of the pixel. This limitation will minimize the errors caused by the necessity to remove the slit image from the LSF in the processing.

7.2.2 MTF Requirement

The MTF requirement is dependent on the wavelength as shown in the Table 7.2.2-1. The MTF requirement is at the Nyquist frequency which is 1/(2*GSD).

Table 7.2.2-1 Hyperion Modulation Transfer Function Requirements

	VNIR MTF			SWIR MTF			
Wavelength (μm)	0.45	0.63	0.90	1.05	1.25	1.65	2.20
Minimum MTF	0.20	0.20	0.15	0.14	0.14	0.15	0.15

The results are shown in the Table 7.2.2-2 for in-track MTF. The in-track MTF is calculated by multiplying the measured cross-track MTF by 2/π. The MTF was measured using both the edge and slit technique with consistent results.

[1] R. Barakat and A. Houston, "Line spread function and cumulative line spread function for systems with rotational symmetry," JOSA 54(6), 768-773 (1964).
[2] R. Barakat, "Determination of the optical transfer function directly from the edge spread function," JOSA 55(10), 1217-1221 (1965)
[3] B. Tatian, "Method of obtaining the transfer function from the edge response function," JOSA 55(8), 1014-1019 (1965).
[4] R. A. Jones, "An automated technique for deriving MTF's from edge traces," Photog. Sci. Eng. 11(2), 102-106 (1967).

Table 7.2.2-2 Pre-flight measurements of Hyperion in-track MTF

Wavelength (μm)	FOV> 200	Center FOV	FOV < 20
0.500	0.29	0.27	0.22
0.630	0.27	0.28	0.22
0.900	0.24	0.26	0.22
1.050	0.28	0.3	0.28
1.250	0.28	0.3	0.27
1.650	0.27	0.27	0.25
2.200	0.28	0.27	0.23

7.2.3 On-orbit Measurement Technique

The objectives for the on-orbit MTF measurement were to use an edge and bridge for both in-track and cross-track measurements. Examples will be provided in the following sections for an edge and bridge. The edge and bridge must be relatively uniform on both sides. This minimizes the extent to which pre-processing of the image is necessary prior to MTF analysis. The angle of the bridge or edge to the in-track or cross-track direction should be greater than 5 degrees but less than 30 degrees. Figure 7.2.3-1 shows an example of an in-track edge object. The angle of the object to the in-track direction is utilized to sample the edge at a higher resolution than the GSD. Adjacent lines are interlaced depending on the position of the edge in the line. The resulting scan is processed to produce the LSF. In Figure 7.2.3-1, the distance α is the amount that the object changes for in-track line 1. This distance needs to be small relative to a pixel. In this case, α is only 0.2 of a pixel. If the angle is larger then the edge is more gradual than actually tracing the integral of LSF. The effect can be corrected for small values of α by realizing that the distance α is similar to a bridge width after the scene is processed with a derivative. For illustration the cross-track profile and the cross-track profile after the derivative are shown in Figure 7.2.3-1. After the derivative the real profile would be the convolution of the LSF with a 5 pixel ($=1/\alpha$) wide bridge. In a similar fashion the edge image in the in-track direction is the convolution of the LSF with a 0.2 pixel (α) wide bridge. To obtain the MTF the convolved image is processed with the Fourier transform and the result is divided by sinc(0.2). If α is over 0.3 then the sinc used in the MTF processing will get too small and amplify the measurement noise.

It is also desirable to have the edge straight. This allows any errors in the edge location algorithm to be reduced.

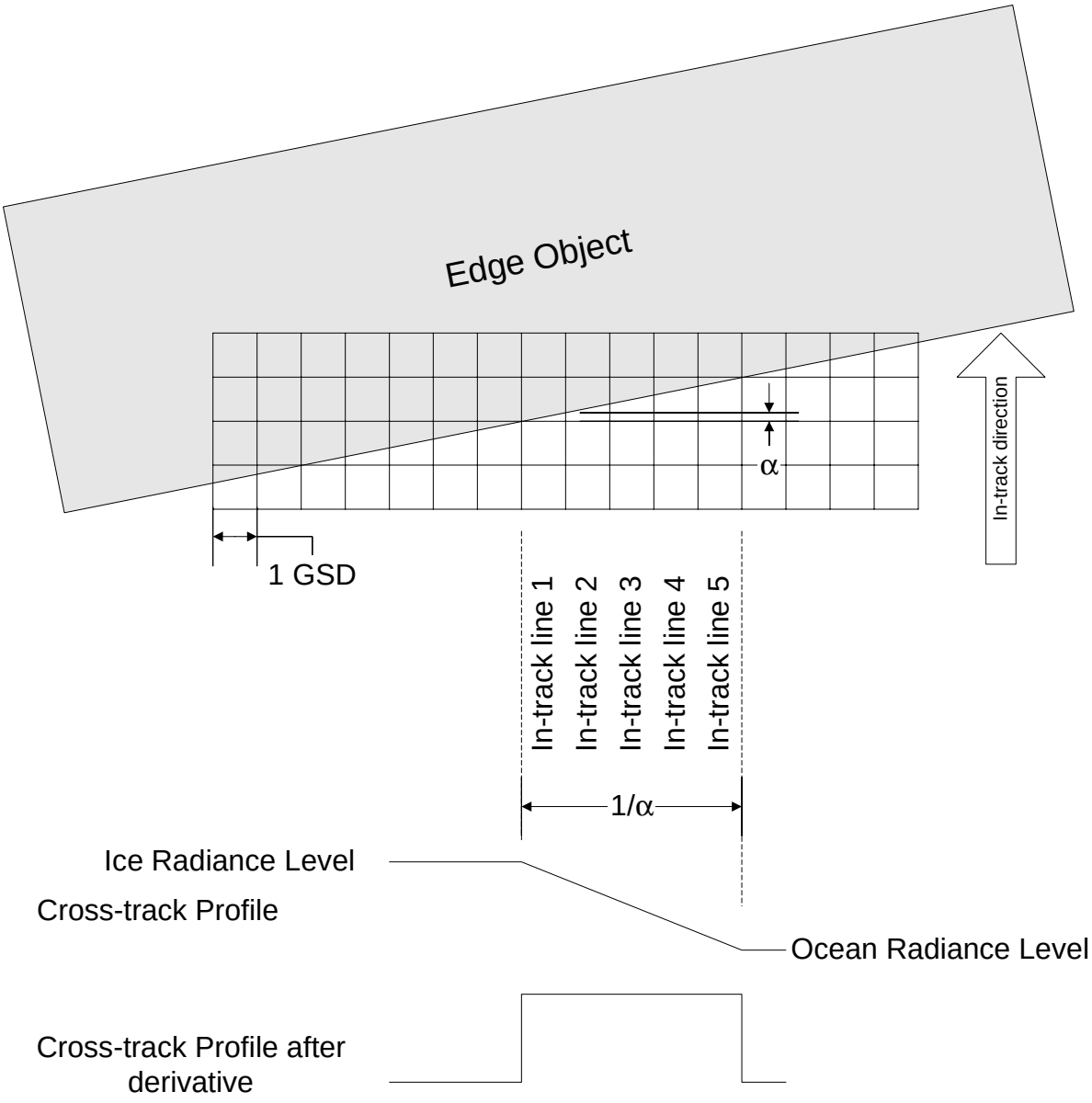

Figure 7.2.3-1 Example of edge object used for in-track MTF analysis

7.2.3.1 MTF Example: Edge scene

This section will provide an example of an edge scene that was used for in-track MTF processing. The image below in Figure 7.2.3.1-1 is from band 28 (λ = 0.630 μm) of the Ross Ice Shelf on Jan 16, 2001. The image to the left is a magnified picture of the image to show the pixel resolution. Each image has a color bar showing the radiance*10. The slope of the edge is larger than desired for measuring in-track MTF but this effect is removed as described in the previous section.

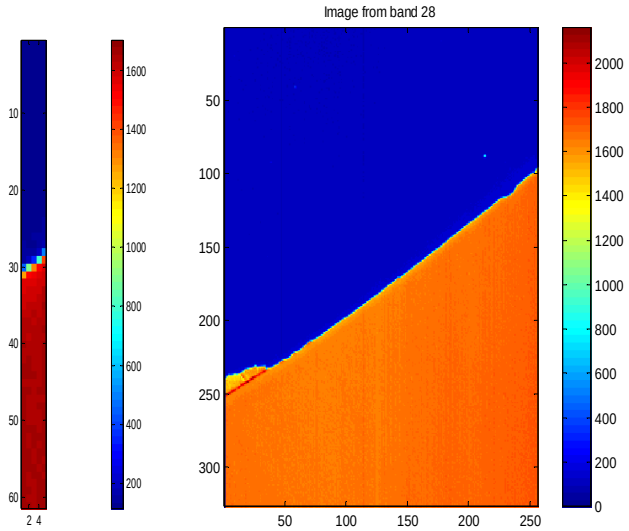

Figure 7.2.3.1-1 Ross Ice Shelf used for In-track MTF

The edge traces in Figure 7.2.3.1-2 are taken from the middle of the scene (field pixel: 134). The edge image from each field pixel is processed with a curve-fit routine to determine the location of the edge for that field pixel. Then the edges are interlaced and the resulting edge is

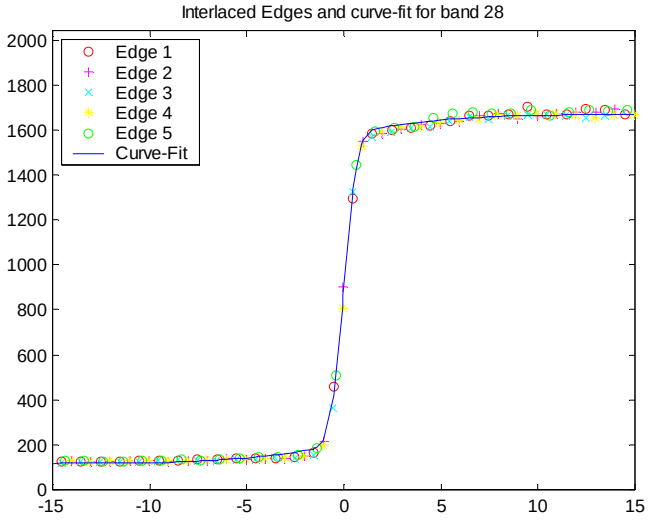

Figure 7.2.3.1-2 Interlaced Edges and Curve-fit

processed with a curve-fit to an error function. The LSF can be calculated from the curve-fit parameters, and is shown in Figure 7.2.3.1-3.

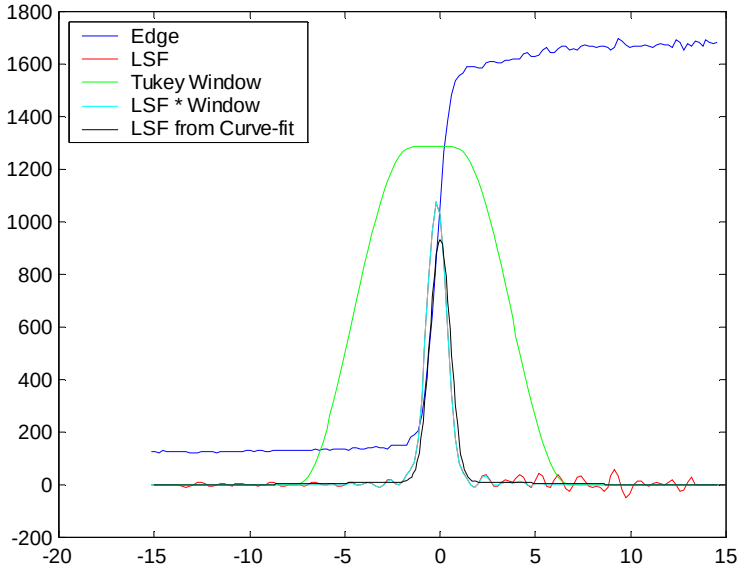

Figure 7.2.3.1-3 Calculated LSF from Interlaced Edge

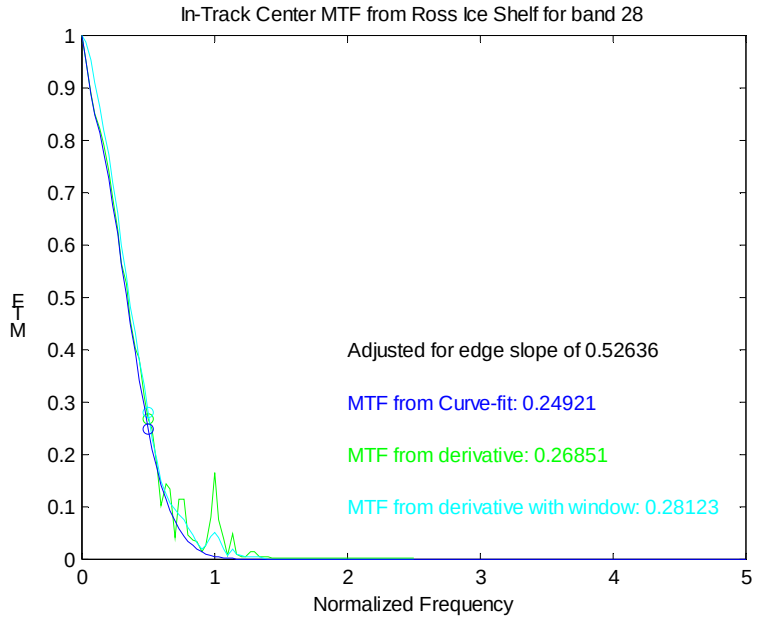

Figure 7.2.3.1-4 Calculated MTF

The edge from each field pixel is also processed with a derivative filter to determine the edge location with the centroid. The edges are then interlaced and the resulting edge is processed with a derivative filter that produces the LSF. The LSF is windowed with a Tukey[5] window to reduce

[5] R. B. Blackman and J. W. Tukey, The measurement of power spectra from the point of view of communications engineering. New York: Dover Publications, 1958

the impact of oscillations away from the edge. The LSF is processed with the Fourier transform to obtain the MTF, shown in Figure 7.2.3.1-4. For this scene the edge slope was significant enough to degrade the MTF by 2% at the Nyquist frequency. The corresponding pre-flight measurement for this wavelength and field position is 0.28.

7.2.3.2 MTF Example: Bridge scene

This section will provide an example of a bridge scene that was used for cross-track MTF

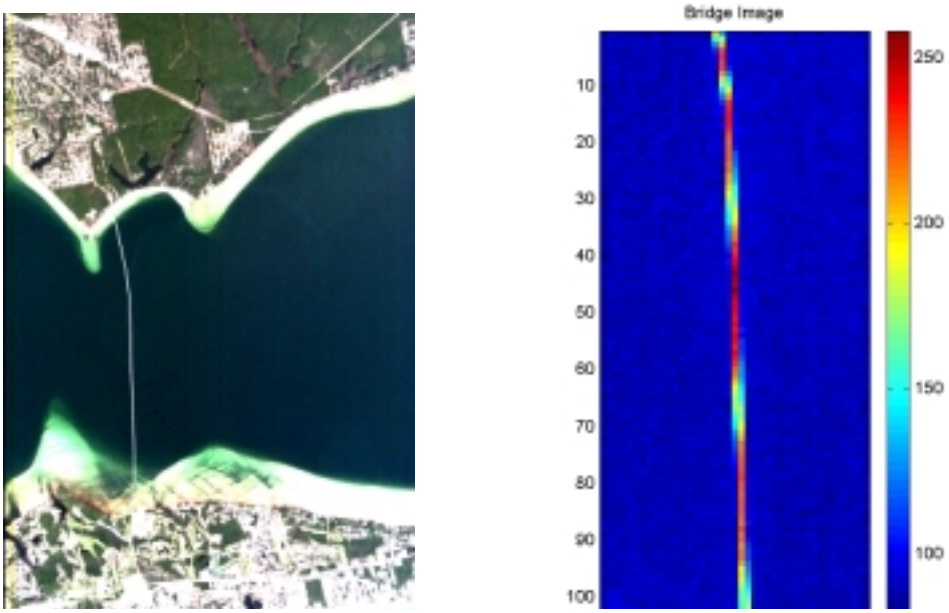

Figure 7.2.3.2-1 Port Eglin Bridge used for Cross-track MTF

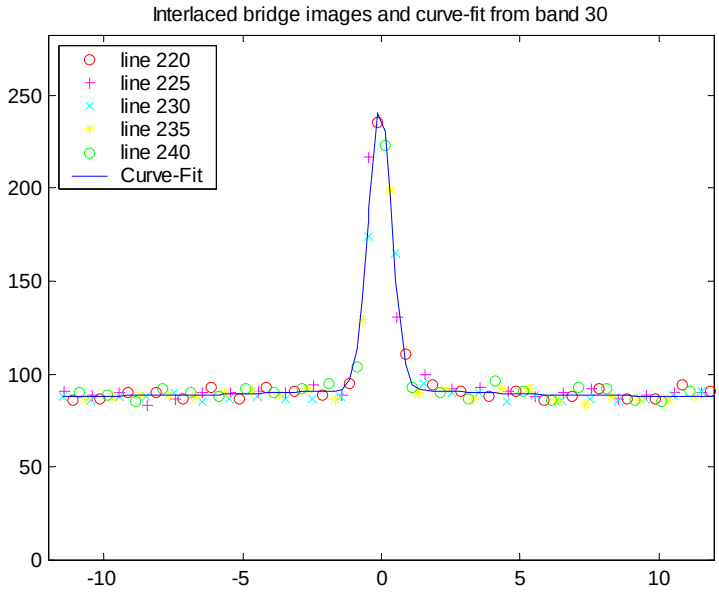

Figure 7.2.3.2-2 Interlaced Bridge Image and Curve-fit.

processing. Figure 7.2.3.2-1 is an image from band 30 (λ = 0.650 μm) of the Mid-Bay bridge near Eglin AFB in Florida. The image was acquired on December 24, 2000. Information on the bridge width was obtained for used in the processing. The width of the bridge is only 13.02

meters or 0.434 of a pixel. As seen in figure 7.2.3.2-1 the angle of the bridge to the in-track direction is quite small. For this reason every fifth line is used to completely sample the LSF. The bridge image from each frame is processed using a curve-fit to a Gaussian to determine the bridge location. Then the images are interlaced to develop the LSF. A curve-fit is then performed using the interlaced data as shown in Figure 7.2.3.2-2. The interlaced data is also sampled a regular intervals to produce the direct LSF. The direct LSF is windowed using the

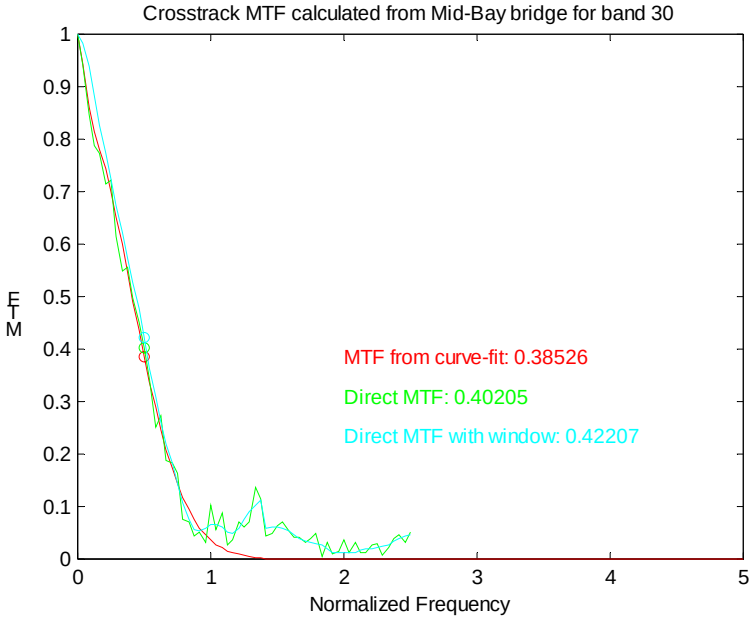

Figure 7.2.3.2-3 Calculated Cross-Track MTF

Tukey window. Each LSF is processed using the Fourier transform and adjusted using the bridge sinc function. At the Nyquist frequency the adjusted MTF is 3% higher than the MTF without the adjustment for the bridge width. The final results are shown in Figure 7.2.3.2-3. The corresponding pre-flight measurement for this wavelength and field position is 0.42.

7.2.4 Results and Discussion

7.2.4.1 In-Track MTF Results

The results for the in-track MTF measurements are presented in Table 7.2.4.1-1. Bands 1-70 are VNIR bands, while 71–242 are SWIR bands.

Table 7.2.4.1-1 In-track MTF Measurements

Scene	Field Pixel	Band	Pre-flight	On-Orbit
Ross Ice Shelf, Day 016	134	28	0.28	0.27
Ross Ice Shelf, Day 016	134	15	0.27	0.23
Ross Ice Shelf, Day 016	134	54	0.26	0.21
Ross Ice Shelf, Day 016	134	91	0.3	0.24
Ross Ice Shelf, Day 016	134	109	0.3	0.26
Ross Ice Shelf, Day 016	74	15	0.29	0.27
Ross Ice Shelf, Day 016	74	28	0.27	0.25
Ross Ice Shelf, Day 016	74	54	0.24	0.28
Ross Ice Shelf, Day 016	74	91	0.28	0.21
Ross Ice Shelf, Day 016	74	110	0.28	0.2
Ross Ice Shelf, Day 016	220	15	0.22	0.27
Ross Ice Shelf, Day 016	220	28	0.22	0.28
Ross Ice Shelf, Day 016	220	54	0.22	0.24
Ross Ice Shelf, Day 016	220	91	0.28	0.24
Ross Ice Shelf, Day 016	220	110	0.27	0.25
Cape Canaveral, Day 045	176	15	0.22	0.25
Cape Canaveral, Day 045	176	28	0.22	0.23
Cape Canaveral, Day 045	176	54	0.22	0.21
Cape Canaveral, Day 045	176	91	0.28	0.28
Cape Canaveral, Day 045	176	110	0.27	0.23
Cape Canaveral, Day 045	176	150	0.25	0.28

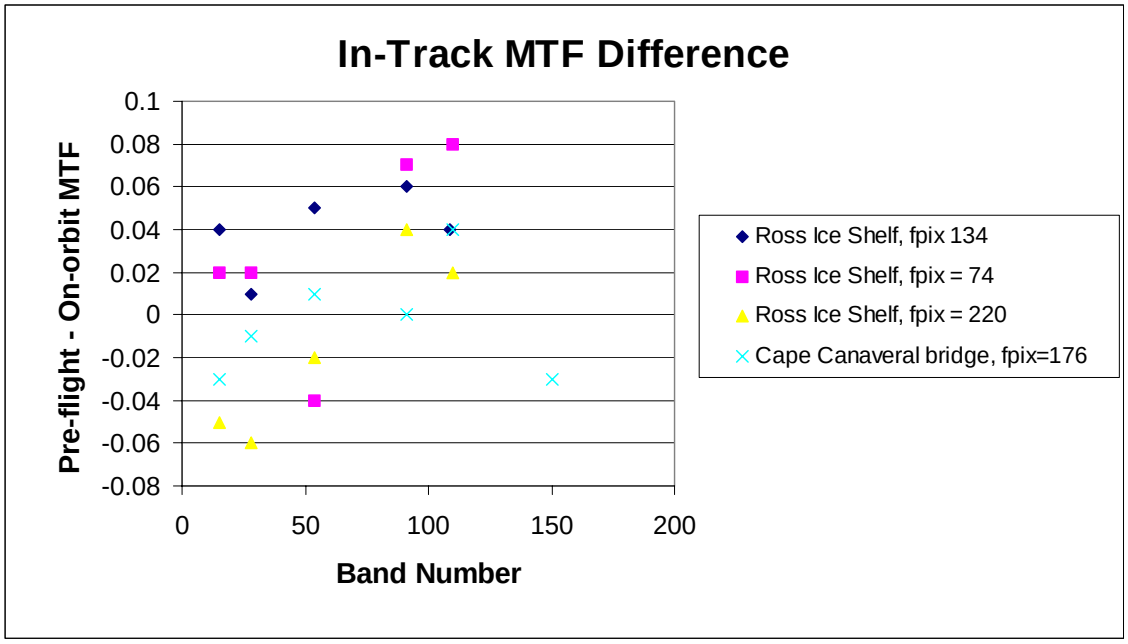

Figure 7.2.4.1-1 In-track MTF Difference from Pre-flight

The differences between the pre-flight and on-orbit MTF results are shown in Figure 7.2.4.1-1. The average in-track MTF error from the on-orbit measurement to the pre-flight measurement is 1.24%. The standard deviation of the difference is 4.0%.

7.2.4.2 In-track MTF Accuracy Discussion

The Ross Ice Shelf scene was taken while the SWIR temperature was 120 K instead of set point of 110 K but this should not affect the system resolution. The scene radiance from the ice and the ocean is compared in Figure 7.2.4.2-1. The contrast beyond band 110 (λ = 1.245 μm) is not sufficient for MTF processing.

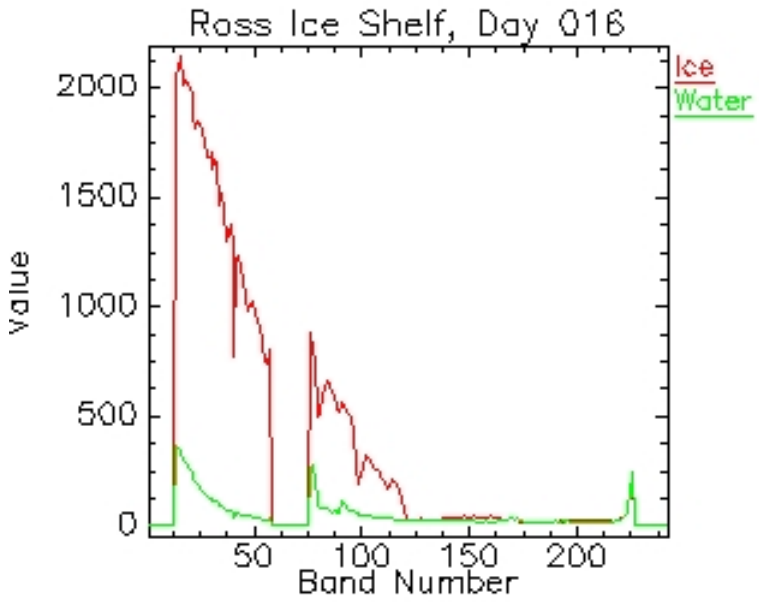

Figure 7.2.4.2-1 Ice – Ocean Spectrum Comparison

In Figure 7.2.4.1-1 a majority of the errors are within ±5% of the pre-flight measurement. The measurements that are significantly outside this range are from the Ross Ice Shelf in the SWIR. The Ross Ice Shelf measurement at band 110 (λ = 1.245 μm) will be discussed further to

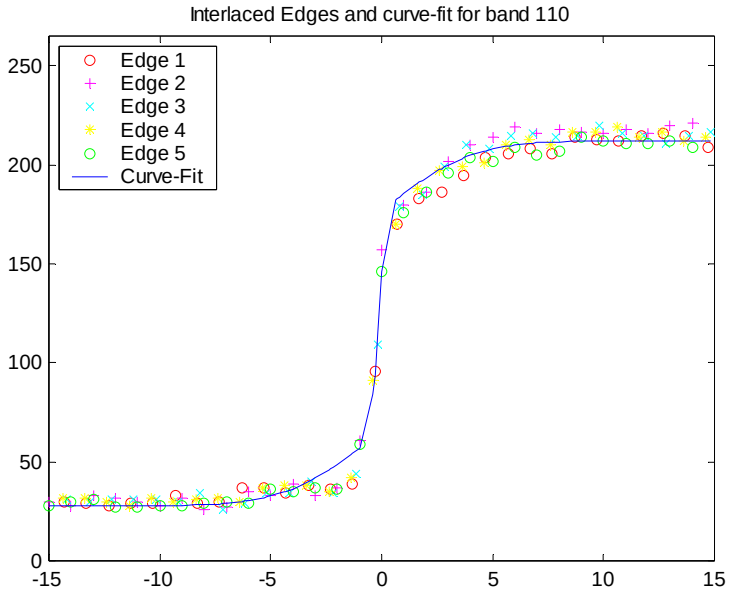

7.2.4.2-2 Interlaced Edges and Curve-fit

describe this measurement anomaly. The interlaced edge profile at a wavelength 1.245 μm of is shown in the Figure 7.2.4.2-2. The radiance near the ice edge in Figure 7.2.4.2-2 is significantly reduced in comparison to Figure 7.2.3.1-2. This could be due to the sunlight transmitting through the thin portions of the ice shelf. The edge profile is processed to determine a curve-fit to a double error function. Figure 7.2.4.2-3 shows the resulting LSF from the curve-fit and the

LSF from the derivative filter. It can be seen that the curve-fit LSF is much more narrow than

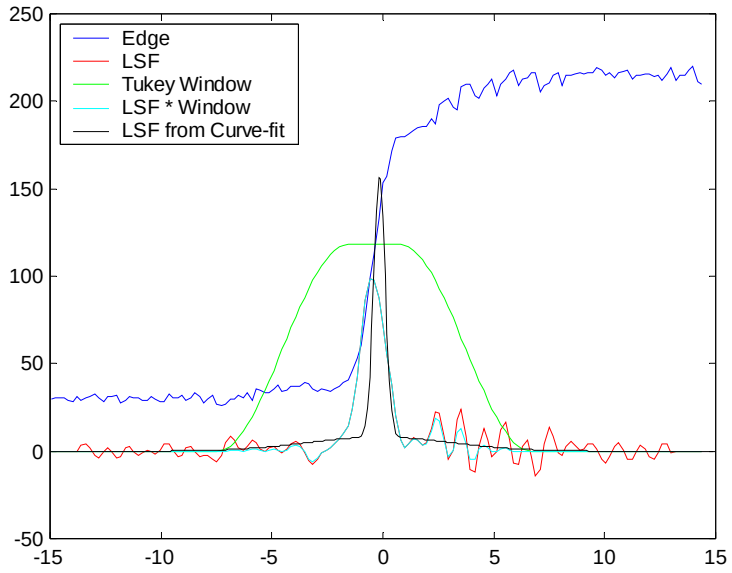

Figure 7.2.4.2-3 Calculated LSF from Interlaced Edge

the LSF from the derivative. Figure 7.2.4.2-4 shows the resulting MTF for the curve-fit and the derivative processing. The abrupt drop in the MTF is caused by the edge slope correction not being performed if it is under 0.5. Typically the MTF value is negligible when the edge slope correction is disabled but this case is the exception.

The reported value from the derivative method is a reasonable value between 0.22 and 0.25. In

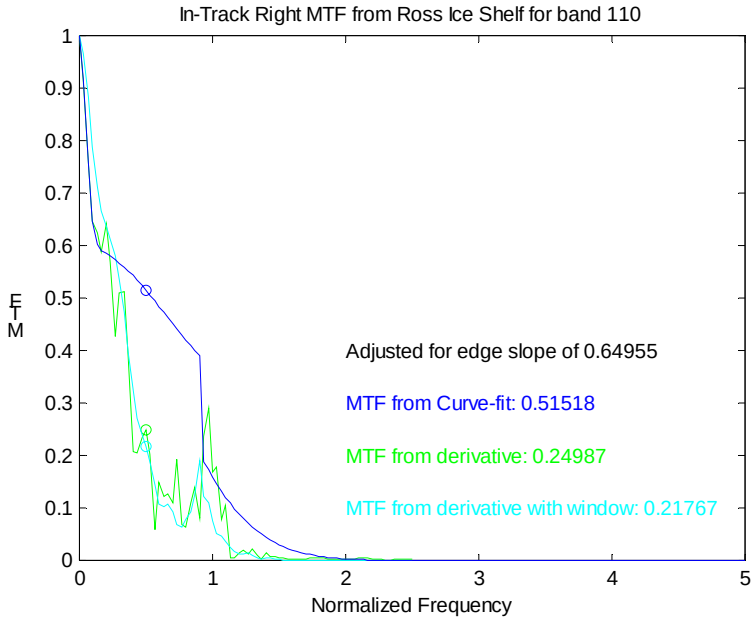

Figure 7.2.4.2-4 Calculated In-track MTF

this case the derivative method produced a more reliable result. In most cases the two methods produce consistent results.

While the accuracy of the ice edge is less than desired in the SWIR bands the measurements made from a bridge near Cape Canaveral resulted in excellent repeatability to the pre-flight measurements. The Cape Canaveral bridge is Florida State Highway 405. This bridge has two movable structures. The separation and width of the bridge was obtained and used in the MTF processing. The width of the bridge is close to 1 GSD, which caused the processing adjustment for the bridge width to be large. The adjustment is a factor of 2 at Nyquist thus it is quite remarkable that the results were so close to the pre-flight measurements.

7.2.4.3 Cross-track MTF Results

The results for the cross-track MTF measurements are presented in Table 7.2.4.3-1 and the differences between the pre-flight and on-orbit results are shown in Figure 7.2.4.3-1.

Table 7.2.4.3-1 Cross-track MTF Measurements

Scene	Field Pixel	Band	Pre-flight	On-Orbit
Port Eglin, Day 359	82	30	0.42	0.4
Port Eglin, Day 359	82	18	0.46	0.42
Port Eglin, Day 359	82	54	0.38	0.4
Moon, Day 038	199	15	0.35	0.35
Moon, Day 038	199	28	0.35	0.34
Moon, Day 038	199	54	0.35	0.39
Moon, Day 038	199	90	0.44	0.367
Moon, Day 038	199	110	0.42	0.367
Moon, Day 038	199	149	0.39	0.31
Moon, Day 038	199	203	0.36	0.29
McMurdo, Day 028	191	15	0.35	0.34
McMurdo, Day 028	191	28	0.35	0.4
McMurdo, Day 028	191	54	0.35	0.33
McMurdo, Day 028	191	91	0.44	0.35
McMurdo, Day 028	191	110	0.42	0.33
McMurdo, Day 028	46	15	0.46	0.42
McMurdo, Day 028	46	28	0.42	0.44
McMurdo, Day 028	46	54	0.38	0.35
McMurdo, Day 028	46	92	0.44	0.39
McMurdo, Day 028	46	110	0.44	0.38

The average cross-track MTF error from the on-orbit measurement to the pre-flight measurement is 3.0%. The standard deviation of the difference is 4.2%.

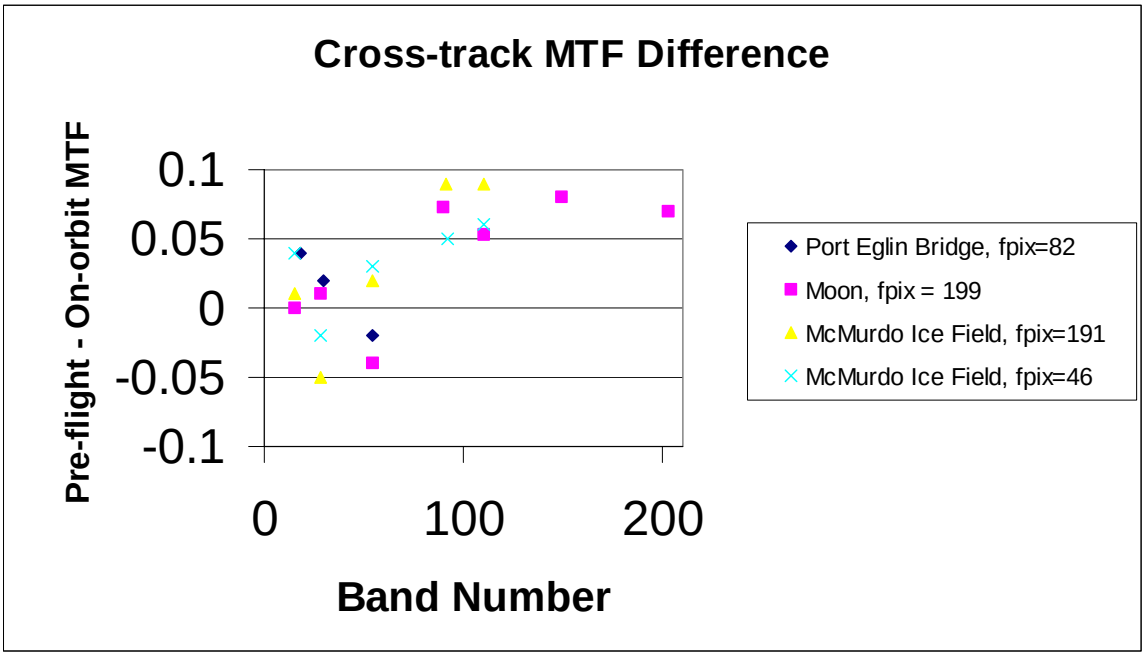

Figure 7.2.4.3-1 Cross-track MTF Difference from Pre-flight

7.2.4.4 Cross-track MTF Accuracy Discussion

The radiance measured from the McMurdo ice field had a similar spectrum to the Ross scene so MTF measurements were not possible beyond band 110. This scene was also recorded with the SWIR at 120 K instead of 110 K but this should not affect the system resolution. The ice edge had similar behavior as described previously with the Ross Ice Shelf.

The spectrum from the moon was excellent but the edge was problematic. To get a full characterization of the edge a few samples should be uniform with the edge signal. For the moon signal only one field location was found that did not have a non-uniform edge in the scene radiance. Figure 7.2.4.4-1 shows a similar edge slope but the scene radiance near the edge is not uniform enough to determine the LSF. This effect did not reduce the MTF accuracy but limited the amount of places in the field that MTF could be measured.

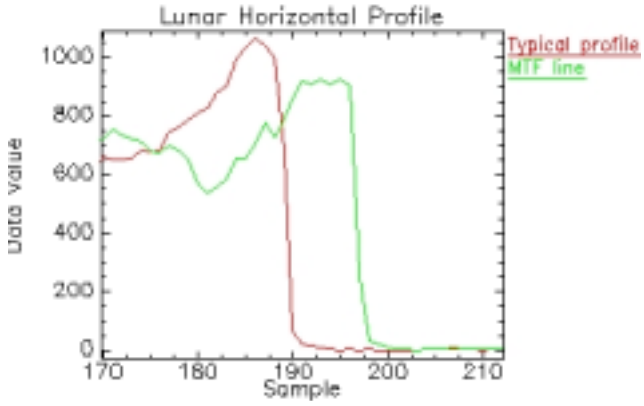

Figure 7.2.4.4-1 Lunar Profile Comparison

The Port Eglin bridge has only been measured with the VNIR. For cross-track MTF processing this scene is ideal. The bridge is quite narrow and it is only a single structure. The MTF measurements also correlated closely with the pre-flight measurements.

From an examination of Figure 7.2.4.3-1 it can be seen that the VNIR measurements have a scatter of ±5% with the average near the pre-flight measurement values. However the SWIR measurements have an obvious positive offset. The actual statistics for VNIR are 0.3% mean and 3.0% standard deviation with 7.1% mean and 2.0% standard deviation for the SWIR. Thus from the statistics only there is more confidence for the SWIR measurements than the VNIR measurements and a MTF degradation must be considered. However when the scenes are considered this conclusion is less certain. Half of the SWIR measurements were from McMurdo, which has an ice edge that is degraded in the SWIR. In the in-track measurements the Ross Ice Shelf had a significant offset in the SWIR but this was negated by the measurement with the Cape Canaveral bridge, which came very close to the pre-flight measurements. There is substantial confidence in the lunar MTF measurement but there is no bridge measurement to verify or negate the postulate that the cross-track MTF in the SWIR has changed. The average shift in the VNIR is negligible so the change would need to be in the SWIR spectrometer. This concern merits an additional scene from the Port Eglin bridge. Additional independent measurements should also be sought from the EO-1 Science Validation Team (SVT).

7.2.5 Conclusion

The on-orbit MTF measurements have demonstrated that the MTF requirements are satisfied. For the in-track MTF measurements there is not a significant change from the pre-flight measurements. The standard deviation is larger than the average difference from the pre-flight measurements thus a degradation cannot be inferred. For the cross-track MTF measurements there is no shift that has been measured in the VNIR but there might be a shift in the SWIR. Additional scenes are necessary to confirm or negate this concern. The SVT will also be consulted for comparable measurements.

The MTF measurements from bridge scenes were able to provide a wider spectral range and were less problematic than the lunar and ice edges. Even scenes with bridge dimensions close to a GSD provided acceptable measurements.

7.3 VNIR / SWIR Spatial Co-registration of Spectral Channels

7.3.1 Measurement Description

The spatial co-registration is a measure of an object's position in the FOV as a function of the spectrometer wavelength. The spatial co-registration is measured by projecting a slit with a broad spectrum that is crossed relative to the spectrometer slit so the spectrometer detects a point source in the spatial direction. The position of the image is measured for all bands in the spectrometer to determine the spatial co-registration.

7.3.2 Spatial Co-registration Requirement

The spatial co-registration of spectral channels requirement is 20% of GSD for each focal plane. The pre-flight results are shown in Figures 7.3.2-1 and 7.3.2-2 for the VNIR and SWIR. The pre-flight measurements directed a point source image at 20 locations. The VNIR requirement was satisfied at all FOV locations except 3 where the exceedance was within the measurement error. The spatial co-registration exceeded the SWIR requirement for most FOV locations but the largest measured value was only 8% above the requirement. The spatial co-registration is the maximum difference between the spatial location as measured in different spectral bands across the focal plane.

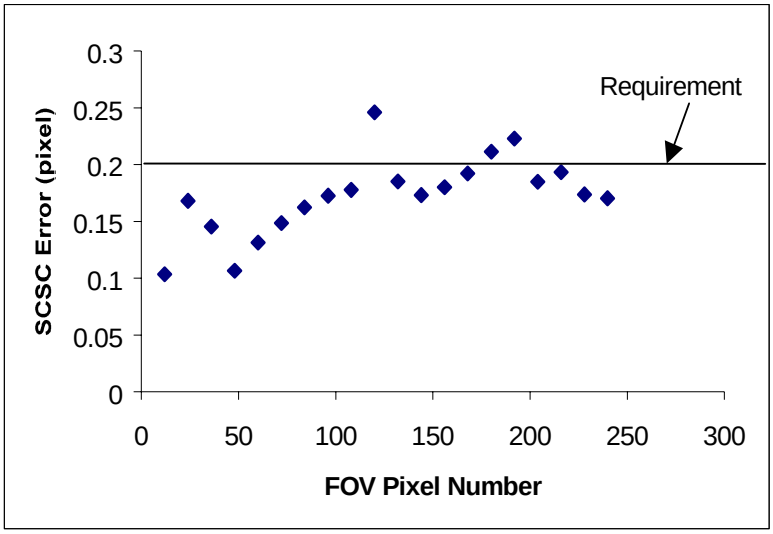

Figure 7.3.2-1 VNIR Spatial Co-registration

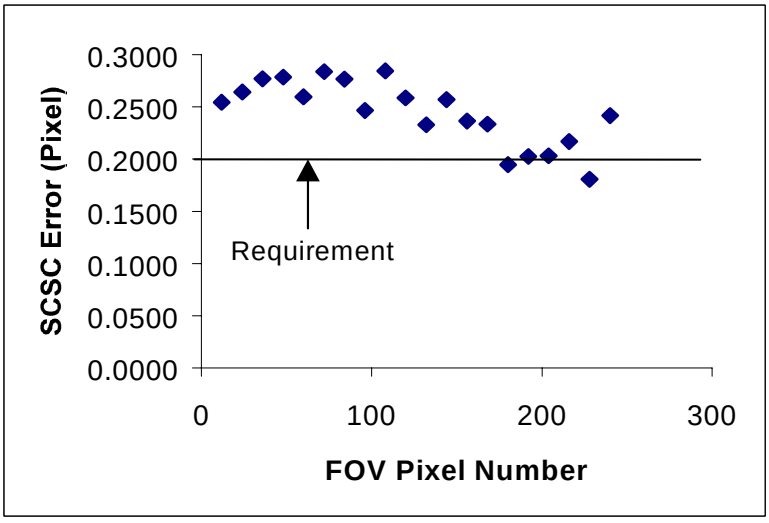

Figure 7.3.2-2 SWIR Spatial Co-registration

Although there was not a requirement for VNIR to SWIR co-registration it was measured during the FOV/IFOV test. Figure 7.3.2-3 shows the spatial co-registration near the center of the FOV. In this figure the SWIR spectral pixels the highest wavelength is at band 71. After level 0 processing the SWIR bands are reversed so the highest wavelength is at band 242. All of the figures after this one utilized level 0 data so the wavelength increases with the bands.

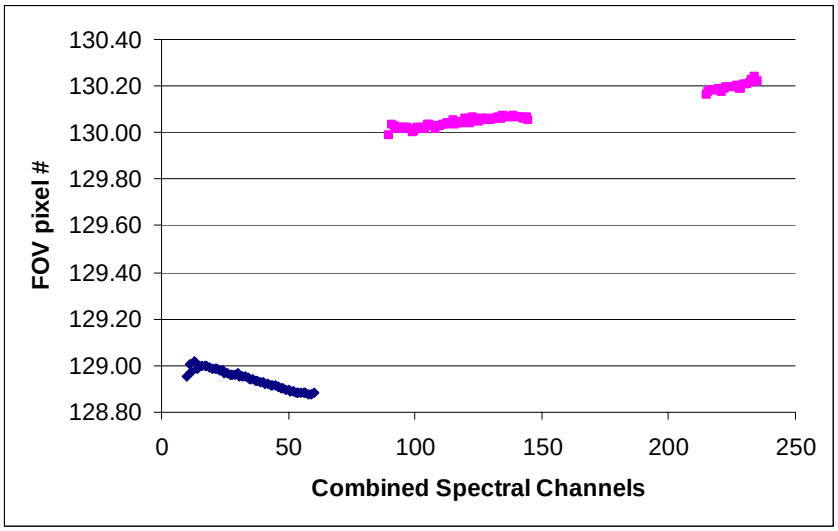

Figure 7.3.2-3 Pre-flight Measurement of Co-Registration of VNIR and SWIR spectrometers near the center field of view

7.3.3 On-orbit Measurement Technique

There was a considerable amount of difficulty in finding the appropriate scene for measuring on-orbit spatial co-registration. The ideal object for spatial co-registration is a point source in the scene with a uniform background. This would have been provided by the active illumination experiment. As an alternative small dense clouds were used over the ocean by calculating the image centroid for each band with sufficient signal. A second method is to use an edge from Ross Ice Shelf and the moon where the edge data is processed using a single error function to determine the edge location. Information was also provided on VNIR - SWIR spatial co-registration by Jenny Lovell from CSIRO in Australia using Ground Control Points (GCPs) in the Lake Frome scene

7.3.4 Results and Discussion

7.3.4.1 VNIR to SWIR Co-registration

Table 7.3.4.1-1 is a comparison of the co-registration measurements between the VNIR and SWIR.

Table 7.3.4.1-1 VNIR to SWIR Co-registration

Source / Scene	Field pixel	SWIR – VNIR
Post Vibe FOV/IFOV	6	+1.24
Post Vibe FOV/IFOV	129	+1.11
Post Vibe FOV/IFOV	251	+1.01
Santa Barbara Cloud, day 3	106	+0.7
Honolulu Cloud, day 363	44	+0.8
Moon, day 38	199	+1.0
Moon, day 38	19	+0.7
Lake Frome, day 5	100, 182, 206	+1.0 – 1.05

The scene that resulted in the highest confidence measurement is the moon from day 38. Figure 7.3.4.1-1 is almost identical to the pre-flight measurement found in Figure 7.3.2-3. The slope for the SWIR co-registration is reversed because the longest wavelength is at band 242 while the pre-flight measurement had the longest wavelength at band 71. Measurements were made using Ross Ice Shelf but the results were not reliable due to the scene reflectance near the edge in the SWIR being lower than the ice reflectance.

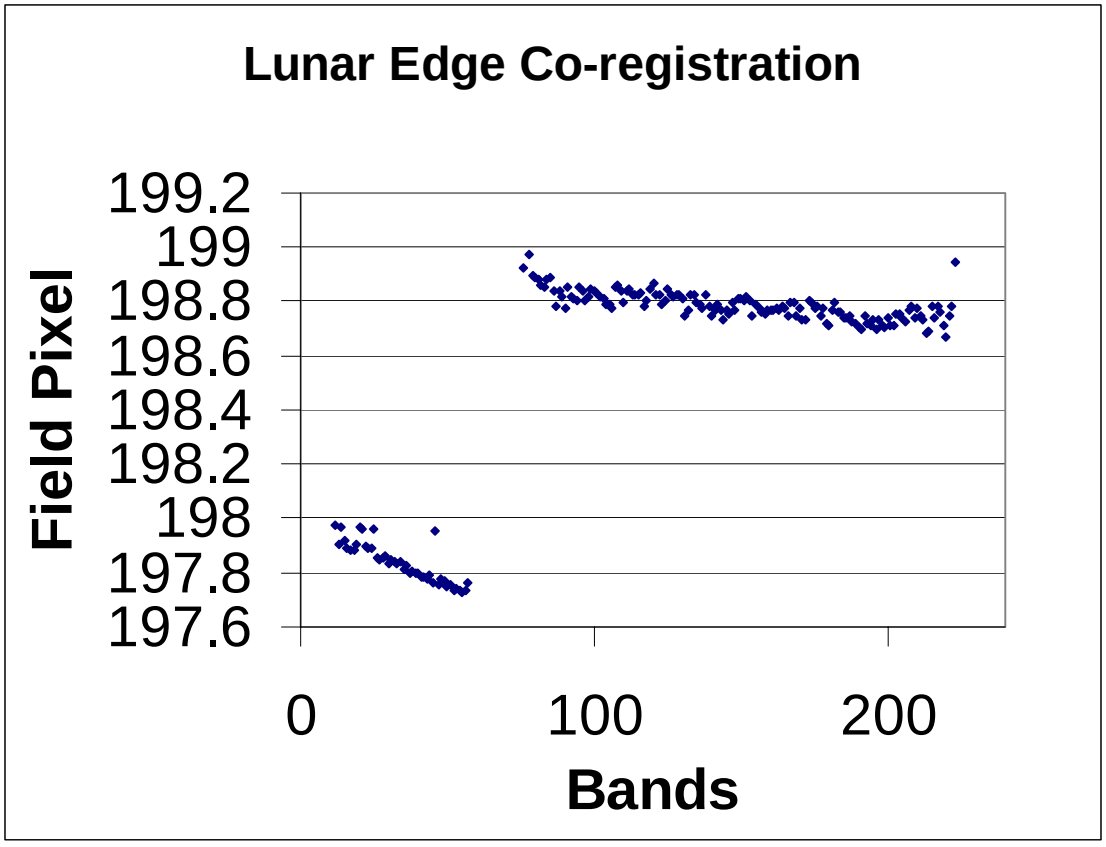

Figure 7.3.4.1-1 Lunar Edge Co-registration

7.3.4.2 Spatial Co-registration within VNIR or SWIR

Table 7.3.4.2-1 is a comparison of the co-registration within the VNIR or SWIR spectrometer.

Table 7.3.4.2-1 Spatial Co-registration within VNIR or SWIR spectrometer

Scene	Field Pixel	VNIR	SWIR
Post Vibe	20 locations	0.1 – 0.25	0.18 – 0.28
Ross Ice Shelf, day 16	77	0.1	0.3
Ross Ice Shelf, day 16	135	0.3	0.25
Ross Ice Shelf, day 16	215	0.1	0.3
Santa Barbara Cloud, day 3	106	0.2	0.4
Honolulu Cloud, day 363	44	0.25	0.3
Moon, day 38	19	0.15	0.2
Moon, day 38	199	0.2	0.2
Moomba, Day 58	30		0.3
Moomba, Day 58	144		0.4
Erta Ale, Day 37	178		0.4

The reported values for the spatial co-registration within the VNIR or SWIR spectrometers are consistent with the pre-flight measurements. The Ross Ice Shelf produced good results in the VNIR but there is significant scatter in the SWIR region. This is most likely due to the edge behavior in the SWIR that was discussed previously. The cloud scenes once again produced good results in the VNIR but had a large scatter in the SWIR possibly due to image non-uniformity. To resolve this deficiency SWIR images of Moomba and Erta Ale volcano echo were analyzed, but these images had signal that was quite low resulting in a co-registration measurement with significant noise. However, even with the high amount of noise the resulting value for the co-registration is reasonable.

7.3.5 Conclusion

The measurements for the spatial co-registration between the VNIR and SWIR and within the spectrometers agreed with the pre-flight measurements. Most of the measurements in the SWIR had a considerable amount of scatter. The exception was the moon but this scene only had a few spatial locations that were useable due to the edge problems described in section 7.2.4.4. The spatial co-registration within the VNIR or SWIR agreed with the pre-flight measurements but there was significant scatter so the measured shape during the pre-flight measurements could not be repeated. To achieve a higher degree of resolution, a scene should be chosen that has sufficient signal and has several locations in the swath width. The active illumination experiment could provide this scene.

8 PERFORMANCE VERIFICATION SUMMARY

This document discussed in detail the on-orbit performance of the Hyperion instrument. The instrument has performed consistently and solidly throughout the performance verification process. The pre-flight characterization remains valid for on-orbit operation. The instrument agreement with specification is the same as the pre-flight agreement. The instrument was characterized from the most fundamental level all the way to the end-to-end measurement.

The overall task was categorized into Radiometric Calibration, Spectral Characterization, and Image Quality with the most fundamental aspects being addressed to support the radiometric end-to-end measurement.

Radiometric Characterization:

An updated calibration file was released on March 30, 2001 as scheduled. The updated file is traceable to the extensive pre-flight radiometric calibration program. A solar calibration event was used to reduce pixel-to-pixel variation. A suite of internal lamp collects and solar calibration collects were used to assess the instrument's DCE-to-DCE and pixel-to-pixel repeatability. Data sets were analyzed to assess and characterize the instrument drift. Recommendations to improve level 1 processing were submitted and accepted. Known artifacts were reviewed to verify pre-flight correction algorithms remained applicable. Detailed studies of the instrument data revealed subtleties that were subsequently analyzed and assessed for their impact. Two areas that require supplemental analysis include verification of spectral smear and SWIR echo for the four pixels near the edge of the field of view. Pending further analysis, a residual error of 0.5% and 0.8% was budgeted for each respectively.

Radiometric assessment will be continuing over the life of the mission and will involve the collection of solar calibration events, trending of the internal calibration lamp, and collection of vicarious calibration sites. Coordination with other platforms is planned to strengthen this effort.

Spectral Characterization:

The atmospheric limb scan data was used as the basis for the spectral verification. The spectral features in the Hyperion spectrum were correlated with spectral features in the atmosphere, reflectance off the on-board diffuse panel, and the solar profile. Nineteen reference features were identified and used in the SWIR to verify the SWIR pre-flight spectral calibration. Two reference features were selected for the VNIR spectral calibration, the oxygen line at 762 nm and one solar line at 520 nm. The VNIR pre-flight calibration was adjusted using a wavelength offset and a rotation to provide a best match to the on-orbit measurements of the two reference lines. The results suggest a slight rotation in the spectral calibration may have occurred. However, the maximum difference between the pre-flight and on-orbit calibration are within the measurement error of the technique. As a result, the VNIR spectral calibration will not be updated. The final spectral calibration file name is SpectralL0_revA.dat. The revision was based on a review solely of the pre-flight calibration and pre-flight data.

Image Quality:

The ground sample distance was measured for the VNIR and SWIR using multiple scenes. The results were consistent with pre-flight characterization and specification. MTF measurements have been completed using both edge-type scenes and bridge scenes. The on-orbit MTF measurements have demonstrated that the MTF requirements are satisfied. For the in-track MTF measurements, there is not a significant change from the pre-flight measurements. For the cross-track MTF measurements, there is no shift that has been measured in the VNIR but there might be a shift in the SWIR. The additional collect of Port Eglin with the SWIR at operational temperature would be valuable to clarify this issue, as would feedback from the EO-1 Science Validation Team. Analysis of the spatial co-registration of spectral channels has been completed and the results are, again, consistent with pre-flight measurements within the error of the measurements. Although not a requirement, the VNIR-to-SWIR co-registration has been reviewed. There remains a one-pixel shift in the cross-track direction. There is a linear VNIR-to-SWIR in-track difference as a function of field-of-view location.

9 RECOMMENDATIONS FOR REMAINING MISSION

This section will provide suggestions on monitoring points to ensure high-quality Hyperion data for the extent of the mission.

The discussion parallels the organization of the performance verification task.

Radiometric Characterization:
To maintain radiometric accuracy the following plan is suggested.

1. Perform Solar Calibration Events on a weekly or alternate week basis. Data should be reviewed in terms of SNR and pixel-to-pixel variation.
2. Perform Lunar Calibration Events as recommended: Lunar calibrations, performed monthly, will further support the absolute accuracy and long-term stability as well as image quality aspects of the instrument.
3. Trend Internal Calibration Source: Process approximately 1 DCE a day for the purposes of maintaining the trending database.
4. Support Vicarious Calibration Efforts: On an as-available basis, data sets, which are complemented by extensive ground truth and collects by multiple-platforms should be reviewed. In the absence of scheduled ground truth collects, a monthly collect of Lake Frome and a monthly collect of one of the following is recommended - Niger 1, Arabia 1, or Libya 1.
5. On-orbit Calibration Updates: The combination of activities mentioned above should be reviewed on a monthly basis to determine if a calibration file update is required.

Spectral Characterization:
To maintain spectral calibration integrity the following plan is suggested.

1. Perform an atmospheric limb scan on a alternate month basis: The atmospheric limb scan enables a quick check of the spectral calibration of the VNIR and SWIR.
2. Support Characterization of Spectrally Significant Sites: Sites with known spectral features, e.g., Mt. Fitton and Cuprite, should be collected on an alternate month basis to enable a user-oriented verification/monitor of the spectral calibration.
3. Support Atmospheric Removal Efforts of the Hyperion Data: Out-of-bound reflectance measurements based on atmospherically removed Hyperion spectra can provide a cross-check of the spectral calibration.

Image Quality:
To maintain image quality characterization the following is suggested.

1. Review agricultural/metropolitan scenes: Monthly collect of, e.g., Coleambally or Cordoba Soy during the Northern winter or Maricopa, Blythe or California Supersite during the Northern summer. Monthly collect of any of the following: El Segundo, New York City, Washington, D.C. Visual inspection will enable identification of gross changes.
2. Perform a collect on an every third month basis of one of the following: Cross–Track Bridge (Port Eglin), In-Track Bridge (Cape Canaveral), and Lunar Calibration.
3. Support Vicarious Calibration Efforts with Georectification Capabilities, e.g. Lake Frome, Arizario, Barreal Blanco, Railroad Valley, White Sands, and others as available Review

VNIR-to-SWIR co registration to verify VNIR-to-SWIR In-Track field-of-view variation does not change.

Summary

Below is a summary of the types of scenes requested and the frequency of the collects that are recommended in order to maintain a high-quality Hyperion data product. For the daily DCE that is requested, the specific site that is collected is not critical since the data set will be used for trending purposes. The Hyperion specific collects consist of the lunar, and solar calibration collects as well as the atmospheric limb. Recommended sites used for agricultural, metropolitan, spectrally significant and uniform scene of known radiance categories are mentioned above.

Requests:
1. DCE (any site): Daily
2. Solar Calibration: weekly to bi-weekly
3. Lunar Calibration: monthly
4. Uniform Scene of Known Radiance: monthly
5. Agricultural site: monthly
6. Atmospheric Limb: bi-monthly
7. Spectrally significant site: bi-monthly
8. Metropolitan site: tri-monthly
9. Saharan Scene: monthly